



# DEVELOPMENT OF A PATIENT-SPECIFIC CAROTID ARTERY FLUID-STRUCTURE- INTERACTION MODEL

**Yanjing Liu**

Msc. Mechanical  
Engineering  
December, 2023

# Development of a Patient-Specific Carotid Artery Fluid-Structure- Interaction Model

by

Yanjing Liu

MSc. Mechanical Engineering

Faculty of Mechanical Mechanical,  
Maritime Maritime and Material Engineering

Supervisor: Dr.ir. A.C.Akyildiz

Daily Supervisor: ir. A.Tziotziou

# Summary

**Background:** Ischemic stroke is a major cause of death worldwide. Atherosclerosis in the carotid arteries is an established predictor of these events. FSI shows its advantage in simulating the hemodynamic environments due to involving the multiphysics coupling of fluid dynamics and structural mechanics regulations. Therefore, the aim of this thesis was to establish and demonstrate a framework, starting with the segment data extracted from CTA images and leading to patient-specific FSI modeling. Thus the results can be used to gain insights into the relationship between plaque changes over time and biomechanical stresses induced by blood flow using FSI.

**Method:** 3D coordinates are firstly extracted from CTA scans of patients with calcified atherosclerotic plaques in their carotid arteries, sourced from the PARISK study. This data was then used to reconstruct 3D surfaces and volumes of the carotid bifurcation structure. Subsequently, the Backward Incremental method is employed to compute the initial stresses and establish the zero-pressure geometry of the vessel. Following this, FSI simulations were conducted on six carotid bifurcations to obtain preliminary results, providing an initial test of the pipeline's robustness. Morphological changes, including plaque burden, wall thickness, and calcium distance, are quantified to study plaque progression over time. The numerical simulation results provide insights into biomechanical stresses, including fluid and solid wall shear stress and von Mises stress. The simulation results are subjected to post-processing for further analysis. The results are mapped to a 2D configuration, with 1.5mm along the centerline and 45° per sector to study the local behavior.

**Result:** The efficacy of the reconstruction and initial stress detection methods shows the robustness of the pipeline. The entire process is executed on six vessels, with a comprehensive examination of one case presented initially. This detailed analysis reveals metrics related to morphological changes, biomechanical stresses, and flow patterns. Subsequently, correlation and stress distribution analyses are conducted for all six vessels. Notably, negative correlations are discerned between stress and morphological changes, adding depth to the understanding of the relationship between biomechanics and morphological changes in these cases.

**Keywords:** *Atherosclerosis, Carotid Arteries, Fluid-Structure-Interaction, Plaque progression, Shear Stress, Structural Stress*

# Acknowledgements

Three years ago at this time, I decided to leave my hometown and come to the Netherlands for the next chapter of my life, a place that required a 12-hour flight to reach, and with such a different culture and weather. Now, as my master's program is about to conclude, looking back at these two years, I have received wonderful memories that I believe I will treasure no matter how many years pass.

First, I would like to thank my supervisors, Ali and Katerina, for their support throughout the project. Ali, I am truly appreciative of your invaluable scientific insights and continuous assistance. I always appreciate our discussion and the unexpected nuggets of wisdom you throw my way. I also want to thank Katerina for your support throughout this project. There have been moments when I felt struggled and lost, but your positive attitude and willingness to help have made me feel that I'm not alone in this journey. I've learned a great lot from both of you, and I wish you all the great things coming your way in the future.

I also want to thank everyone at the Biomechanics lab in the Biomedical Engineering group at the Cardiology Department of Erasmus Medical Center. This group has always welcomed and supported each member, creating a positive and collaborative environment. The moments we've shared during lunchtime, labouting, and working together have been enjoyable and memorable. Thank you all for contributing to a fantastic atmosphere.

My heartfelt thanks also go to my friends. The memories of our late-night chats, cooking nights, and incredible trips are truly cherished. Your presence makes my life more joyful and enriching. As we are about to part ways and start new adventures in different corners of the world, I hope that distance never becomes a barrier to our friendship.

Last but certainly not least, I want to express my special appreciation to my mom. Thank you for always supporting my decisions and having my back, even when you may not fully understand or agree with them. Your love strengthens me and brings courage to accept new challenges.

*Yanjing Liu  
December 2023*

# Contents

<b>Summary</b>	<b>i</b>
<b>Acknowledgements</b>	<b>ii</b>
<b>1 Introduction</b>	<b>1</b>
1.1 Atherosclerosis	1
1.2 Computed Tomography Angiography of Artery	2
1.3 Biomechanical Stress	3
1.4 Fluid-Structure Interaction Analysis	4
1.5 Thesis Objective and Outline	5
<b>2 Method</b>	<b>7</b>
2.1 Patient Data Acquisition	7
2.2 Vessel Model Reconstruction	7
2.3 Backward Incremental Method	11
2.3.1 Implementation of Backward Incremental Method in FEBio	12
2.3.2 BI Method Model Creation	13
2.4 Fluid-Structure Interaction Model Creation	15
2.4.1 Mesh Preparation	15
2.4.2 Material Model	16
2.4.3 Loading Conditions	16
2.4.4 Simulation Setting	17
2.5 Sector Creation	17
2.5.1 Morphological Metrics	18
2.5.2 Biomechanical Metrics	19
<b>3 Results</b>	<b>21</b>
3.1 Model Reconstruction	21
3.2 Validation of Backward Incremental Method	22
3.3 FSI Results: Patient 1L	24
3.4 FSI Result: Six Cases	32
<b>4 Discussion</b>	<b>37</b>
4.1 Framework	37
4.2 Result	38
4.3 Limitations	39
<b>5 Conclusion</b>	<b>41</b>
<b>6 References</b>	<b>42</b>
<b>A Reconstruction</b>	<b>50</b>

---

<b>B</b>	<b>Validation of Backward Incremental Method</b>	<b>55</b>
B.1	Ring Model . . . . .	55
B.2	Artery Model . . . . .	61
B.3	Ogen Material Model . . . . .	62
<b>C</b>	<b>Mesh Convergence Study</b>	<b>63</b>
C.1	Solid Domain . . . . .	64
C.2	Fluid Domain . . . . .	64
<b>D</b>	<b>FSI</b>	<b>66</b>
D.1	Fluid-Structure Interaction Module in FEBio . . . . .	66
D.2	Comparison of 2nd cycle and 4th cycle . . . . .	67
<b>E</b>	<b>Results</b>	<b>69</b>
E.1	Case 1R . . . . .	69
E.2	Case 2L . . . . .	75
E.3	Case 2R . . . . .	81
E.4	Case 3L . . . . .	87
E.5	Case 3R . . . . .	93

# List of Figures

1.1	Schematic representation of a healthy artery (left) and an atherosclerotic artery(right) [1]. . . . .	1
1.2	a. CTA images indicating plaque ulceration. Orange arrowheads show contrast material reaching into a carotid plaque [13]. b. CTA images indicating a large bulk of calcification (orange arrowheads) at the level of the bifurcation [13]. . . . .	2
1.3	a. Forces and stresses acting on the vascular wall [19]. b. Stresses generated in the vascular wall, including circumferential stress ( $\sigma_C$ ), longitudinal stress ( $\sigma_L$ ), and shear stress ( $\tau_w$ ) [19]. c. Laminar (left), transitional (middle), and turbulent (right) blood flow [23]. d. Distribution of wall shear stress in the carotid artery bifurcation [16]. . . . .	3
1.4	<b>Overview of the project.</b> . . . . .	6
2.1	<b>Summary of surface reconstruction process.</b> a. The original ECA and ICA contours. b. Interpolate contours between adjacent contours. c. Cap the inlet and outlet surfaces. The figure only shows capping the ICA outlet. d. Alphashape result. e. Zoom-in plot of bifurcation. f. Remesh the surface using Geogram. g. Add Extension at CCA inlet. h. The previous process would repeat to create the vessel surface. The vessel was created by subtracting the vessel surface from the lumen surface. . . . .	10
2.2	<b>Summary of geometry reconstruction process 2.</b> Artery Cutting: a. Artery and the red cutting cylinder. b. The original geometry(Grey) and geometry after cutting (Green). Extension: c. Inlet and outlet surface identification. d. The inner and outer rims of the inlet surface were lofted to create the extension. e. Geometry with inlet extension. Feature Detection: f. Calcium and artery. g. Solid-fluid interface. . . . .	11
2.3	<b>Backward incremental analysis model.</b> a. The artery wall with inlet and outlet extensions (Extension: yellow). b. The deformations of the CCA, ECA, and ICA were constrained in all three axes. c. Pressure was applied to the lumen surface. . . . .	13
2.4	<b>Top view of the ICA outlet during the boundary layer creation process.</b> . . . . .	15
2.5	<b>Inlet flow profile of average flow</b> from Lee’s study [60] and the scaled curve. . . . .	17
2.6	<b>3D to 2D map process.</b> a. Three branches were identified. b. Circumferential coordinate of mesh points around the centerlines ( $+\pi, -\pi$ ). c. Distance along the centerlines (mm). d-e. Example of wall thickness result mapped to each sector. The artery was divided into thin cross-sectional slices of 0.5mm and grouped into eight sectors ( $45^\circ$ ). The 2D map shows the vessel circumference on the x-axis and the distance along the centerline on the y-axis. . . . .	18

2.7	<b>Post-processing of morphological metrics.</b> a. Ray-tracing method. If the interaction was found from a node along its normal direction towards the calcium structure, calcium presence was identified and the distance was computed. b. A cross-section was generated perpendicular to the centerline for the calculation of plaque burden. Plaque burden was computed utilizing the lumen area and vessel area. . . . .	19
3.1	a. Distribution of percentage difference of volume change before and after smoothing and remeshing process. b. Distribution of maximum wall thickness.	21
3.2	<b>Verification using artery model with <math>opt\_iter = 16, 24</math>.</b> Backward incremental analysis with $p_i = 13.3$ kPa. The $p_f$ was set as 18 kPa. . . . .	23
3.3	a. Baseline carotid artery of patient 1L. b. Follow-up carotid artery of patient 1L. Blue: calcium. c. Diseased wall thickness region ( $>1.5$ mm, green) of baseline ICA-CCA. d. Diseased wall thickness region ( $>1.5$ mm, green) of follow-up ICA-CCA. e. The wall thickness of baseline ICA-CCA (mm). f. The wall thickness of follow-up ICA-CCA (mm). g. Change of wall thickness in ICA-CCA (mm). (WT: wall thickness; $\Delta$ WT: baseline wall thickness follow-up wall thickness) . . . . .	25
3.4	a. Plaque burden of baseline ICA-CCA. b. Plaque burden of follow-up ICA-CCA. c. Change of plaque burden in ICA-CCA. (PB: plaque burden; $\Delta$ PB: baseline plaque burden-follow-up plaque burden) . . . . .	26
3.5	a. Distance between calcium and lumen of baseline ICA-CCA. b. Distance between calcium and lumen of follow-up ICA-CCA (mm). c. Change of calcium distance of ICA-CCA (mm). (Orange: $\Delta$ calcium distance $>0$ ; Yellow: $\Delta$ calcium distance $<0$ ) . . . . .	26
3.6	<b>Fluid time-average wall shear stress (TAWSS) of case 1L at lumen surface.</b> a. Front view and back view of Fluid TAWSS. b. Low Fluid TAWSS plot. Stress larger than 1Pa was eliminated. c. 2D map plot of ICA-CCA FTAWSS.	27
3.7	<b>Solid time-average wall shear stress (TAWSS) of case 1L at lumen surface.</b> a. Front view and back view of Solid TAWSS at lumen surface. b. 2D map plot of ICA-CCA Solid TAWSS at lumen surface. . . . .	27
3.8	<b>Time-average vom Mises stress (TAVMS) of case 1L at lumen surface.</b> a. Front view and back view of TAVMS at lumen surface. b. 2D map plot of ICA-CCA TAVMS at lumen surface. . . . .	28
3.9	<b>Radial average solid time-average von Mises stress (TAWMS) of case 1L.</b> a. Front view and back view of radial average TAWMS. b. 2D map plot of ICA-CCA radial average TAWMS. c. Cutview plot of time-average von Mises stress at planes A and B (Pa). . . . .	29
3.10	<b>Streamline plot and velocity profiles at different positions in the carotid bifurcation model (m/s).</b> . . . . .	30
3.11	<b>Velocity pattern at different time points of a cardiac cycle (m/s).</b> . . . . .	31
3.12	<b>Vessel models with calcium (Blue) and lipid (Green).</b> From patient 1 a. LEFT, b. RIGHT; patient 2 c. LEFT, d. RIGHT; patient 3 e. LEFT, f. RIGHT.	32
3.13	<b>Overview of morphological metrics of six cases at baseline and follow-up.</b>	33
3.14	Overview of six vessels showing the stress distribution for each vessel. . . . .	35

3.15	<b>Stress Distribution and morphological changes over time.</b> a-c. Fluid time-average wall shear stress (TAWSS) d-f. Solid time-average wall shear stress (TAWSS) g-i. Average time-average von Mises stress (TAVMS) j-l. Time-average von Mises stress (TAVMS) at interface . . . . .	36
A.1	<b>Contour and alpha shape result with different alpha values.</b> Light Blue: CCA-ECA Vessel; Dark Blue: CCA-ICA Vessel. . . . .	50
A.2	<b>Reconstruction result of patient 1-20 before adding the extension.</b> Blue: calcium; green: lipid. . . . .	51
A.3	<b>Reconstruction result of patient 21-40 before adding the extension.</b> Blue: calcium; green: lipid. . . . .	52
A.4	<b>Reconstruction result of patient 41-60 before adding the extension.</b> Blue: calcium; green: lipid. . . . .	53
A.5	<b>Reconstruction result of patient 61-80 before adding the extension.</b> Blue: calcium; green: lipid. . . . .	54
B.1	<b>Verification using the ring model.</b> A pressure of 50 kPa was first applied on the inner surface at zero-pressure geometry. The deformed geometry was taken as the starting geometry for backward incremental analysis with $p_i$ kPa. A final pressure was then applied using the input from backward incremental analysis. The reference stress distribution was calculated by applying the final pressure on undeformed geometry as the reference. The stresses from stage 2 were then compared with the reference. . . . .	56
B.2	Max difference of von Mises stress of different methods and iteration numbers. Stage 1: Left, Stage 2: Right. . . . .	57
B.3	The Von Mises stress result with Stage 1 (Left) and Stage 2 (Right) applying on undeformed geometry. . . . .	57
B.4	The Von Mises stress result obtained using Method 1 with 16 iterations was compared to the reference result to calculate the difference. Stage 1: Left, Stage 2: Right. . . . .	58
B.5	The Von Mises stress result obtained using Method 1 with 24 iterations was compared to the reference result to calculate the difference. Stage 1: Left, Stage 2: Right. . . . .	58
B.6	The Von Mises stress result obtained using Method 1 with 32 iterations was compared to the reference result to calculate the difference. Stage 1: Left, Stage 2: Right. . . . .	59
B.7	The Von Mises stress result obtained using Method 2 with 16 iterations was compared to the reference result to calculate the difference. Stage 1: Left, Stage 2: Right. . . . .	59
B.8	The Von Mises stress result obtained using Method 2 with 24 iterations was compared to the reference result to calculate the difference. Stage 1: Left, Stage 2: Right. . . . .	60
B.9	The Von Mises stress result obtained using Method 2 with 32 iterations was compared to the reference result to calculate the difference. Stage 1: Left, Stage 2: Right. . . . .	60
B.10	The Von Mises stress result of Stage 1 (a) and Stage 2 (b) from abaqus. . . . .	61

B.11	The Von Mises stress result obtained using Method 1. a. iteration = 16, Stage 1. c. iteration = 16, Stage 2. a. iteration = 24, Stage 1. a. iteration = 24, Stage 2.	61
B.12	The Von Mises stress result obtained using Method 2. a. iteration = 16, Stage 1. c. iteration = 16, Stage 2. a. iteration = 24, Stage 1. a. iteration = 24, Stage 2.	62
B.13	Stress–stretch data points obtained from [53], with corresponding fitted curves using Ogden strain energy density functions (N=1,2,3,4).	62
D.1	<b>Comparison of flow between the 2nd and 4th cycles.</b> a. Inlet velocity profile settings. b. Inlet and outlet flow results. c. Percentage difference in inlet and outlet flow between the 2nd and 4th cycles. d. Comparison of CCA inlet flow between the 2nd and 4th cycles. e. Comparison of ECA outlet flow between the 2nd and 4th cycles. f. Comparison of ICA outlet flow between the 2nd and 4th cycles.	67
D.2	<b>Comparison between the 2nd and 4th Cycles.</b> a. Selection of a bifurcation point marked in red to obtain shear stress results. b. Maximum fluid shear stress. c. Difference in shear stress between the 2nd and 4th cycles. e. Selection of a point on the plaque cap marked in red to obtain von Mises stress results. f. von Mises stress. g. Difference in von Mises stress between the 2nd and 4th cycles.	68
E.1	<b>2D map plot of WT for case 1R.</b> a. WT at baseline. b. DWT at baseline. c. WT at follow-up. d. DTW at follow-up. e. Difference of WT between baseline and follow-up. (WT: wall thickness; DWT: diseased wall thickness)	69
E.2	<b>2D map plot of calcium distance for case 1R.</b> a. Calcium distance at baseline. b. Calcium distance at follow-up. c. Difference of calcium distance between baseline and follow-up. Only the sectors with calcium detected were presented. a and b shared the same colormap.	70
E.3	<b>2D map plot of plaque burden for case 1R.</b> a. Plaque burden at baseline. b. Plaque burden at follow-up. c. Difference of plaque burden between baseline and follow-up. a and b shared the same colormap.	70
E.4	<b>Fluid wall shear stress (WSS) for case 1R.</b> a. Front view and back view of the stress distribution. b. 2D map of fluid time-average WSS. c. 2D map of min fluid WSS over a cycle. d. 2D map of max fluid WSS over a cycle.	71
E.5	<b>Solid wall shear stress (WSS) for case 1R.</b> a. Front view and back view of the stress distribution. b. 2D map of solid time-average WSS. c. 2D map of min solid WSS over a cycle. d. 2D map of max solid WSS over a cycle.	72
E.6	<b>Average von Mises stress (VMS) for case 1R.</b> a. Front view and back view of the stress distribution. b. 2D map of average VMS. c. 2D map of min average VMS over a cycle. d. 2D map of max average VMS over a cycle.	73
E.7	<b>Interface von Mises stress (VMS) for case 1R.</b> a. Front view and back view of the stress distribution. b. 2D map of interface VMS. c. 2D map of min interface VMS over a cycle. d. 2D map of max interface VMS over a cycle.	74
E.8	<b>2D map plot of WT for case 2L.</b> a. WT at baseline. b. DWT at baseline. c. WT at follow-up. d. DTW at follow-up. e. Difference of WT between baseline and follow-up. (WT: wall thickness; DWT: diseased wall thickness)	75

E.9	<b>2D map plot of calcium distance for case 2L.</b> a. Calcium distance at baseline. b. Calcium distance at follow-up. c. Difference of calcium distance between baseline and follow-up. Only the sectors with calcium detected were presented. a and b shared the same colormap. . . . .	75
E.10	<b>2D map plot of plaque burden for case 2L.</b> a. Plaque burden at baseline. b. Plaque burden at follow-up. c. Difference of plaque burden between baseline and follow-up. a and b shared the same colormap. . . . .	76
E.11	<b>Fluid wall shear stress (WSS) for case 2L.</b> a. Front view and back view of the stress distribution. b. 2D map of fluid time-average WSS. c. 2D map of min fluid WSS over a cycle. d. 2D map of max fluid WSS over a cycle. . . . .	77
E.12	<b>Solid wall shear stress (WSS) for case 2L.</b> a. Front view and back view of the stress distribution. b. 2D map of solid time-average WSS. c. 2D map of min solid WSS over a cycle. d. 2D map of max solid WSS over a cycle. . . . .	78
E.13	<b>Average von Mises stress (VMS) for case 2L.</b> a. Front view and back view of the stress distribution. b. 2D map of average VMS. c. 2D map of min average VMS over a cycle. d. 2D map of max average VMS over a cycle. . . . .	79
E.14	<b>Interface von Mises stress (VMS) for case 2L.</b> a. Front view and back view of the stress distribution. b. 2D map of interface VMS. c. 2D map of min interface VMS over a cycle. d. 2D map of max interface VMS over a cycle. . . . .	80
E.15	<b>2D map plot of WT for case 2R.</b> a. WT at baseline. b. DWT at baseline. c. WT at follow-up. d. DTW at follow-up. e. Difference of WT between baseline and follow-up. (WT: wall thickness; DWT: diseased wall thickness)	81
E.16	<b>2D map plot of calcium distance for case 2R.</b> a. Calcium distance at baseline. b. Calcium distance at follow-up. c. Difference of calcium distance between baseline and follow-up. Only the sectors with calcium detected were presented. a and b shared the same colormap. . . . .	81
E.17	<b>2D map plot of plaque burden for case 2R.</b> a. Plaque burden at baseline. b. Plaque burden at follow-up. c. Difference of plaque burden between baseline and follow-up. a and b shared the same colormap. . . . .	82
E.18	<b>Fluid wall shear stress (WSS) for case 2R.</b> a. Front view and back view of the stress distribution. b. 2D map of fluid time-average WSS. c. 2D map of min fluid WSS over a cycle. d. 2D map of max fluid WSS over a cycle. . . . .	83
E.19	<b>Solid wall shear stress (WSS) for case 2R.</b> a. Front view and back view of the stress distribution. b. 2D map of solid time-average WSS. c. 2D map of min solid WSS over a cycle. d. 2D map of max solid WSS over a cycle. . . . .	84
E.20	<b>Average von Mises stress (VMS) for case 2R.</b> a. Front view and back view of the stress distribution. b. 2D map of average VMS. c. 2D map of min average VMS over a cycle. d. 2D map of max average VMS over a cycle. . . . .	85
E.21	<b>Interface von Mises stress (VMS) for case 2R.</b> a. Front view and back view of the stress distribution. b. 2D map of interface VMS. c. 2D map of min interface VMS over a cycle. d. 2D map of max interface VMS over a cycle. . . . .	86
E.22	<b>2D map plot of WT for case 3L.</b> a. WT at baseline. b. DWT at baseline. c. WT at follow-up. d. DTW at follow-up. e. Difference of WT between baseline and follow-up. (WT: wall thickness; DWT: diseased wall thickness)	87

E.23	<b>2D map plot of calcium distance for case 3L.</b> a. Calcium distance at baseline. b. Calcium distance at follow-up. c. Difference of calcium distance between baseline and follow-up. Only the sectors with calcium detected were presented. a and b shared the same colormap. . . . .	87
E.24	<b>2D map plot of plaque burden for case 3L.</b> a. Plaque burden at baseline. b. Plaque burden at follow-up. c. Difference of plaque burden between baseline and follow-up. a and b shared the same colormap. . . . .	88
E.25	<b>Fluid wall shear stress (WSS) for case 3L.</b> a. Front view and back view of the stress distribution. b. 2D map of fluid time-average WSS. c. 2D map of min fluid WSS over a cycle. d. 2D map of max fluid WSS over a cycle. . . . .	89
E.26	<b>Solid wall shear stress (WSS) for case 3L.</b> a. Front view and back view of the stress distribution. b. 2D map of solid time-average WSS. c. 2D map of min solid WSS over a cycle. d. 2D map of max solid WSS over a cycle. . . . .	90
E.27	<b>Average von Mises stress (VMS) for case 3L.</b> a. Front view and back view of the stress distribution. b. 2D map of average VMS. c. 2D map of min average VMS over a cycle. d. 2D map of max average VMS over a cycle. . . . .	91
E.28	<b>Interface von Mises stress (VMS) for case 3L.</b> a. Front view and back view of the stress distribution. b. 2D map of interface VMS. c. 2D map of min interface VMS over a cycle. d. 2D map of max interface VMS over a cycle. . . . .	92
E.29	<b>2D map plot of WT for case 3R.</b> a. WT at baseline. b. DWT at baseline. c. WT at follow-up. d. DTW at follow-up. e. Difference of WT between baseline and follow-up. (WT: wall thickness; DWT: diseased wall thickness)	93
E.30	<b>2D map plot of calcium distance for case 3R.</b> a. Calcium distance at baseline. b. Calcium distance at follow-up. c. Difference of calcium distance between baseline and follow-up. Only the sectors with calcium detected were presented. a and b shared the same colormap. . . . .	93
E.31	<b>2D map plot of plaque burden for case 3R.</b> a. Plaque burden at baseline. b. Plaque burden at follow-up. c. Difference of plaque burden between baseline and follow-up. a and b shared the same colormap. . . . .	94
E.32	<b>Fluid wall shear stress (WSS) for case 3R.</b> a. Front view and back view of the stress distribution. b. 2D map of fluid time-average WSS. c. 2D map of min fluid WSS over a cycle. d. 2D map of max fluid WSS over a cycle. . . . .	95
E.33	<b>Solid wall shear stress (WSS) for case 3R.</b> a. Front view and back view of the stress distribution. b. 2D map of solid time-average WSS. c. 2D map of min solid WSS over a cycle. d. 2D map of max solid WSS over a cycle. . . . .	96
E.34	<b>Average von Mises stress (VMS) for case 3R.</b> a. Front view and back view of the stress distribution. b. 2D map of average VMS. c. 2D map of min average VMS over a cycle. d. 2D map of max average VMS over a cycle. . . . .	97
E.35	<b>Interface von Mises stress (VMS) for case 3R.</b> a. Front view and back view of the stress distribution. b. 2D map of interface VMS. c. 2D map of min interface VMS over a cycle. d. 2D map of max interface VMS over a cycle. . . . .	98

# List of Tables

2.1	Material parameters of solid components. . . . .	15
2.2	Material parameters of fluid [59] . . . . .	16
2.3	Biomechanical Metrics . . . . .	20
3.1	Results for the percentage difference of volume change [%] . . . . .	22
3.2	Results for maximum wall thickness of the artery [mm] . . . . .	22
3.3	Maximum Von Mises Stress Results of Artery Model for Different Methods and Iteration Numbers [kPa] . . . . .	24
3.4	Overview of Morphological Changes. . . . .	33
3.5	Overview of Time-Averaged Biomechanical Metrics of Sectors (N = 2808). . . . .	34
3.6	Threshold for Stress Distribution . . . . .	34
B.1	Maximum Von Mises Stress Results of Ring Model for Different Methods and Iteration Numbers [kPa] . . . . .	56
C.1	Mesh Convergence Result of Solid Domain . . . . .	64
C.2	Element Settings and Maximum Edge Sizes Analysis for Fluid Domain . . . . .	64
C.3	Mesh Convergence Result of the Fluid Domain with Different Element Numbers. . . . .	65
C.4	Mesh Convergence Result of the Fluid Domain with Different Segment Numbers of the Boundary Layer. . . . .	65

## Introduction

### 1.1. Atherosclerosis

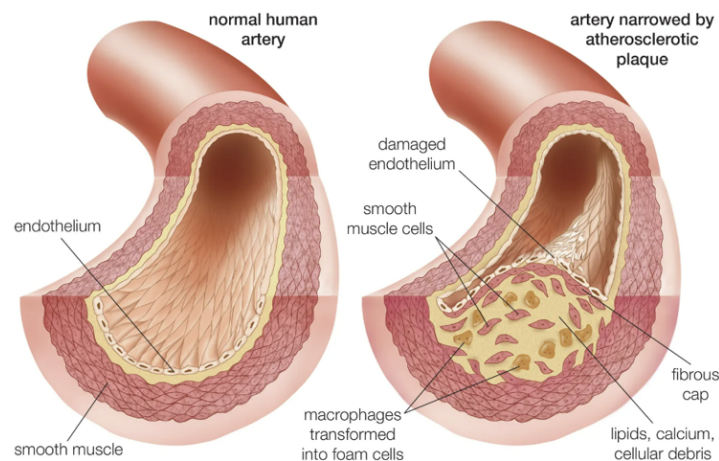


**Figure 1.1:** Schematic representation of a healthy artery (left) and an atherosclerotic artery(right) [1].

Ischaemic stroke was one of the leading causes of premature mortality globally [2]. Cardiovascular disease deaths increased by 12.5% from 2005 to 2015, highlighting the urgent need to better understand the underlying mechanisms driving this global health crisis. Atherosclerosis was a major contributor to adverse acute cardiovascular events, characterized by a local thickening of the walls of arteries due to the formation of lesions within the wall [3]. Endothelial cells became more permeable for lipoproteins, leading to low-density lipoproteins accumulation and the initiation of the disease [4][5]. Subsequent inflammatory responses, combined with smooth muscle cell migration, proliferation, extracellular matrix deposition, and intraplaque hemorrhage, contributed to intimal thickening and the potential for rupture (Figure 1.1). Arterial plaque developed in the carotid artery contributed to carotid stenosis and reduced blood supply to the brain [6]. The impact led to repetitive transient ischemic attacks due to the decreased brain oxygen supply especially when combined with proximal stenosis. Additionally, the heightened risk of thrombosis complicated the situation, with clots forming within narrowed carotid arteries, potentially traveling to the brain and causing ischemic strokes

[7]. The presence of thrombosis may also contribute to stenosis, increasing the likelihood of adverse cerebrovascular events [8].

## 1.2. Computed Tomography Angiography of Artery

Vessel wall imaging has been increasingly used to characterize plaque for the assessment of atherosclerotic carotid arteries [9]. While various imaging methods can provide detailed plaque information, Computed Tomography Angiography (CTA) was particularly appealing for carotid plaque imaging [10] due to its relatively low cost, widespread availability, operator independence, and capacity to discern high-risk features [11].

CTA scans were conducted following the intravenous administration of nonionic iodinated contrast through a peripheral IV, utilizing a power injector with a 4-mL/s flow rate. Helical mode CT scanning was performed with a multidetector scanner spanning from the aortic arch to the C1 ring, achieving submillimeter resolution [12]. The resulting grey-scale images with tissue density-dependent coloring provided rich detail regarding plaque morphology and features [11]. Studies indicated that CTA classification was particularly effective in classifying calcifications, ulcerations, and measuring fibrous cap thickness (Figure 1.2ab). At the same time, its performance was relatively less robust for classifying lipid-rich necrotic cores and hemorrhage [10][12].

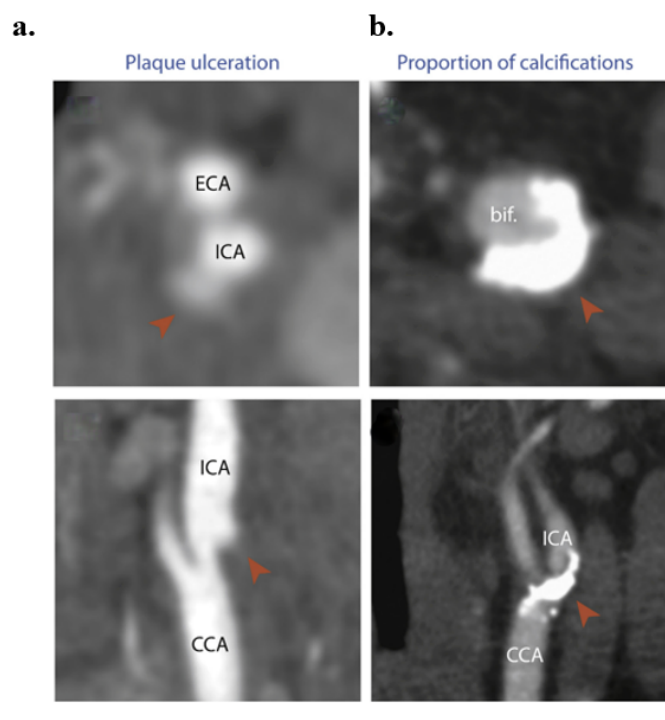


**Figure 1.2:** a. CTA images indicating plaque ulceration. Orange arrowheads show contrast material reaching into a carotid plaque [13]. b. CTA images indicating a large bulk of calcification (orange arrowheads) at the level of the bifurcation [13].

### 1.3. Biomechanical Stress

Among all factors that modulated the pathogenesis of atherosclerosis, hemodynamic factors were largely responsible for the regional localization of plaques and progression of atherosclerosis [14]. The arterial system was continually exposed to hemodynamic forces, including structural stress and shear stress, resulting from blood flow and blood pressure (Figure 1.3ab) [15]. The stress induced by blood pressure was three orders of magnitude greater than shear stress, and thus was considered a factor associated with both plaque rupture [6] and fatigue failure [16]. In larger vessels, long-term cyclic stress contributed to fatigue failure of artery [17]. The repetitive deformations induced by the cardiac cycle emerged as another critical factor influencing plaque stability [18].

On the other hand, shear stress referred to the tangential force generated by the friction between the flowing blood and the inner arterial surface. It was proportional to the product of blood viscosity ( $\mu$ ) and the spatial gradient of blood velocity at the vessel wall [19]. The pulsatile nature of the arterial blood flow and arterial geometric configuration determined the shear stress patterns. In relatively straight arterial segments, shear stress exhibited a pulsatile nature with a unidirectional magnitude, resulting in a positive time-averaged value (Figure 1.3d) [20]. However, disturbed flow patterns were typically observed at arterial bends and bifurcations. Due to lumen stenosis and flow pulsatility, the lateral motion of blood became completely randomized [21], leading to low or oscillatory shear stress. This phenomenon caused endothelial dysfunction and initiated the progression of atherosclerotic plaques [22].

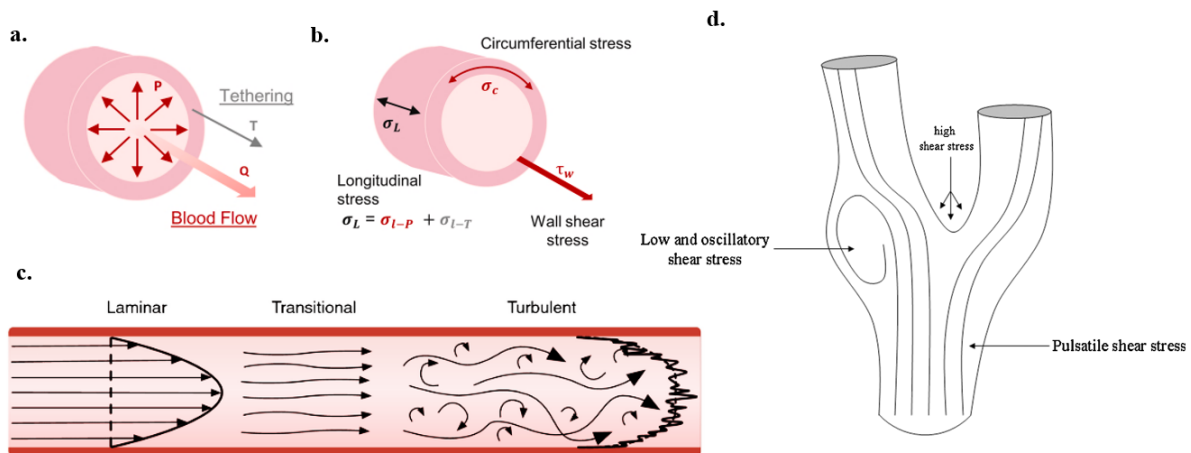


**Figure 1.3:** a. Forces and stresses acting on the vascular wall [19]. b. Stresses generated in the vascular wall, including circumferential stress ( $\sigma_C$ ), longitudinal stress ( $\sigma_L$ ), and shear stress ( $\tau_w$ ) [19]. c. Laminar (left), transitional (middle), and turbulent (right) blood flow [23]. d. Distribution of wall shear stress in the carotid artery bifurcation [16].

In the human vascular system, the carotid artery served as a critical component, enabling blood flow from the aorta to the brain. The presence of atherosclerotic plaque in this artery could disrupt blood flow to the brain, potentially leading to cerebrovascular diseases [8]. The common carotid artery (CCA) ascended from the aorta and then divided into two terminal branches: the internal carotid artery (ICA) and the external carotid artery (ECA) [24]. This bifurcation site was particularly susceptible to atherosclerotic plaque formation due to its specific arterial

geometry [25] due to the influenced local hemodynamic forces [26]. Among all factors that modulated the pathogenesis of atherosclerosis, hemodynamic factors were largely responsible for the regional localization of plaques and the progression of atherosclerosis [14].

In carotid circulation, there were specific regions where atherosclerosis tended to develop, particularly on the outer wall of the internal carotid artery [26]. The carotid artery bifurcation was inherently asymmetric, with the carotid artery sinus possessing a cross-sectional area twice as large as the distal segment of the internal carotid artery [16]. This structural feature promoted the separation of flow and led to complex helical and reverse flow patterns [27]. Disturbed flow patterns were typically observed on the outer wall of the sinus, resulting in the generation of low and oscillating levels of wall shear stress (Figure 1.3d). Conversely, the flow divider point of the bifurcation and the inner wall of the external carotid artery was characterized by high wall shear stress, providing a protective effect against the development of atherosclerosis [27].

## 1.4. Fluid-Structure Interaction Analysis

To simulate the hemodynamic environments within carotid arteries and understand changes in pathological conditions, two main methods were employed: Computational Fluid Dynamics (CFD) and Fluid-Structure Interaction (FSI). CFD primarily focused on analyzing blood flow dynamics, while FSI took into consideration the influence of the vessel wall on the analysis [28]. FSI was a common phenomenon in vascular systems, involving the multiphysics coupling of fluid dynamics and structural mechanics regulations. This interaction occurred between a deformable or moving structure and the surrounding or interior fluid flow [29]. Given that the fluid domain was dynamically influenced by the deformation of arterial walls during the cardiac cycle, it became crucial to incorporate this movement into the analysis [30]. However, taking into account the deformation and motion of vessels increased computational effort, primarily due to the vessel's mechanical properties and the coupling between the fluid and solid systems [31].

Researchers have explored the hemodynamics of arteriosclerotic diseases using FSI models, particularly in stenosed carotid arteries [32]. Comparative analyses between CFD and FSI results have been conducted [33][34]. Notably, FSI models exhibited higher wall shear stress and velocity, especially in plaque regions, when compared to CFD results [33]. Numerical studies have discussed various factors influencing FSI simulations, including the role of vessel geometry [35][30], flow conditions [30], and material models [36]. In contrast to idealized geometry models, simulations using patient-specific vessel geometry revealed that flow in the carotid sinus was dominated by strong helical patterns [35]. Therefore, imaging data were used to build patient-specific vessel geometry. For FSI, the acquisition of geometry involved the reconstruction of fluid geometry as well as the solid domain. One common way to utilize CTA image data was to obtain the lumen geometry and thicken the lumen surface to build the vessel [34]. However, this method induced bias since the thickness of the actual vessel was not uniform. Only a few researchers obtained the vessel structure as well as lumen structure using CTA data [30][37][38]. Additionally, under conditions of low outlet flow rate and high distal vascular resistance, lower wall shear stress was observed in the carotid artery FSI model [30]. Teng et al. [39] conducted fitting of the neo-Hookean, Mooney-Rivlin, Ogden, and Yoah material models with experimental data. They performed FSI using the fitted results and demonstrated that modified Mooney-Rivlin models might be more appropriate choices,

considering their ability to characterize material properties and achieve convergence in 3D FSI analyses. Tang et al. [40] finds that plaques with prior ruptures are associated with higher critical stress conditions using patient-specific plaque morphology in FSI model.

## 1.5. Thesis Objective and Outline

Limited studies obtained both vessel and lumen structures from CTA data, and few methodologies exist for application in FSI modeling with large databases [30][37][38]. Therefore, the aim of this thesis was to establish and demonstrate a comprehensive framework, starting with the segment data extracted from CTA images and leading to patient-specific FSI modeling. Thus the results can be used to gain insights into the relationship between plaque changes over time and biomechanical stresses induced by blood flow using FSI.

The framework was explained in detail in Chapter 2. The first step involved extracting 3D coordinates from CTA scans of patients with calcified atherosclerotic plaques in their carotid arteries, sourced from the PARISK study. This data was then used to reconstruct 3D surfaces and volumes of the carotid bifurcation structure, a process detailed in Section 2.2. Subsequently, the Backward Incremental method was employed to compute the initial stresses and establish the zero-pressure geometry of the vessel. This step was crucial for eliminating the effect of initial stress during image acquisition. Section 2.3 outlined two methods for BI implementation and compared their effectiveness. Following this, FSI simulations were conducted on six carotid bifurcations to obtain preliminary results, providing an initial test of the pipeline's robustness. The simulation results were subjected to post-processing for further analysis. Section 2.4 provided a detailed explanation of the methodology behind FSI model creation, followed by the post-processing process. In Chapter 3, the qualifications of reconstruction and initial stress detection method were first presented. Then the entire pipeline was conducted on six vessels. A detailed explanation of one case was first presented, followed by a stress distribution analysis of all six vessels.

The project's workflow is shown in the following figure:

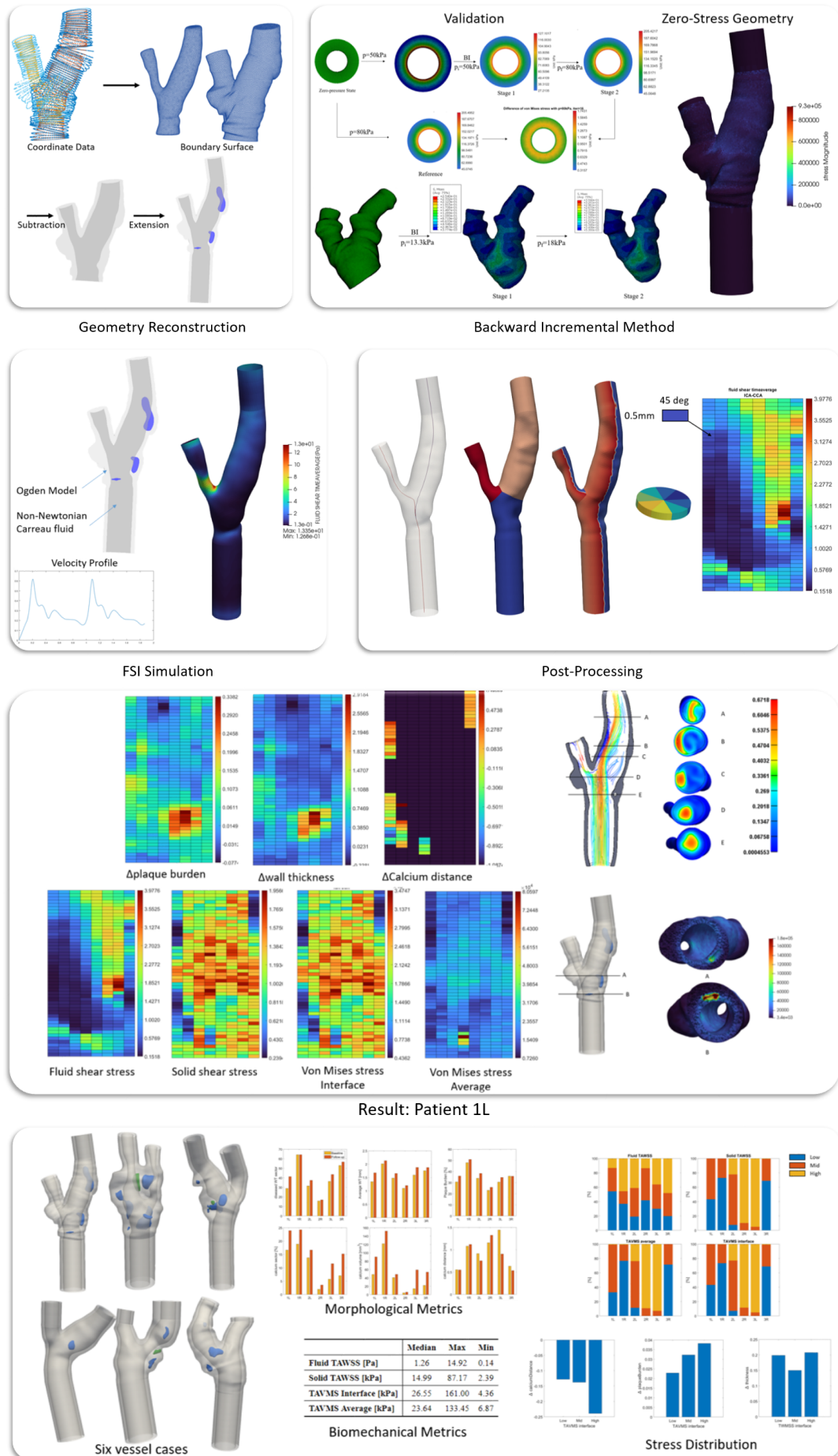


Figure 1.4: Overview of the project.

# 2

## Method

### 2.1. Patient Data Acquisition

The CTA image of the Plaque At RISK (PARISK) study was used in this study. The PARISK study was a prospective multicenter cohort study that investigated noninvasive imaging techniques for assessing carotid plaque characteristics in patients with symptomatic mild-to-moderate carotid artery stenosis [41]. The study collected image information on patients who had experienced a recent (<3 months) transient ischemic attack, and the imaging process was repeated two years after inclusion. Between September 2010 and December 2014, a total of 240 patients were enrolled in the PARISK study. Out of these, 161 patients had carotid artery CTA available for analysis [42]. The PARISK carotids were segmented using QAngio software [43] by a trained colleague (A.T.).

### 2.2. Vessel Model Reconstruction

The construction of the model began with the utilization of ICA and ECA contour coordinates. It was worth noting that the contours of ICA-CCA and ECA-CCA exhibited a degree of overlap beneath the bifurcation point, so they were not perfectly aligned. Consequently, reconstructing two separate vessel structures and merging these structures without further adjustment would lead to defects in the overlapped regions. To solve this problem, the alpha shape function was employed to conduct the reconstruction process. Alpha shapes were based on the Delaunay triangulation. For a given value of  $\alpha$ , the alpha shape result included all the simplices in the Delaunay triangulation with an empty circumscribing sphere with a radius equal or smaller than  $\alpha$  [44]. This method treated the two contour points as a point cloud and created a bounding surface. Boolean subtraction was then performed. A detailed visualization of this process was presented in Figure 2.1 and Figure 2.2. This entire process was automatically executed through custom MATLAB R2023a scripts developed in-house.

#### Bounding Surface Creation

The results of AlphaShape were governed by a controlling parameter  $\alpha$ , which was a real number greater than zero. When  $\alpha$  approached infinity, the result became equivalent to a convex hull [45]. Conversely, as  $\alpha$  decreased, the surface boundary became more tightly defined,

resulting concave geometries, particularly around bifurcations. Given the objective of reconstructing the CCA-ICA and CCA-ECA segments together while accurately capturing bifurcation geometry, the  $\alpha$  parameter was set to a low value (Figure A.1). Achieving this necessitated a higher point density within the desired regions. Linear interpolation was employed to introduce additional contours between two adjacent ones, reducing the spacing between adjacent contours to 0.1 mm (Figure 2.1b). Furthermore, points were added within the inlet and outlet surfaces at intervals of 0.1 mm (Figure 2.1c). This point cloud preparation was crucial for effective bifurcation identification, accomplished with  $\alpha = 0.2$ .

### Remesh

Although the resulting mesh displayed the bifurcation structure, a large number of nodes were generated due to the small alpha value. This resulted in a large file and the presence of small holes in the mesh. To address these issues, the external Geogram library [46] was employed to remesh the surface obtained from the alphashape operation. To repair potential surface imperfections such as small holes and self-intersections, the MeshFix module [47] was utilized. This step significantly improved the overall quality of the surface structure. The final structure underwent 10 iterations of Laplacian smoothing. The vessel volume of the alphashape result and after the smoothing process was computed as a coefficient to assess the quality of this procedure.

### Subtraction

This entire process was applied to both lumen and vessel surfaces. The vessel wall was generated by performing boolean subtraction between the lumen and vessel surfaces (Figure 2.1g)[48]. The resulting output encapsulated both the faces and vertices data of the enclosed surface and an STL file was also generated.

### Calcium and Lipid

Calcium and lipid data were extracted from the imaging. The structures were converted into face and vertex data, followed by a remeshing process using a point spacing of 0.3 mm. Subsequently, a smoothing operation was applied using the Laplacian method with ten iterations.

### Extension

To ensure the flow attained full development before entering the arterial region, an inlet extension was implemented with a length of 5 times of CCA radius. In addition, to avoid recirculation of the flow and divergence of simulation, outlet extension was added where ICA and ECA were shorter than 30mm or the end contour was close to calcium. This involved lofting the boundary rim along its normal vector, extending it by a length equivalent to five times the lumen radius. Before extensions were added, the inlet and outlets were cut approximately 0.3 mm (Figure 2.2a-b). The booleanOperation function [48] was used for the cutting process. This same procedure was repeated for both outlets. Then, the inner and outer rims were lofted in a similar manner, achieving the desired extension length and forming a cylindrical structure (Figure 2.2d).

### Feature Identification

In preparation for the finite element and fluid-structure interaction analysis, identifying geometry details (Figure 2.2g) for boundary and loading conditions was required. This was accomplished by locating the solid-fluid interface on the inner surface of the vessel wall, determined

through the recognition of dihedral angles below a specific threshold. The boundary curves for this interface were explicitly defined as the inlet and outlet curves. The model's final output included the following essential information:

- Mesh data of vessel surface, calcium, and lipid;
- Face data of solid-fluid interface;
- Node data of CCA inlet rim, ECA outlet rim, and ICA outlet rim.

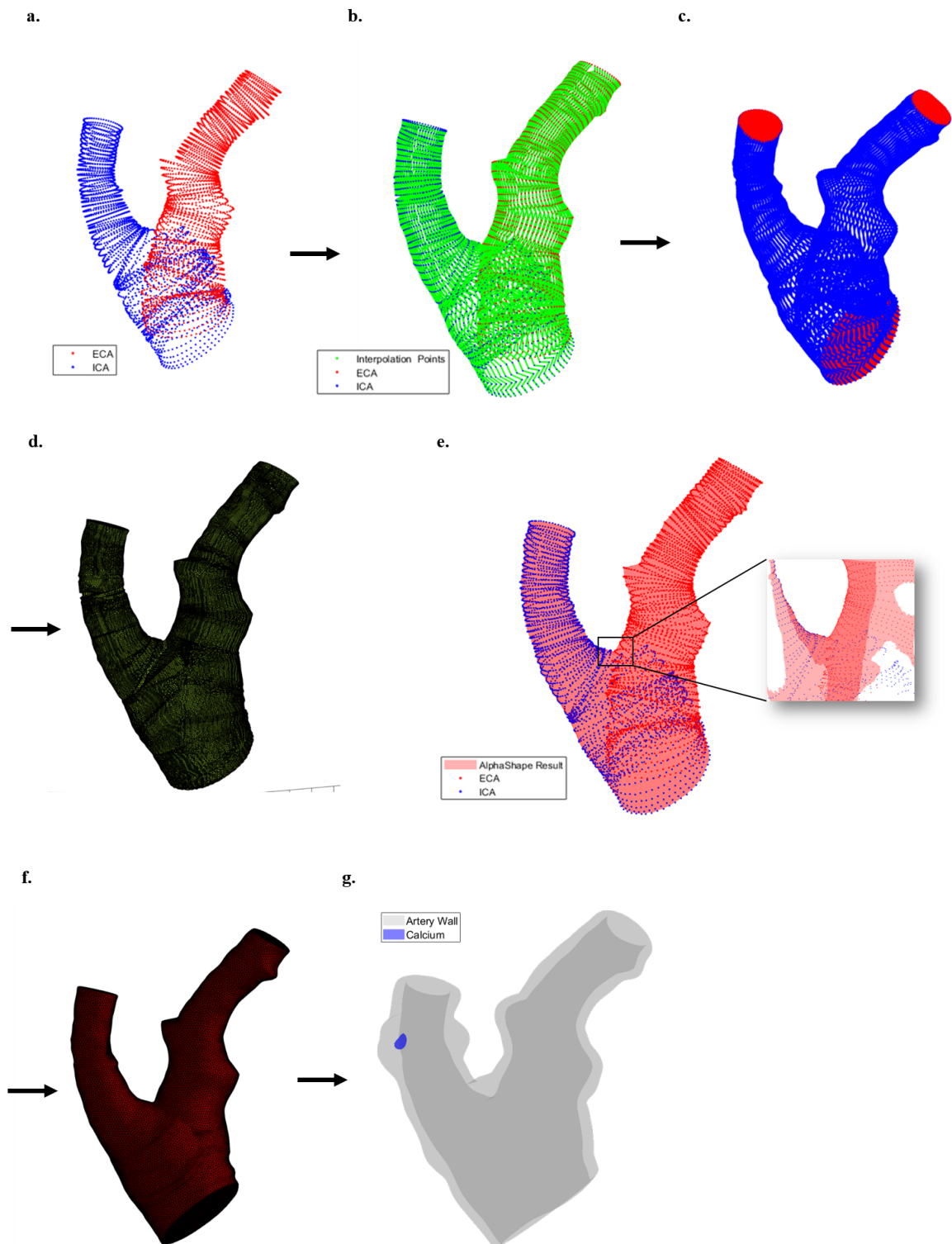


**Figure 2.1: Summary of surface reconstruction process.** a. The original ECA and ICA contours. b. Interpolate contours between adjacent contours. c. Cap the inlet and outlet surfaces. The figure only shows capping the ICA outlet. d. Alphashape result. e. Zoom-in plot of bifurcation. f. Remesh the surface using Geogram. g. Add Extension at CCA inlet. h. The previous process would repeat to create the vessel surface. The vessel was created by subtracting the vessel surface from the lumen surface.

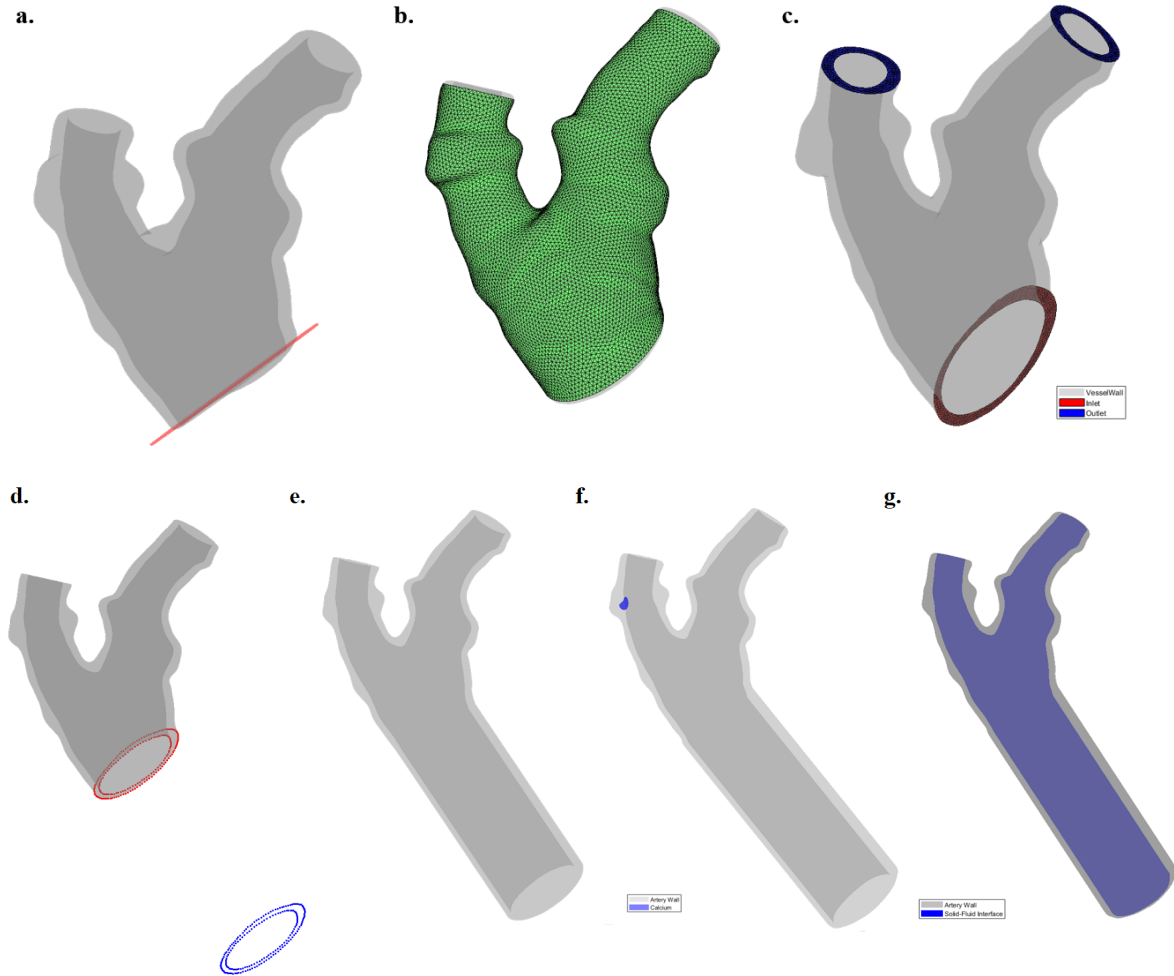


**Figure 2.2: Summary of geometry reconstruction process 2.** Artery Cutting: a. Artery and the red cutting cylinder. b. The original geometry (Grey) and geometry after cutting (Green). Extension: c. Inlet and outlet surface identification. d. The inner and outer rims of the inlet surface were lofted to create the extension. e. Geometry with inlet extension. Feature Detection: f. Calcium and artery. g. Solid-fluid interface.

## 2.3. Backward Incremental Method

After obtaining the 3D geometry of the artery, it was worth noting that the arteries had been pressurized during imaging or processing, leading to a certain initial stress state. Neglecting this initial stress and conducting simulations based on the measured geometry could introduce errors. The Backward Incremental (BI) method had previously been employed to account for the effects of initial stress [49]. The BI method was shown below. The lumen pressure was increased in  $opt\_iter$  iterations to the initial pressure  $p_i$ . In every iteration, a standard stress analysis was performed and the element-wise stress distribution was computed. The stress distribution was then used as the initial condition for the following iteration.  $\Omega_n$  was the geometry at pressure step  $n$ ,  $F_{a,b}$  was the deformation gradient between steps  $a$  and  $b$ ,  $I$  was the unity tensor,  $opt\_iter$  was the number of steps that required to reach initial-stress state,  $\sigma_n$  was the stress tensor,  $p_n$  was the pressure and  $G$  represents the material parameters.

This section focused on the second phase of the methodology, which centered around acquir-

ing initial stress through the application of the BI method. Since the BI method was not implemented into FEBIO, a software for nonlinear finite element analysis in biomechanics, within this chapter, two methods were proposed for implementing the BI method. To assess their robustness, both methods were put to the test using two different models.

---

**Algorithm 1** Pseudocode of backward incremental method

---

```

 $\Omega_0 = \Omega_{measured}$ 
 $F_{0,0} = I$ 
for  $n = 1$  to  $n = opt\_iter$  do
   $(F_{n-1,n}, \delta\sigma_n) = f(\Omega_{n-1}, F_{0,n-1}, \sigma_{n-1}, p_n, G)$ 
   $\Omega_n = \Omega_{n-1}$ 
end for

```

---

### 2.3.1. Implementation of Backward Incremental Method in FEBio

The previous implementation of the backward incremental method [49] employed the stress distribution from the preceding step as the initial condition for each subsequent step using Abaqus. However, the software used to conduct FSI in this project, FEBio, did not support a stress field as an initial condition. Instead, the applicable approach involved the use of the Prestrain feature [50]. The Prestrain feature defined a prestrain elastic material, which acted as a wrapper of the hyperelastic materials. The use of the Prestrain feature entailed a two-step analysis. In the initial step, a prestrain gradient was specified as input, and the geometry was deformed accordingly. Subsequently, in the second step, loading was applied to the model while the prestrain gradient was held fixed. An option also existed to provide an initial guess for the prestrain gradient and an update rule for the iterative determination of a compatible prestrain gradient that minimized mesh distortion. However, for this specific implementation of this project, this option remained unused.

Therefore, the goal was to obtain a deformation gradient as the input of further FSI simulation as the initial condition. Two methods have been come up with to implement the backward incremental method in FEBio:

- The first option involved utilizing codes from a previous project that performed the backward incremental method in Abaqus. In the final step, the pressure was set to 0 to obtain the zero-stress geometry. The resultant deformation gradient was taken as the prestrain input in FEBio.
- The second option involved using the prestrain deformation field, updated at each step, instead of the stress field. In the first stage, the intraluminal pressure was incrementally increased to the initial pressure of  $p_i$ . A standard stress analysis was then conducted, and the deformation gradient was computed. This gradient was subsequently applied element-wise in the following step. Once the initial stress state was achieved, the pressure was set to 0, thus the deformation gradient of zero-stress state to initial geometry was computed and used as input for further analysis.

In earlier applications of the backward incremental method, a 2D geometry was utilized, and stress was established as an initial condition in Abaqus[49]. Given the transition to a 3D geometry for this project, it became necessary to reevaluate the optimal iteration number in 3D.

Moreover, the two implementation methods were compared within the 3D geometry framework. To achieve this, the two implement methods first underwent validation.

### 2.3.2. BI Method Model Creation

In order to conduct BI method, finite element analysis (FEA) models were created. A mesh convergence study was performed to ensure the accuracy of the result (Appendix section C.1). Then, models were generated for each artery model to facilitate the implementation of backward incremental analysis. To achieve this, the surface structures were transformed into solid entities employing 4-node tetrahedral elements, a transformation process made possible through the utilization of the GIBBON toolbox [46]. The analysis process was automated through MATLAB code developed in-house.

#### Loading and Boundary Conditions

Figure 2.3 showed the boundary and loading condition of an example model. Blood pressure was applied on the inner luminal surface. Boundary conditions were defined to prevent any motion or rotation of the rigid body. The deformation of CCA inlet, ICA, and ECA outlets was constrained in three axes.

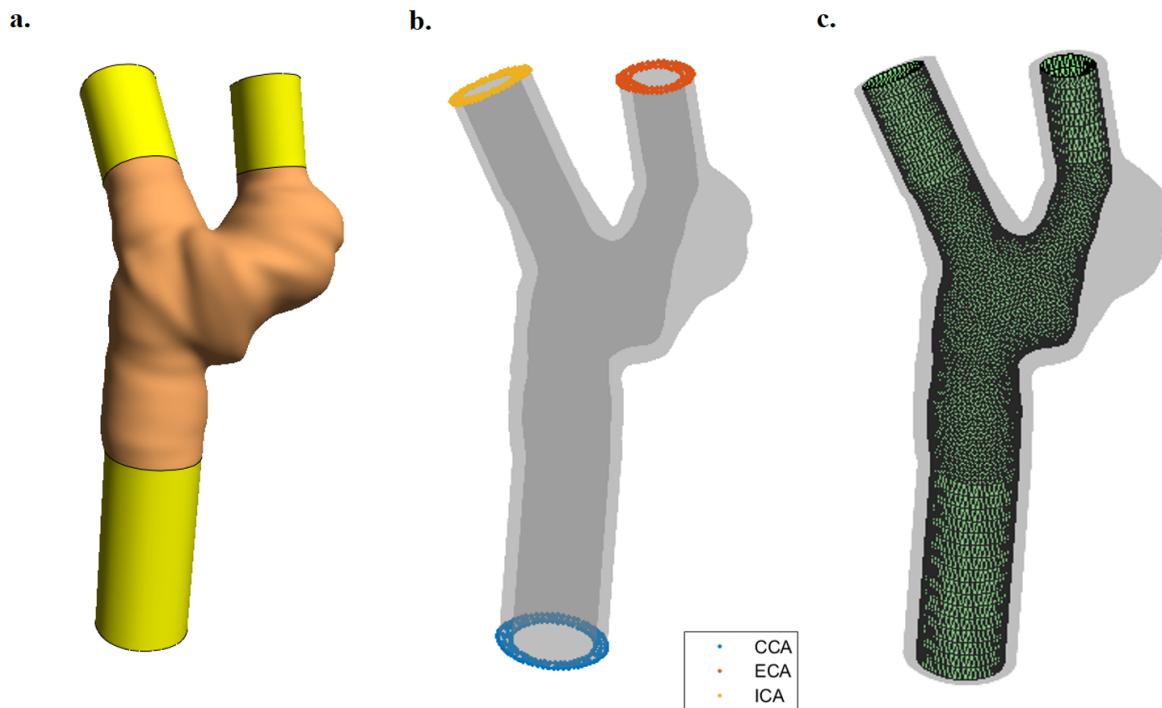


**Figure 2.3: Backward incremental analysis model.** a. The artery wall with inlet and outlet extensions (Extension: yellow). b. The deformations of the CCA, ECA, and ICA were constrained in all three axes. c. Pressure was applied to the lumen surface.

During backward incremental analysis, for each iteration, the prestrain deformation gradient was applied to the geometry the same as the first analysis step and the pressure was incrementally increased to the initial pressure. After 16 iterations, the initial stress stage was reached and then the result deformation gradient was exported. Since the CTA image was not electrocardiographic (ECG) gated, meaning that the exact time-point in cardiac cycle when the image

was taken was unknown. However, the systolic and diastolic pressure can be obtained, therefore the mean blood pressure  $p_{mean}$  was calculated using patient-specific systolic  $p_s$  pressure and diastolic pressure  $p_d$  as the initial pressure:

$$p_{mean} = p_d + \frac{1}{3}(p_s - p_d) \quad (2.1)$$

After the initial stress state was reached, the final deformation gradient would be calculated and utilized as the input for further simulation process.

### Material Model

Hyperelastic material models were employed to describe the behavior of solid components. Specifically, calciums and lipids were modeled using the isotropic Neo-Hookean material. The strain energy density function for the Neo-Hookean model was defined as:

$$W = \frac{\mu}{2}(I_1 - 3) - \mu \ln J + \frac{\lambda}{2}(\ln J)^2 \quad (2.2)$$

Here,  $I_1$  and  $I_2$  represent the first and second invariants of the right Cauchy-Green tensor  $C$ ,  $J$  is the determinant of the deformation gradient,  $\lambda$  stands for the first Lamé parameter, and  $\mu$  represents the shear modulus. The parameters used in the strain-energy function can be derived using Young's modulus  $E$  and Poisson's ratio  $\nu$ . The parameters were taken from literature [51][52].

$$\mu = \frac{E}{(1 + \nu)} \quad (2.3)$$

$$\lambda = \frac{\nu E}{(1 - 2\nu)} \quad (2.4)$$

The characterization of the artery wall's behavior employed the hyperelastic Ogden model. The strain-energy function was defined as follows:

$$\Psi = \sum_{p=1}^N \frac{\mu_p}{\alpha_p} (\lambda_1^{\alpha_p} + \lambda_2^{\alpha_p} + \lambda_3^{\alpha_p} - 3) \quad (2.5)$$

where  $\mu_p$  and  $\alpha_p$  were material constants,  $N$  ranged from 1 to 6, and  $\lambda_i$  were principal stretches. The material properties used in this model were obtained from tensile test data [53]. As the vessel was modeled using the same material, the average curve of the intima and vessel was first derived and subsequently employed as input for curve fitting. Abaqus Material Evaluation tool was then used to extract the material constants with varying values of  $N$ . The results were illustrated in the Figure B.13. Notably, starting from  $N$  values larger than 4, the results exhibited stability across all strain ranges. Therefore, an eight-parameter ( $N=4$ ) Ogden model was employed for analysis. The parameter settings for the solid components can be found in Table 2.1.

Given the utilization of the FEBio Prestrain feature, the material was set as *Uncoupled Prestrain Elastic*, employing the *Ogden* model. The *Prestrain Gradient* option was selected for prestrain.

**Table 2.1:** Material parameters of solid components.

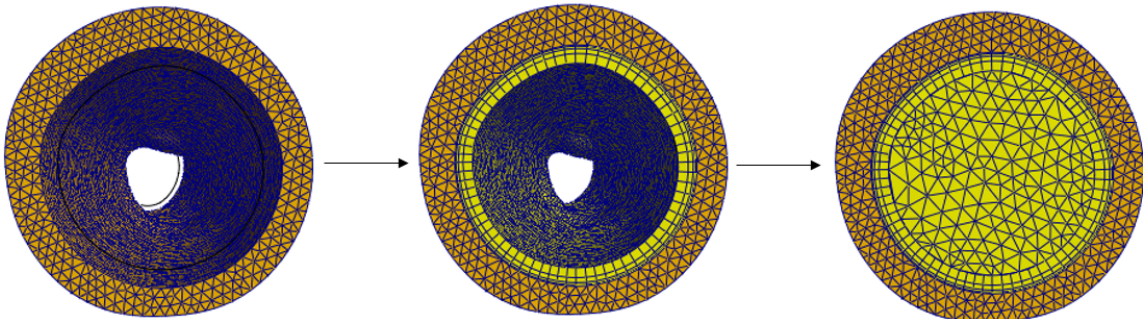
Calcium		Vessel Wall	
model	Neo-Hookean	model	Ogden
E	$10^7$ Pa	$\mu_1$	-18.69MPa
$\nu$	0.48	$\mu_2$	9.32MPa
$\rho$	$1000 \text{ kg/m}^3$	$\mu_3$	21.46MPa
<b>Lipid</b>		$\mu_4$	-12.05MPa
model	Neo-Hookean	$\alpha_1$	6.1Pa
E	$2 \times 10^4$ Pa	$\alpha_2$	7.02Pa
$\nu$	0.48	$\alpha_3$	4.95
$\rho$	$1000 \text{ kg/m}^3$	$\alpha_4$	4.86
		$\rho$	$1000 \text{ kg/m}^3$

## 2.4. Fluid-Structure Interaction Model Creation

Blood simulation was carried out via a Fluid-Structure Interaction (FSI) analysis using the open-source finite element software FEBio. A detailed explanation of the implementation of FSI in FEBio was provided in Appendix D.1. Initially, a mesh sensitivity test for the fluid domain was conducted using the right carotid artery model from one of the patient (Appendix C.2). Following this, FSI models were developed, incorporating patient-specific inlet and outlet boundary conditions over two cardiac cycles.

### 2.4.1. Mesh Preparation

The preparation of the FSI model was initiated with the solid model from the previous section. Subsequently, the boundary layer was extracted. The thickness of the boundary layer was set as 6mm according to Reynolds's number at peak flow in the carotid artery [54][55]. The mesh was built by penta6 elements featuring a bias of 2 and 6 segments. The process was shown in Figure 2.4. The residual fluid domain was delineated using tet4 elements with an element size of 0.3 mm. To ensure the robustness of the model, a mesh convergence analysis was conducted (Appendix C.2).

**Figure 2.4:** Top view of the ICA outlet during the boundary layer creation process.

### 2.4.2. Material Model

The model consisted of four key components: blood, vessel wall, calcium, and lipid. The material models utilized for solid components were explained in section 2.3.2. While blood typically exhibited Newtonian fluid behavior in large arteries, the presence of arterial stenosis had been observed to influence the hemodynamic behavior of blood flow [56]. To address this, a non-Newtonian model was employed, which demonstrated superior predictive capabilities for wall shear stresses [57] and the ability to capture the tapering effect [58]. In this model, blood was characterized as an incompressible non-Newtonian Carreau fluid with a density of  $1,060 \text{ kg/m}^3$ . The viscosity was calculated using the following formula:

$$\mu = \mu_{\infty} + (\mu_0 - \mu_{\infty})[1 + (\lambda\dot{\gamma})^2]^{\frac{n-1}{2}} \quad (2.6)$$

In this equation,  $\mu$  represented fluid viscosity,  $\mu_0$  was the viscosity at zero shear rate,  $\mu_{\infty}$  was the viscosity at infinite shear rate,  $\lambda$  was the characteristic time,  $\dot{\gamma}$  was the shear rate, and  $n$  was the power index. The material properties were set as follows in Table 2.2.

**Table 2.2:** Material parameters of fluid [59]

<b>Blood</b>	
model	Carreau fluid
$\mu_0$	$0.056 \text{ Pa} \cdot \text{s}$
$\mu_{\infty}$	$0.00345 \text{ Pa} \cdot \text{s}$
$\lambda$	$3.313 \text{ s}$
$n$	$0.3564$
$k$	$2.2 \times 10^9 \text{ Pa}$
$\rho$	$1060 \text{ kg/m}^3$

### 2.4.3. Loading Conditions

The deformation of solid domain was constrained at both the inlet and outlet surfaces to prevent any potential rigid body motion. Additionally, to ensure a non-slip condition, the fluid velocity at the solid-fluid interface was set to zero. To enable the solid to deform in response to fluid stresses, a *Fluid-FSI traction* boundary condition was imposed along the solid-fluid interface. This condition facilitated the accurate representation of the interaction between the solid and fluid domains.

In terms of flow dynamics, a transient flow curve was applied at the inlet, derived from the average flow curve [60]. For each patient, the mean flow was estimated based on the radius of the CCA inlet, and the average flow curve was then scaled accordingly (Figure 2.5). A heart rate of 68 beats per minute was considered, and a parabolic flow profile was employed. For the outflow boundary condition, a ratio of internal carotid artery flow to external carotid artery flow was considered as 0.64:0.36 since the vessels did not exhibit severe stenosis [61]. The boundary condition at outflow was applied by using the distal vascular resistance model [62]:

$$p = RQ + p_0 \quad (2.7)$$

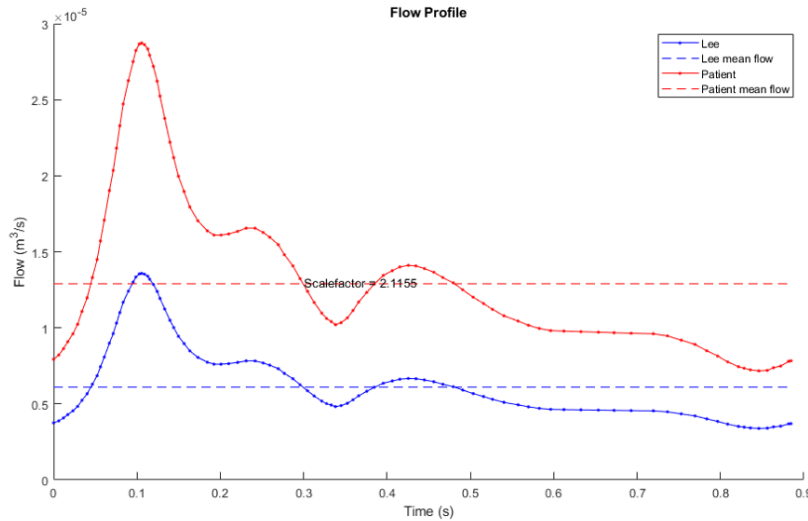


**Figure 2.5:** Inlet flow profile of average flow from Lee's study [60] and the scaled curve.

where  $p$  was outflow pressure,  $R$  was the distal vascular resistance,  $Q$  was the flow, and  $p_0$  was the reference pressure. When reference pressure was set as zero, the outflow resistance can be calculated as the ratio of mean pressure to mean flow [63]. In addition, backflow and tangential stabilization were prescribed on outlet faces with  $\beta = 1$  [64].

#### 2.4.4. Simulation Setting

FEBio *Fluid-FSI* module was utilized for the simulation (Dev Version 2.3.0.0654ab787). The coefficients of boundary conditions, velocity, and prestrain deformation gradient were ramped up from zero to their initial values within the first 0.1 seconds to ensure convergence of the model. Subsequently, the simulation was conducted over two complete heart cycles. The first cycle was utilized for initialization, while the second cycle provided the data for analysis. The time step was set to 0.01 seconds. To guarantee the reliability of the results, the simulation was performed on one artery model for four cycles. The outcomes from the 2nd and 4th cycles were compared for validation (Appendix D.2).

## 2.5. Sector Creation

Sectors were created to prepare the data from previous steps for subsequent analysis. Initially, morphological metrics were acquired to evaluate the atherosclerotic carotid geometry at both baseline and follow-up. The changes between the two time points represented atherosclerotic progression over time. Subsequently, the outcomes from FSI simulations were processed. These results can be employed to characterize the stress in correlation with plaque progression in each case. The results on extension and ECA were not shown in 2D map plot as well as further analysis.

VMTK toolbox was employed to determine the centerline of the vessel geometry and partition the input structure into three distinct segments (Figure 2.6a). The result of ICA-CCA was saved for future analysis. Additionally, two supplementary arrays—AbscissaMetric and AngularMetric—were generated for each branch. The former was derived from the curvilinear

ear distance along the centerlines, while the latter represented the circumferential coordinate of mesh points around the centerlines ( $+\pi, -\pi$ ). The final result was mapped in sectors based on these two arrays with the AbscissaMetric on the x-axis and AngularMetric on the y-axis and stretched to account for the presence of insertion regions at bifurcations. In this 2D map configuration, the arteries were divided into cross-sectional segments of 1.5mm along the centerline. Subsequently, these segments were divided into 8 sectors of  $45^\circ$  with the lumen center as the center (Figure 2.6e). The foundation is based on an in-house written code and a method described in [65].

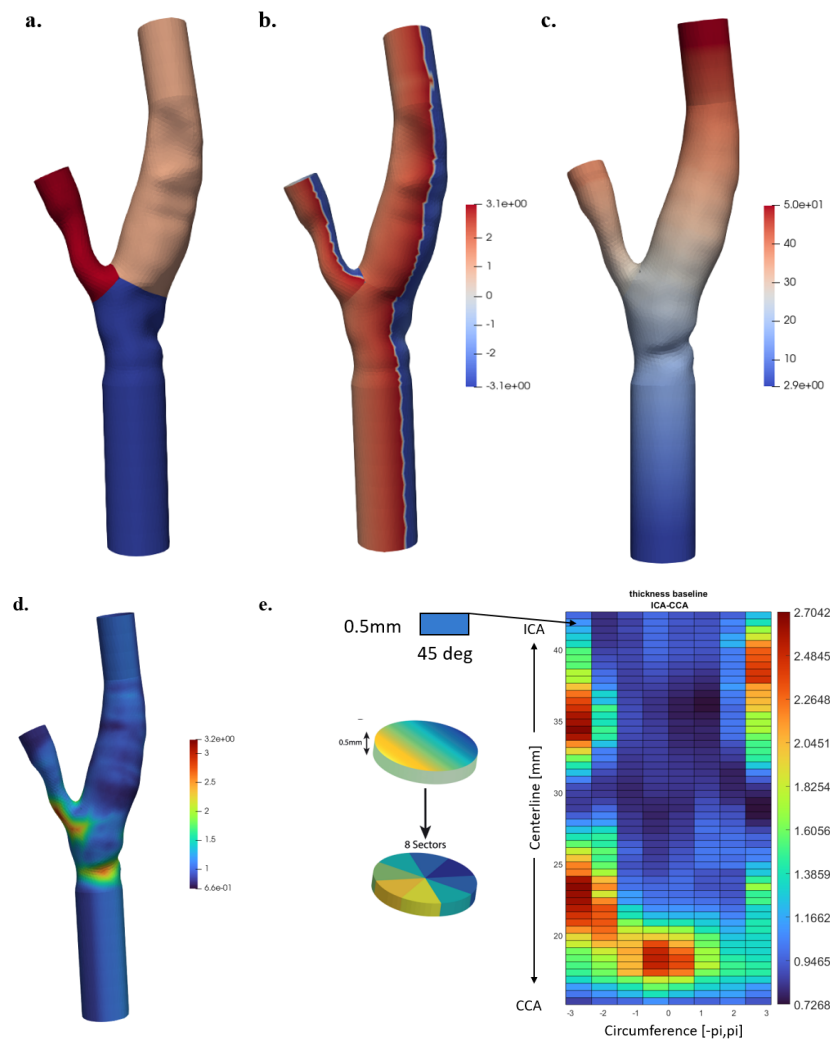


**Figure 2.6: 3D to 2D map process.** a. Three branches were identified. b. Circumferential coordinate of mesh points around the centerlines ( $+\pi, -\pi$ ). c. Distance along the centerlines (mm). d-e. Example of wall thickness result mapped to each sector. The artery was divided into thin cross-sectional slices of 0.5mm and grouped into eight sectors ( $45^\circ$ ). The 2D map shows the vessel circumference on the x-axis and the distance along the centerline on the y-axis.

### 2.5.1. Morphological Metrics

In order to simplify the analysis process, morphological metrics were derived by reconstructing the lumen and vessel surface without extension. The baseline and follow-up geometries were

firstly co-registered. The co-registration process involved fitting the centerline of ICA-CCA longitudinally and circumstantially, as well as matching the two flow divider points. Subsequently, the results from the follow-up were projected onto the baseline geometry before the 3D-to-2D mapping process, enabling accurate calculation of changes between the two time points per sector. Three morphological metrics were extracted from both baseline and follow-up ICA-CCA structures: wall thickness, calcium location, and plaque burden.

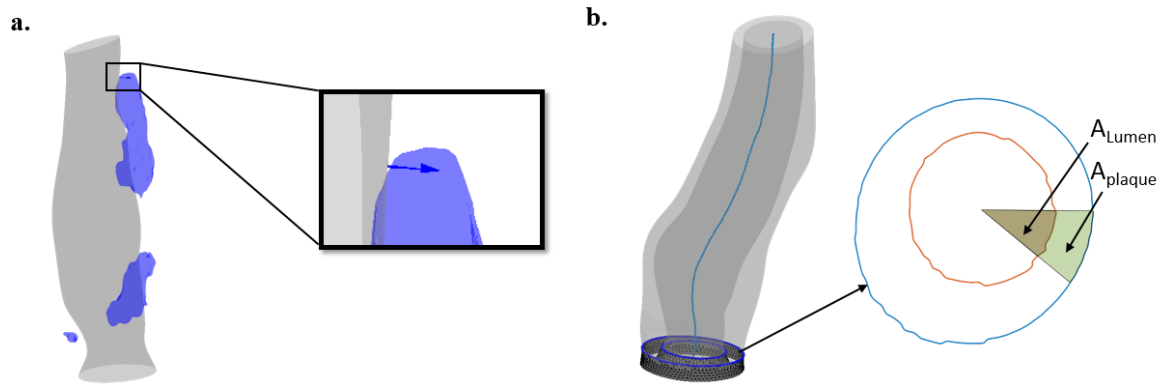


**Figure 2.7: Post-processing of morphological metrics.** a. Ray-tracing method. If the interaction was found from a node along its normal direction towards the calcium structure, calcium presence was identified and the distance was computed. b. A cross-section was generated perpendicular to the centerline for the calculation of plaque burden. Plaque burden was computed utilizing the lumen area and vessel area.

Wall thickness was computed as the distance between the lumen surface and the vessel surface using the ray tracing method. To determine the distance between calcium and the lumen surface, a ray-tracing method was employed for each node on the lumen surface to identify the presence of calcium (Figure 2.7a). This method involved tracing a line from each node in its normal direction towards the calcium structure. If an interaction was detected, the node was marked as having calcium presence. The point-wise distance between calcium and the identified nodes was calculated. Additionally, to determine the plaque burden for each sector, the vessel wall was divided into 200 cross-sections. The resulting lumen curve and vessel curve were then segmented into eight circular sectors to calculate the plaque burden for each sector (Figure 2.7b). A piecewise cubic hermite interpolating polynomial (pchip) method [66] was employed to fit the plaque burden results to the 2D map, with sector settings consistent with other results.

### 2.5.2. Biomechanical Metrics

The results obtained from the simulation underwent several post-processing steps to enhance understanding of the simulation outcomes and facilitate further analysis. Shear stresses were extracted from both the solid and fluid interfaces, along with the von Mises stress from the vessel-flow interface. The time-average value, maximum, and minimum over a cardiac cycle were computed. To understand the stress distribution within vessel structure, the average of structural von Mises stress was computed in the radial direction and visualized on the lumen surface. These findings were subsequently converted into a .tec file format and mapped to the

2D sector plot.

**Table 2.3:** Biomechanical Metrics

	<b>Description</b>
<b>Fluid TAWSS</b>	Fluid shear stress on lumen surface averaged over a cycle.
<b>Solid TAWSS</b>	Solid shear stress on lumen surface averaged over a cycle.
<b>TAVMS Average</b>	Von Mises stress averaged over a cycle and average in radial direction.
<b>TAVMS Interface</b>	Von Mises stress on lumen surface over a cycle.

# 3

## Results

### 3.1. Model Reconstruction

Patient-specific model reconstruction was undertaken for 160 vessels from 80 patients in the PARISK dataset at baseline. The requisite data were stored in .mat files and subsequently exported as STL files. The geometries of vessel wall were separately shown in Appendix A.

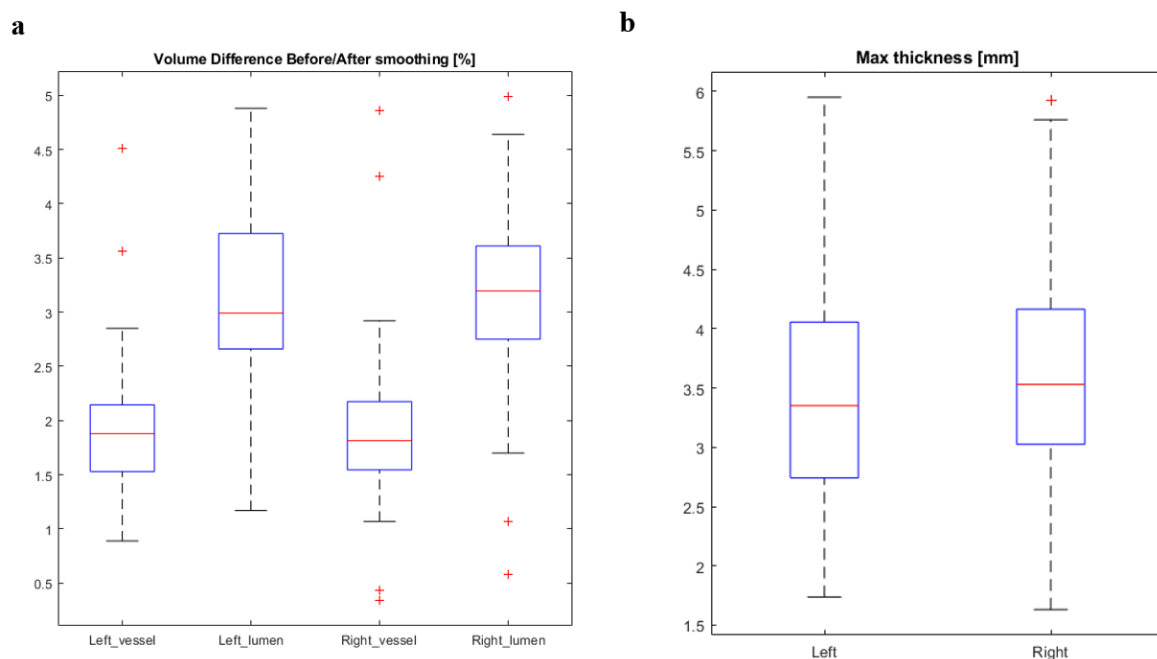


**Figure 3.1:** a. Distribution of percentage difference of volume change before and after smoothing and remeshing process. b. Distribution of maximum wall thickness.

To assess the quality of the final geometry, the percentage difference in volume change was calculated between the alpha shape result and the structure intended for further Boolean subtraction. The results were presented in Figure 3.1 and Table 3.1. On average, across all the structures, the percentage difference was 2.54%, with a standard deviation of 0.96. Notably, the largest percentage difference observed in the lumen structure was 4.99%. Both the left and

right vessel structures exhibit lower average percentage differences, with values of 1.91% and 1.90%, respectively. This demonstrated the overall robustness of the reconstruction process.

**Table 3.1:** Results for the percentage difference of volume change [%]

	<b>Left_vessel</b>	<b>Left_lumen</b>	<b>Right_vessel</b>	<b>Right_lumen</b>
<b>Minimum</b>	0.89	1.17	0.34	0.58
<b>Maximum</b>	4.51	4.88	4.86	4.99
<b>Average</b>	1.91	3.16	1.90	3.19
<b>Standard Deviation</b>	0.57	0.83	0.64	0.78

The wall thickness was determined by measuring the closed distance between the lumen surface and the vessel surface before the extension was added. The analysis of maximum wall thickness for both left and right carotid arteries was presented in Table 3.2. The recorded measurements ranged from a minimum of 1.63 mm to a maximum of 5.92 mm, with an average thickness of 3.39 mm for the left artery and 3.65 mm for the right artery. A wall thickness exceeding 1.50 mm was considered as a well-established criterion for identifying diseased regions [67]. All 160 cases exhibited maximum wall thickness values surpassing the threshold of 1.50 mm, reaffirming the presence of diseased regions across the patients.

**Table 3.2:** Results for maximum wall thickness of the artery [mm]

	<b>Left</b>	<b>Right</b>
<b>Minimum</b>	1.74	1.63
<b>Maximum</b>	5.95	5.92
<b>Average</b>	3.39	3.65
<b>Standard Deviation</b>	0.89	0.91

## 3.2. Validation of Backward Incremental Method

The arteries had already undergone deformation during imaging, resulting in a specific initial stress state. To address this, the Backward Incremental method was utilized. The earlier applications of the backward incremental method were performed on a 2D geometry, and stress was established as an initial condition in Abaqus[49]. Therefore, the two implementation methods were then underwent validation. An interaction process for reaching the initial stress state occurred in stage 1, followed by the application of the desired pressure in stage 2.

The first validation utilized a simple ring model. The simulations were performed using three different iterations (16, 24, and 32). The stress distribution at the initial stress stage (Stage 1) and after final pressure was applied (Stage 2) were extracted. The detail explanation and result of this model was presented in Appendix B.1. With increasing iteration numbers, there were slight variations in the stress values for all methods and stages. Method 1 exhibited a higher difference than Method 2 across all iterations and stages. Therefore, using an iteration number of 16 showed promise.

The second validation utilized an artery model from a patient. The artery model was achieved

through the reconstruction process outlined in the previous section. For simulation simplicity, the geometry prior to the creation of the extension was employed. The tetrahedral mesh was then generated utilizing the GIBBON toolbox within MATLAB [46]. For material properties, a nonlinear hyperelastic Neo-Hookean model was utilized, with detailed parameters outlined in 2.3.2. The specific values chosen were  $E = 0.6$  MPa for Young's modulus and  $\nu = 0.4$  for Poisson's ratio [52]. Given the utilization of the FEBio Prestrain feature, the material was set as *Prestrain Elastic*, employing the *neo-Hookean* hyperelastic model [50]. Additionally, constraints were imposed on the deformations of one inlet curve and two outlet curves along all three axes.

Tests were carried out with 16 and 24 iterations, aiming to conduct a comparative assessment of resulting stress distributions and computational times, considering different optimal iteration steps and two implementation methods. The initial pressure was set at  $p_i = 13.3$  kPa and the final pressures were specified at 18 kPa. The entire process is illustrated in Figure 3.2. The stress distribution at the initial stress stage (Stage 1) and after final pressure was applied (Stage 2) were extracted. It is noteworthy to mention that, unlike the prior ring model, the zero-stress geometry and correct initial stress distribution were unknown, resulting in a lack of reference results for this artery model. Therefore, resultant stress obtained from a BI process completely in Abaqus was utilized for comparison.

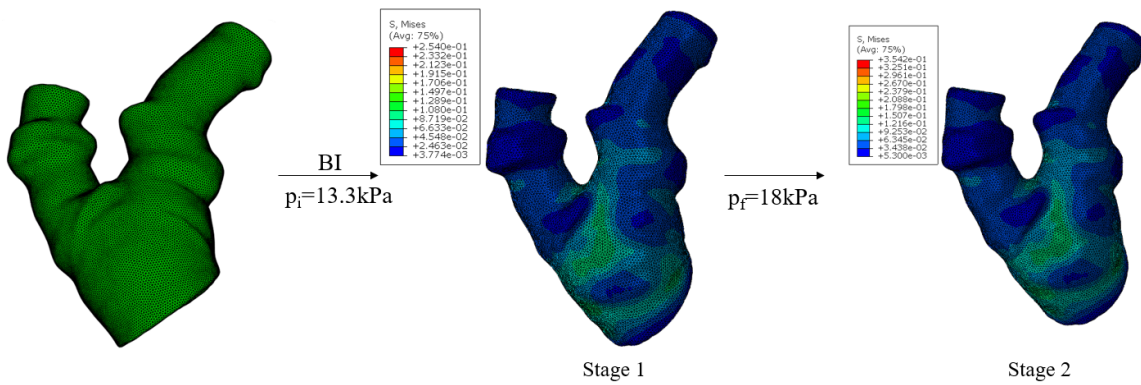


**Figure 3.2: Verification using artery model with  $\text{opt\_iter} = 16, 24$ .** Backward incremental analysis with  $p_i = 13.3$  kPa. The  $p_f$  was set as 18 kPa.

The artery model from the real carotid artery was utilized. Iterations 16 and 24 were tested using the two different methods. The stress distribution of each model was displayed in Appendix B.1. Unlike the ring model, the true initial stress state of this artery model was unknown. Therefore, a result obtained from a complete analysis in Abaqus was used for comparison. The estimation of von Mises stress showed a higher value than the abaqus result for both methods (Table B.1). However, method 2 was closer to the Abaqus result. Additionally, Method 1 took 53 minutes while Method 2 took 36 minutes to complete the analysis. Taking all factors mentioned above into consideration, the Backward Incremental method will be applied using Method 2 with an iteration number of 16.

**Table 3.3:** Maximum Von Mises Stress Results of Artery Model for Different Methods and Iteration Numbers [kPa]

	Abaqus		Method 1		Method2	
	Stage 1	Stage 2	Stage 1	Stage 2	Stage 1	Stage 2
<b>i=16</b>	265.03	354.27	284.13	389.72	267.29	376.99
<b>i=24</b>	265.03	354.36	302.51	414.25	267.35	372.91

### 3.3. FSI Results: Patient 1L

Three patients with lipid presence on one side and calcium on both sides of the carotid artery were chosen for FSI simulation from the PARISK dataset, denoted as Patient 1, 2, and 3, respectively. In this section, the FSI result of Patient 1L was explained in detail. The progression of plaque between baseline and follow-up was analyzed, using calcium distance, wall thickness, and plaque burden. Subsequently, the simulation results were presented. Biomechanical stresses, including wall shear stress and von Mises stress, were discussed, followed by an illustration of the flow pattern.

#### Morphological Metrics

In Figure 3.3ab, the carotid artery and calcium within the vessel of Case 1L at baseline and follow-up were shown. Growth of calcium in volume and size was observed, and severe stenosis was identified in CCA for follow-up vessel structure. Diseased regions were identified as areas with a thickness greater than 1.5 mm [67]. The percentage of diseased regions increased from 28.85% (193/460) to 42.24% (235/460), signifying plaque development (Figure 3.3cd). The total volume of calcium increased from 48.31 mm<sup>3</sup> to 92.58 mm<sup>3</sup>.

Among all three calcium, the one located at the lowest point exhibited the largest volume change (20.07 mm<sup>3</sup>), aligning with the location of severe stenosis in CCA. A new calcium was also observed near this region, indicating potential calcification within the same plaque. The increase in wall thickness was concentrated in the region where calcium grew most, reaching a maximum value of 2.98 mm. A high plaque burden of 96.7% was observed in the same region of follow-up CCA (Figure 3.4) as well as a high plaque burden difference of 66.67%. In addition to the concentrated region in CCA, an increase in thickness was observed in ICA. The calcium volume increased second largest (14.54 mm<sup>3</sup>), coinciding with the observation of lumen stenosis and an increase in diseased wall thickness regions.

On the other hand, a thinner vessel and a smaller plaque burden also appeared in the follow-up data, located at the distal end of ICA and the proximal end of CCA (Figure 3.3g and Figure 3.4c). While the number of sectors with detected calcium increased by 17, the change in distance between calcium and the lumen surface was not consistent across all sectors. Figure 3.5 illustrated the change in calcium distance. In 43.14% (22/34) of sectors, calcium moved closer to the lumen, while 29 sectors exhibited a thickened cap.

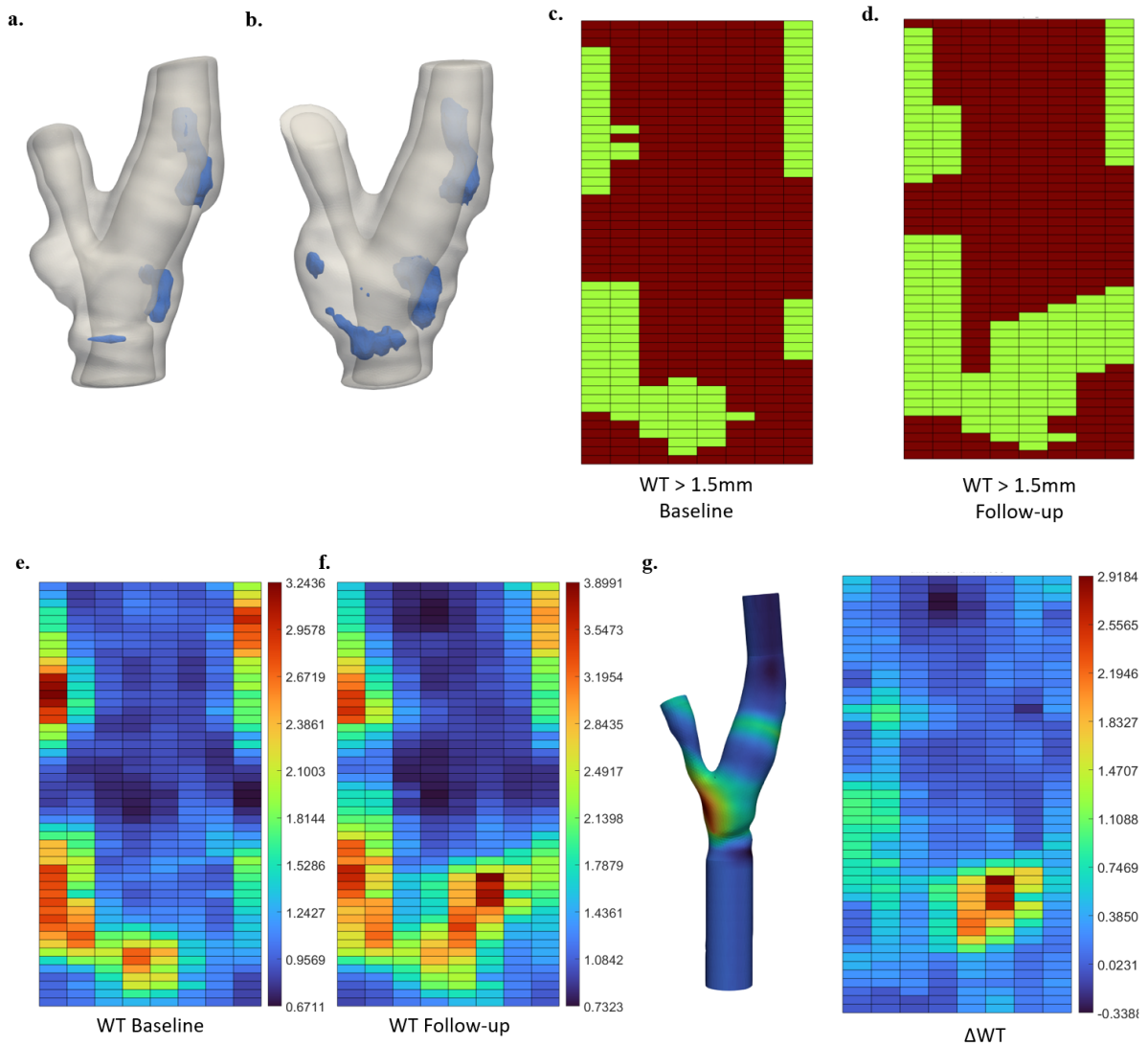


**Figure 3.3:** a. Baseline carotid artery of patient 1L. b. Follow-up carotid artery of patient 1L. Blue: calcium. c. Diseased wall thickness region ( $>1.5\text{mm}$ , green) of baseline ICA-CCA. d. Diseased wall thickness region ( $>1.5\text{mm}$ , green) of follow-up ICA-CCA. e. The wall thickness of baseline ICA-CCA (mm). f. The wall thickness of follow-up ICA-CCA (mm). g. Change of wall thickness in ICA-CCA (mm). (WT: wall thickness;  $\Delta\text{WT}$ : baseline wall thickness follow-up wall thickness)

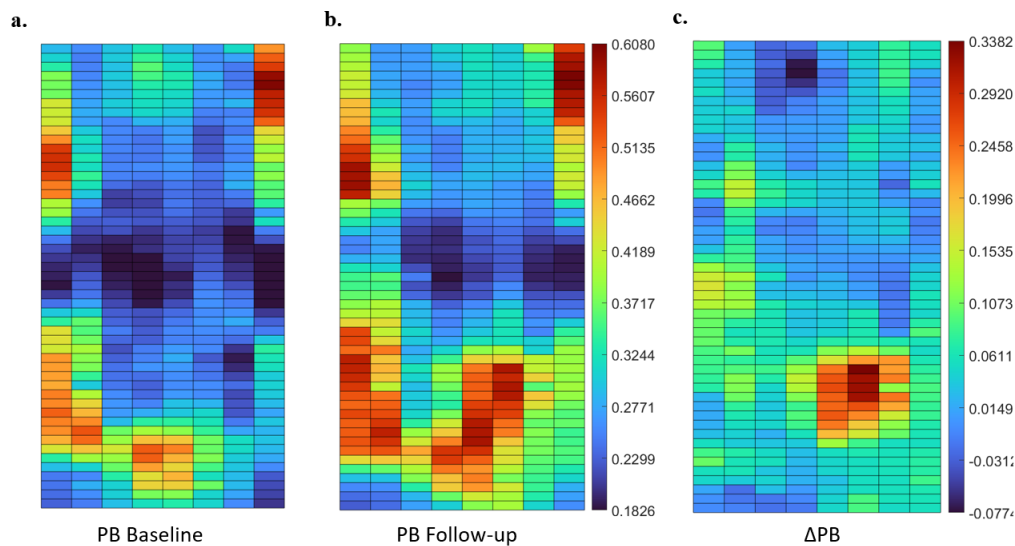


**Figure 3.4:** a. Plaque burden of baseline ICA-CCA. b. Plaque burden of follow-up ICA-CCA. c. Change of plaque burden in ICA-CCA. (PB: plaque burden;  $\Delta$ PB: baseline plaque burden-follow-up plaque burden)

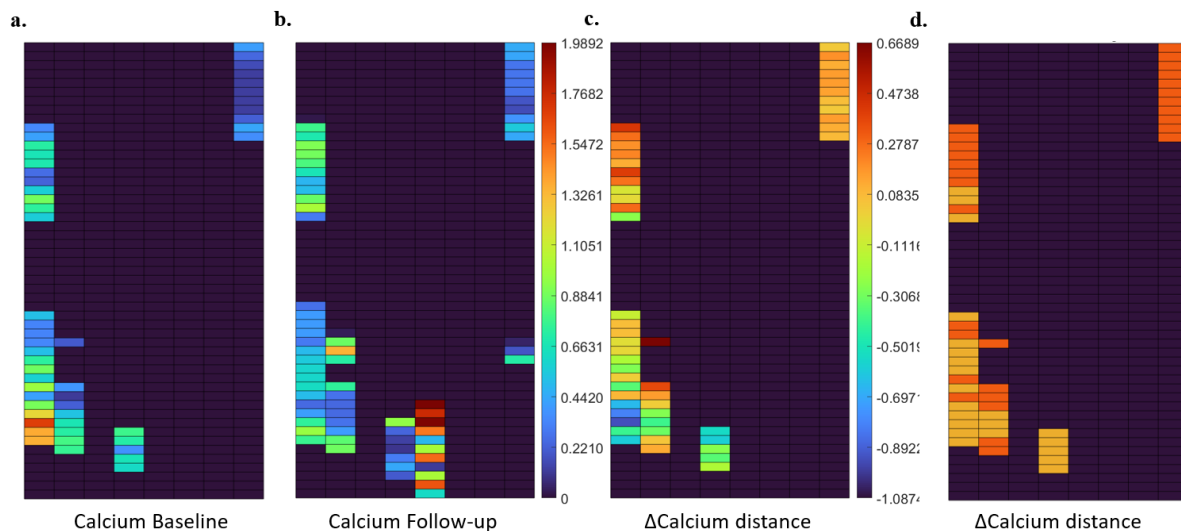


**Figure 3.5:** a. Distance between calcium and lumen of baseline ICA-CCA. b. Distance between calcium and lumen of follow-up ICA-CCA (mm). c. Change of calcium distance of ICA-CCA (mm). (Orange:  $\Delta$ calcium distance $>$ 0; Yellow: $\Delta$ calcium distance $<$ 0)

### Biomechanical Metrics

Fluid time-average wall shear stress (TAWSS) at the lumen surface was shown in the Figure 3.6a. Figure 3.6 b showed the low fluid TAWSS plot where high and median fluid TAWSS ( $>$ 1Pa) was filtered out. Subsequently, the ECA was eliminated, and data for ICA and CCA were mapped into a 2D sector plot (Figure 3.6c). The image revealed that the highest fluid TAWSS was present at the bifurcation and ECA where the lumen radius was small. Higher fluid TAWSS was also observed along the inner wall of the bifurcation. Low fluid TAWSS occurred in the plaque regions, corresponding to the area where diseased wall thickness and increased plaque burden appeared.

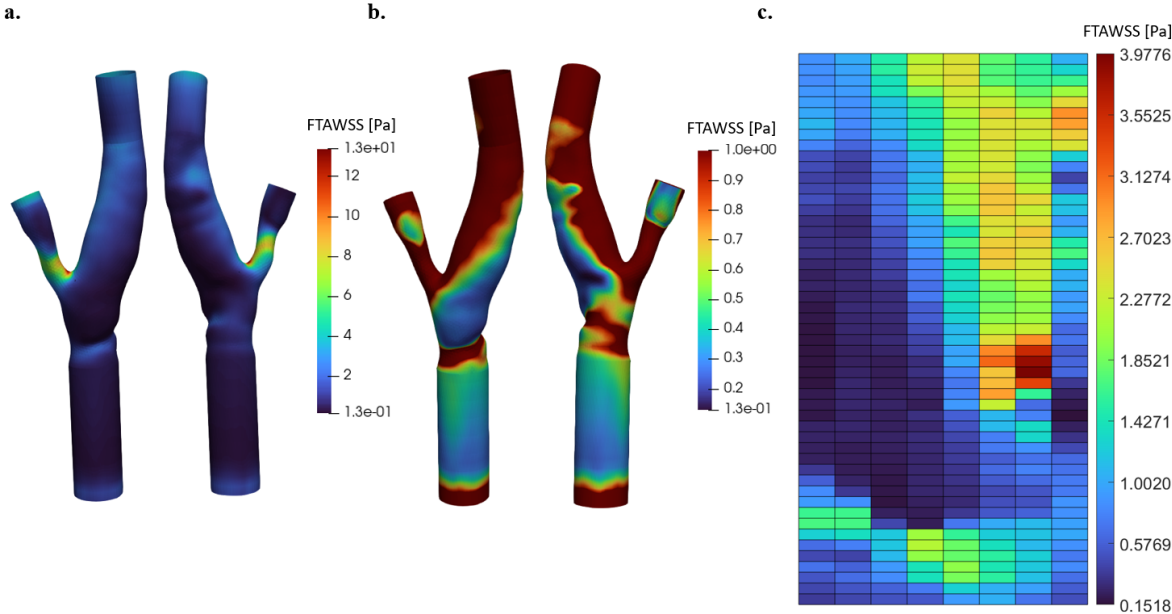


**Figure 3.6: Fluid time-average wall shear stress (TAWSS) of case 1L at lumen surface.** a. Front view and back view of Fluid TAWSS. b. Low Fluid TAWSS plot. Stress larger than 1Pa was eliminated. c. 2D map plot of ICA-CCA FTAWSS.

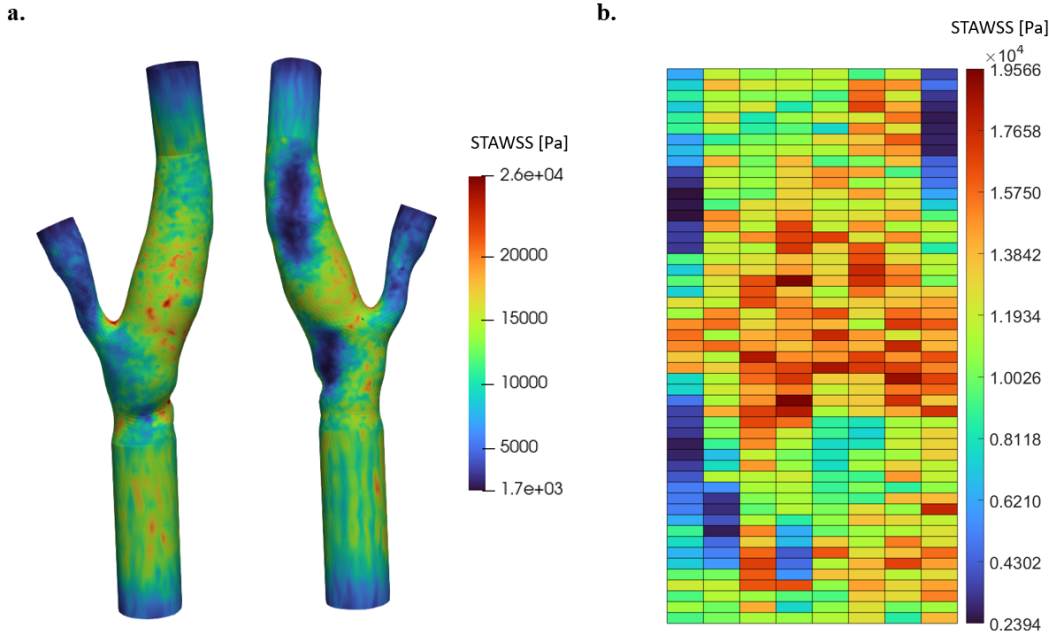


**Figure 3.7: Solid time-average wall shear stress (TAWSS) of case 1L at lumen surface.** a. Front view and back view of Solid TAWSS at lumen surface. b. 2D map plot of ICA-CCA Solid TAWSS at lumen surface.

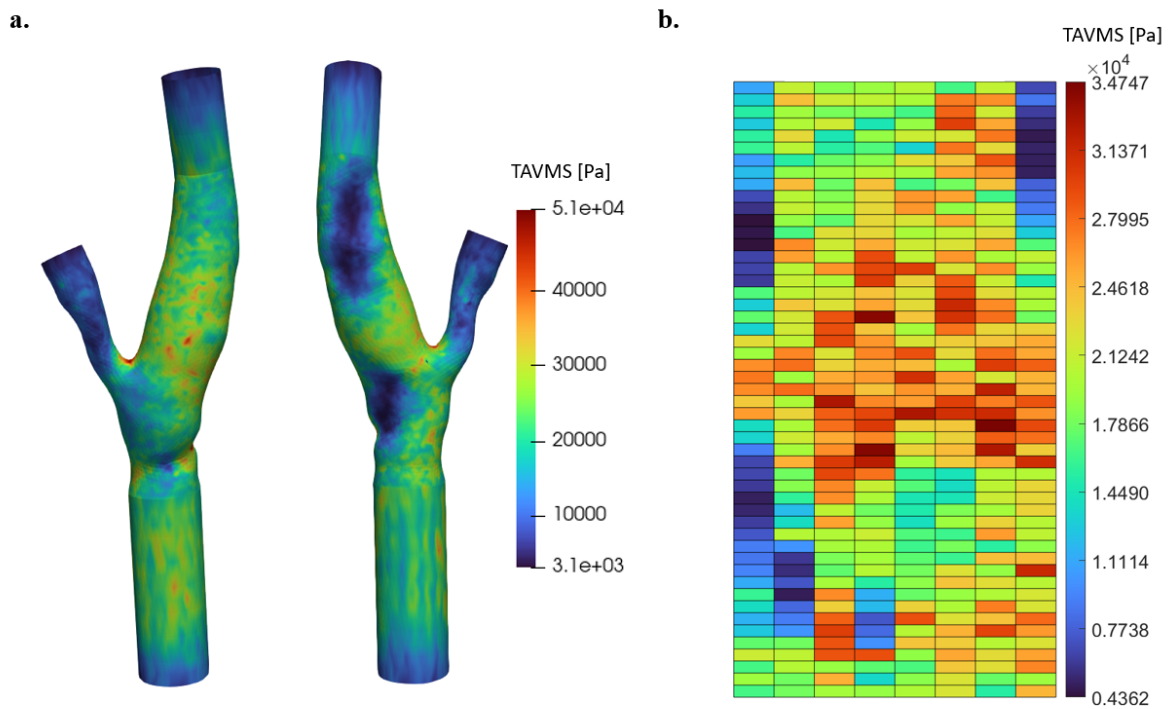


**Figure 3.8: Time-average von Mises stress (TAVMS) of case 1L at lumen surface.** a. Front view and back view of TAVMS at lumen surface. b. 2D map plot of ICA-CCA TAVMS at lumen surface.

Similar distributions were observed in the solid TAWSS and time-average von Mises stress (TAVMS) of the vessel wall on the interface (Figure 3.7 and Figure 3.8). The highest stress was present at the bifurcation while low stresses were concentrated in the regions with calcium. When compared with fluid TAWSS, although the highest solid shear stress was also identified at the flow divider point as fluid shear stress, no significant occurrence of high solid shear stress in ECA was observed. Nonuniform stress was shown at the side wall without calcium, while lower stress was observed in the plaque region.

In addition to the interface, the time-average von Mises stress was also determined by calculating the average value in the radial direction (Figure 3.9). This value provided insight into the stress distribution in the vessel wall. Lower stress was observed at the calcified region in ICA; however, for the other two calcium, local high stress was evident. Cut-view plots of the two calcium regions were presented in Figure 3.9c. In comparison to other calcified areas, the calcium exhibited a spindle pattern with tapered ends. The sharp corners led to stress concentration due to significant discontinuities in geometry [68], resulting in the local high average TAVMS.

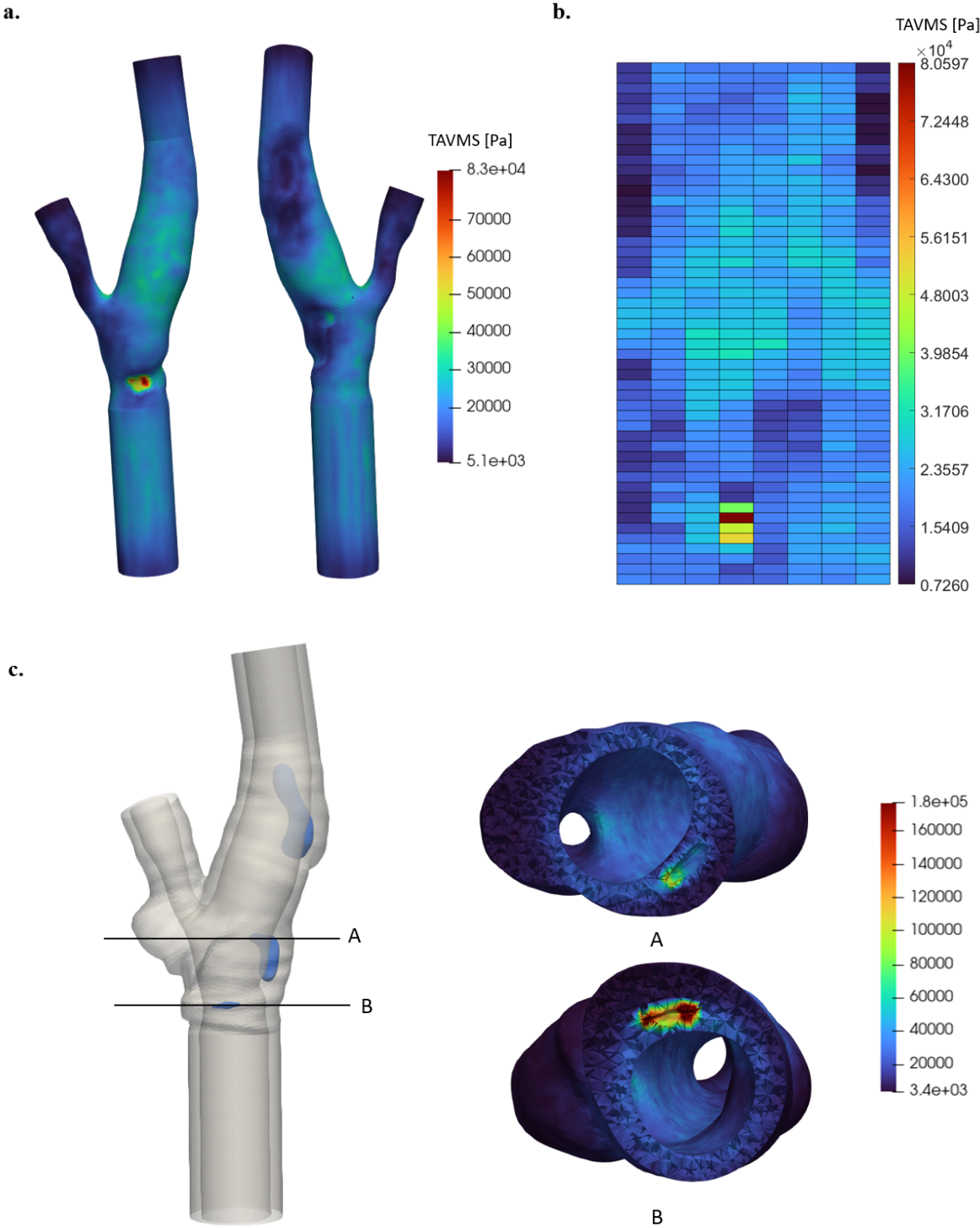


**Figure 3.9: Radial average solid time-average von Mises stress (TAWMS) of case 1L.** a. Front view and back view of radial average TAWMS. b. 2D map plot of ICA-CCA radial average TAWMS. c. Cutview plot of time-average von Mises stress at planes A and B (Pa).

### Flow Pattern

While parameters related to flow behavior were not utilized as metrics for later analysis, it was demonstrated that wall stress was closely related to flow behavior [21]. In this section, the flow patterns at different positions of the bifurcation and various time points within the cardiac cycle were explained.

Figure 3.10 presented an overview of velocity profiles in the plane of the bifurcation at 0.5s after peak systolic. Initially, the velocity exhibited a symmetric profile in CCA before entering the plaque region. Proximal to the bifurcation, a laminar flow with streamlines parallel to the vessel wall was observed. However, the presence of calcium, indicating local lumen stenosis, disrupted the flow, resulting in an asymmetric pattern at position E with skewing opposite to the calcium regions. Subsequently, flow separation occurred, generating secondary flows due to the deflection of the main flow at the flow divider. In the ICA bulb region (from Position D to B), velocities were highest near the flow divider, while flow separation and recirculation were observed on the side opposite the bifurcation. Moving from position C to B, a crescent shape was formed due to the increased transport of flow around the circumference of the tube [69]. Recirculation of flow was still observed at position B. Towards the distal end of the ICA, the skewing phenomenon reduced, with the high-velocity region moving towards the geometry center, although the crescent shape still persisted.

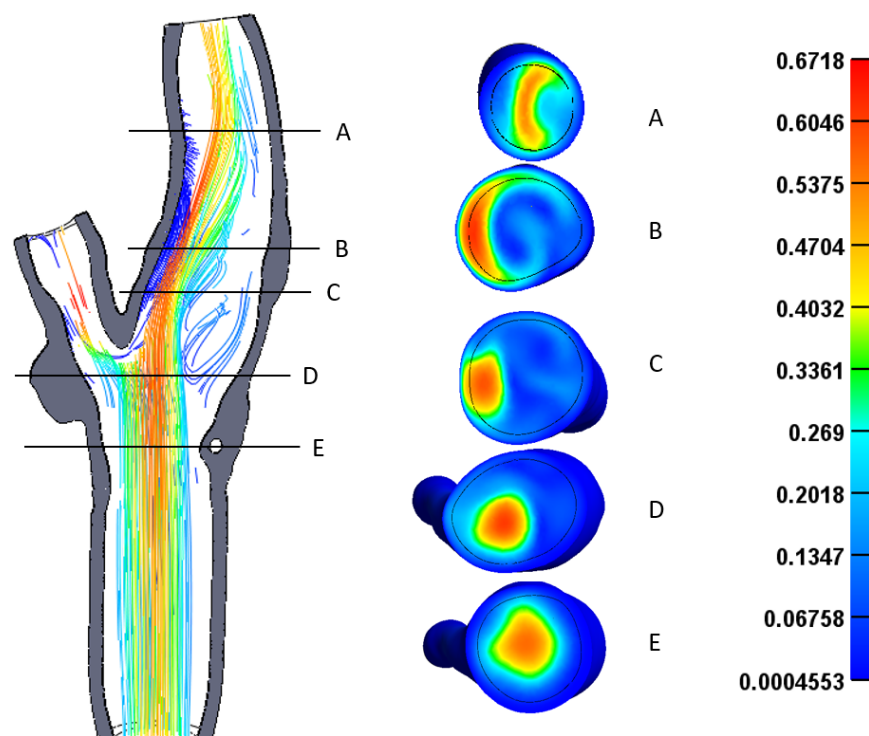


**Figure 3.10: Streamline plot and velocity profiles at different positions in the carotid bifurcation model (m/s).**

Streamline plots were obtained at different time points within a cardiac cycle (Figure 3.11). During early and peak systole (Figure 3.11A and Figure 3.11B), the flow was accelerated and large deformation of the vessel wall was observed. After the peak systolic phase, spiral lines ap-

peared with a severe skewing and recirculation pattern. Following peak diastolic, the presence of secondary flow reduced, and velocity decreased. Throughout the cardiac cycle, skewing was observed throughout the entire cycle. The movement of the high-velocity region towards the inner wall of the bifurcation explained the high time-average shear appearance along the inner wall of the bifurcation.

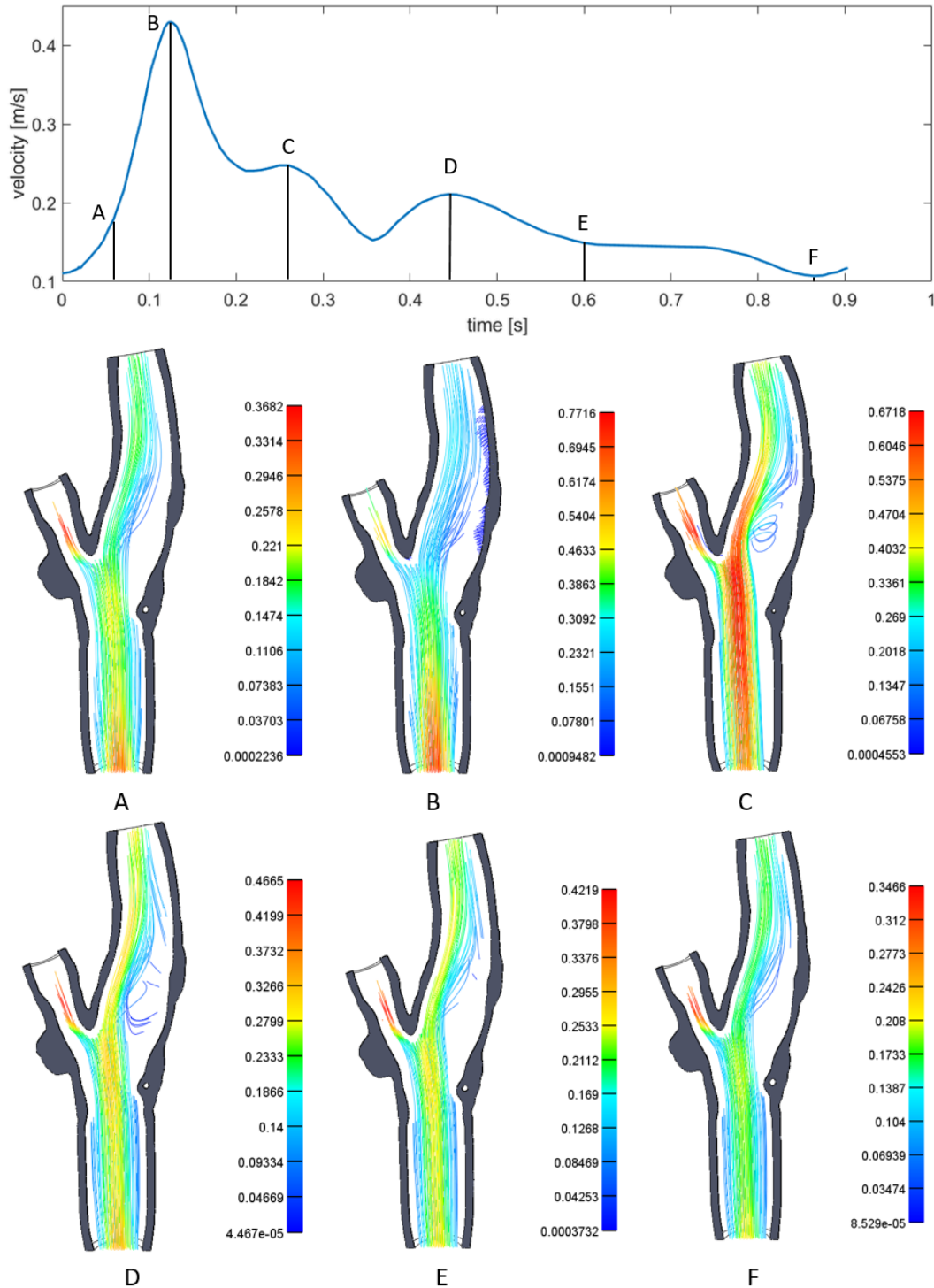
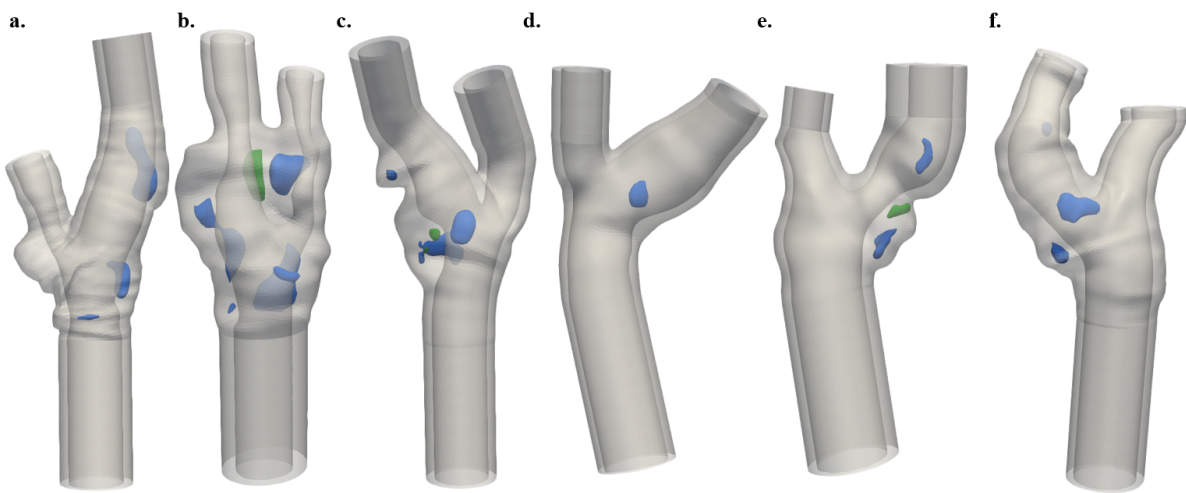


Figure 3.11: Velocity pattern at different time points of a cardiac cycle (m/s).

### 3.4. FSI Result: Six Cases

Three patients with lipid presence on one side and calcium presence on both sides of the carotid artery were chosen for FSI simulation from the PARISK dataset, denoted as Patient 1, 2, and 3, respectively. The final geometry utilized for simulation, as shown in Figure 3.12, was obtained through the method detailed in Section 2.2. The backward incremental method was applied to these vessels, and the resultant deformation gradient served as the predefined deformation field for FSI. Subsequently, FSI was performed using patient-specific velocity profiles and outlet resistances. The results for case 1L were thoroughly illustrated previously and the results of the other five cases were presented in Appendix E. A global analysis of all six cases was presented in this section. The overview of morphological changes and biomechanical stress was shown first. Following this, the stress distribution was analyzed by dividing the sector into three groups using a vessel-specific threshold.



**Figure 3.12: Vessel models with calcium (Blue) and lipid (Green).** From patient 1 a. LEFT, b. RIGHT; patient 2 c. LEFT, d. RIGHT; patient 3 e. LEFT, f. RIGHT.

#### Morphological Metrics

For six vessels across three patients, the morphological metrics at baseline and follow-up were illustrated in Figure 3.13, and the corresponding changes were summarized in Table 3.4. The results on extension and ECA were not shown in 2D map plot as well as used for further analysis. In the analysis of 2808 sectors, calcium was detected in 297 sectors. Only the sectors with calcium detected were used for calcium distance calculation. The percentage change of sector with calcium and diseased WT was calculated per vessel while the change of wall thickness and plaque burden were computed per sector ( $N = 2808$ ).

The percentage of sectors exhibiting diseased thickness increased for all vessel cases (Figure 3.13a), with an average rise of 12.89%. Regarding wall thickness, there was an average increase of 0.17 mm, ranging from a minimum decrease of 1.51 mm to a maximum increase of 2.89 mm. This suggested that thickening and thinning both occurred in the vessel wall from baseline to follow-up, although, for most sectors, the wall thickness increased. Sectors where calcium was detected showed a mean increase of 5.01% in the affected sectors, ranging from

1.45% to 8.81%. Additionally, the average calcium volume increased by  $28.01 \text{ mm}^3$ , with a minimum change of  $3.18 \text{ mm}^3$  and a maximum change of  $46.75 \text{ mm}^3$ . These increments signified plaque progression from baseline to follow-up (Figure 3.13de).

On the other hand, the  $\Delta$ Calcium Distance provided insights into changes in the distance between calcium and the lumen, showing an average decrease of  $0.06 \text{ mm}$ . The range extended from a minimum decrease of  $0.53 \text{ mm}$  to a maximum increase of  $0.36 \text{ mm}$ . Additionally, Figure 3.13f confirmed that the change in the average distance between calcium and the lumen surface was not consistent across vessel cases. Interestingly, vessel 3R showed a decrease in the percentage of disease WT region, average wall thickness, and plaque burden, although the calcium volume and number of calcified sectors increased.

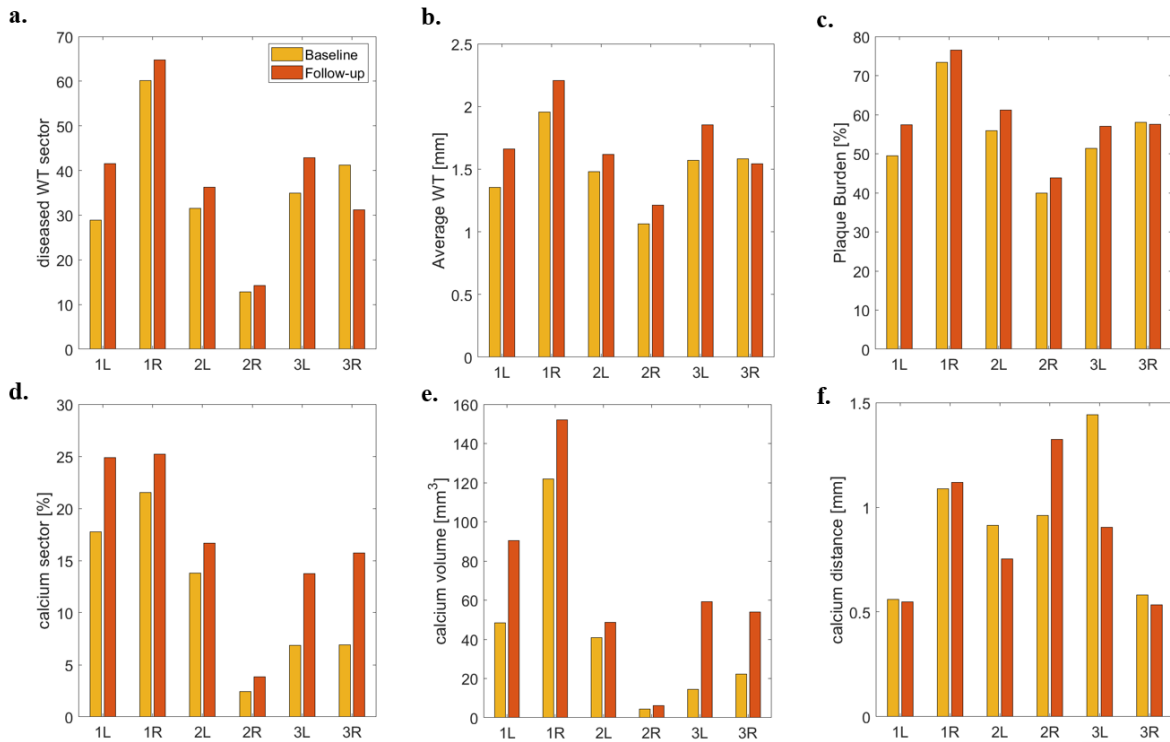


**Figure 3.13: Overview of morphological metrics of six cases at baseline and follow-up.**

**Table 3.4: Overview of Morphological Changes.**

Metrics	Mean	Max	Min
$\Delta$ Diseased WT [%]	5.05	12.31	0
$\Delta$ WT [mm]	0.18	2.92	-1.09
$\Delta$ PB [%]	2.74	33.82	-12.97
$\Delta$ Calcium Sector [%]	5.56	8.15	1.56
$\Delta$ Calcium Volume [ $\text{mm}^3$ ]	28.01	46.75	3.18
$\Delta$ Calcium Distance [mm]	-0.09	0.16	-0.54

### Biomechanical Metrics

In Table 3.5, biomechanical metrics were computed to assess the time-averaged stress distribution across 2808 sectors. The median fluid TAWSS was 1.26 Pa, indicating a pro-atherosclerotic condition in most of the sectors. The solid wall shear stress, which represented the mechanical interaction between blood and vessel walls, revealed a median value of 14.99 kPa. The von Mises stress was calculated both at the lumen interface and as an average across the vascular structure. The von Mises stress at the interface exhibited a larger range compared to the average value, with a larger median of 161 kPa.

**Table 3.5:** Overview of Time-Averaged Biomechanical Metrics of Sectors (N = 2808).

	<b>Median</b>	<b>Max</b>	<b>Min</b>
<b>Fluid TAWSS [Pa]</b>	1.26	14.92	0.14
<b>Solid TAWSS [kPa]</b>	14.99	87.17	2.39
<b>TAVMS Interface [kPa]</b>	26.55	161.00	4.36
<b>TAVMS Average [kPa]</b>	23.64	133.45	6.87

### Stress Distribution

In the examination of 2808 sectors, 297 sectors were found to contain calcium. This section presented the stress distribution and morphological changes of these sectors. Stress thresholds—low, mid, and high—were established by dividing the stress levels of all sectors into three groups, with each group representing one-third of all sectors. Following this, the morphological changes of the sectors were calculated. The calculation of calcium distance considered only the sectors where calcium was detected.

Table 3.6 presented the threshold of this study for different stress. For fluid TAWSS, the low/mid threshold was 0.88 Pa, while the mid/high threshold was at 2.08 Pa. In the context of solid TAWSS, the threshold between low and mid stress is at 11.13 kPa, while high stress was defined above 24.64 kPa. The TAVMS at the interface and average over the vessel showed a similar threshold for both low/mid and mid/high. Furthermore, Figure 3.14 provided an overview of the stress distribution across six vessels. Sectors with mid and high solid TAWSS stress were identified in vessels 2R and 3L, while vessels 1L, 1R, and 3R exhibited only low and mid solid TAWSS stress sectors. This pattern was consistent for both TAVMS metrics of average and interface, highlighting large variations in solid stress among different vessels.

**Table 3.6:** Threshold for Stress Distribution

	<b>Low/Mid Threshold</b>	<b>Mid/High Threshold</b>
<b>Fluid TAWSS [Pa]</b>	0.88	2.08
<b>Solid TAWSS [kPa]</b>	11.13	24.64
<b>TAVMS Average [kPa]</b>	18.11	39.74
<b>TAVMS Interface [kPa]</b>	19.69	43.81

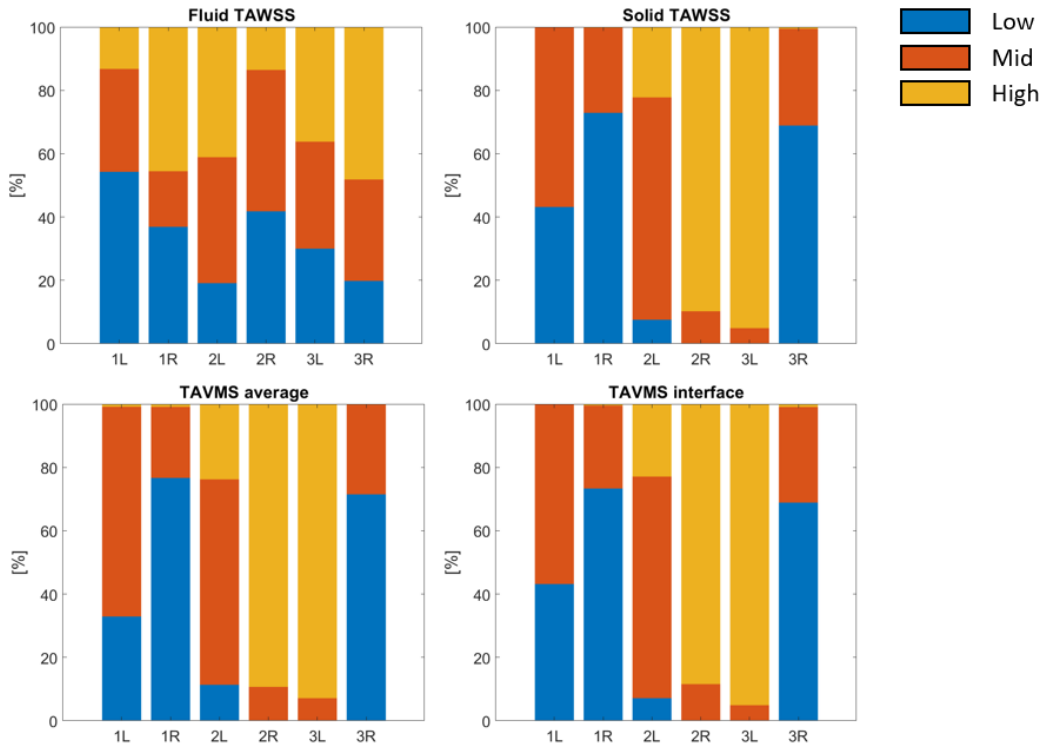


**Figure 3.14:** Overview of six vessels showing the stress distribution for each vessel.

For fluid TAWSS, a reduction (0.27 mm) in calcium distance was observed in mid-stress sectors (Figure 3.15a). Conversely, sectors with low fluid TAWSS exhibited no significant changes in calcium distance. However, low fluid TAWSS sectors demonstrated a substantial increase (3.86%) in plaque burden (Figure 3.15b), while the difference in plaque burden change between mid and high stress sectors was relatively small (2.61% and 2.83%, respectively). Interestingly, the increase in wall thickness was significantly higher in sectors exposed to both low and high fluid TAWSS (0.20 mm and 0.22 mm) compared to mid-stress sectors (0.13 mm).

In the case of Solid TAWSS, the calcium distance displayed significant variability across stress distribution, as depicted in Figure 3.15d. Notably, there was a substantial decrease (0.29 mm) in high-stress sectors and a minor decrease (0.19 mm) in mid-stress sectors. The increase in plaque burden over time was related to increased stress levels, suggesting that sectors exposed to high solid TAWSS exhibited greater plaque development from baseline to follow-up compared to other sectors. Additionally, the trend of  $\Delta$ thickness aligned with patterns observed in fluid TAWSS (Figure 3.15c and f).

For time-average von Mises stress, similar patterns were found in plaque burden, and thickness changes for the two methods, as illustrated in Figure 3.15d-i. Notably, when computing the average value across the vessel, the variance in wall thickness change between stress groups was less pronounced compared to values obtained from the lumen interface. Concerning the change in  $\Delta$ calcium distance, the most significant decrease was observed in the high-stress group of average TAVMS, while the most substantial decrease occurred in the mid-stress group of TAVMS on the interface.

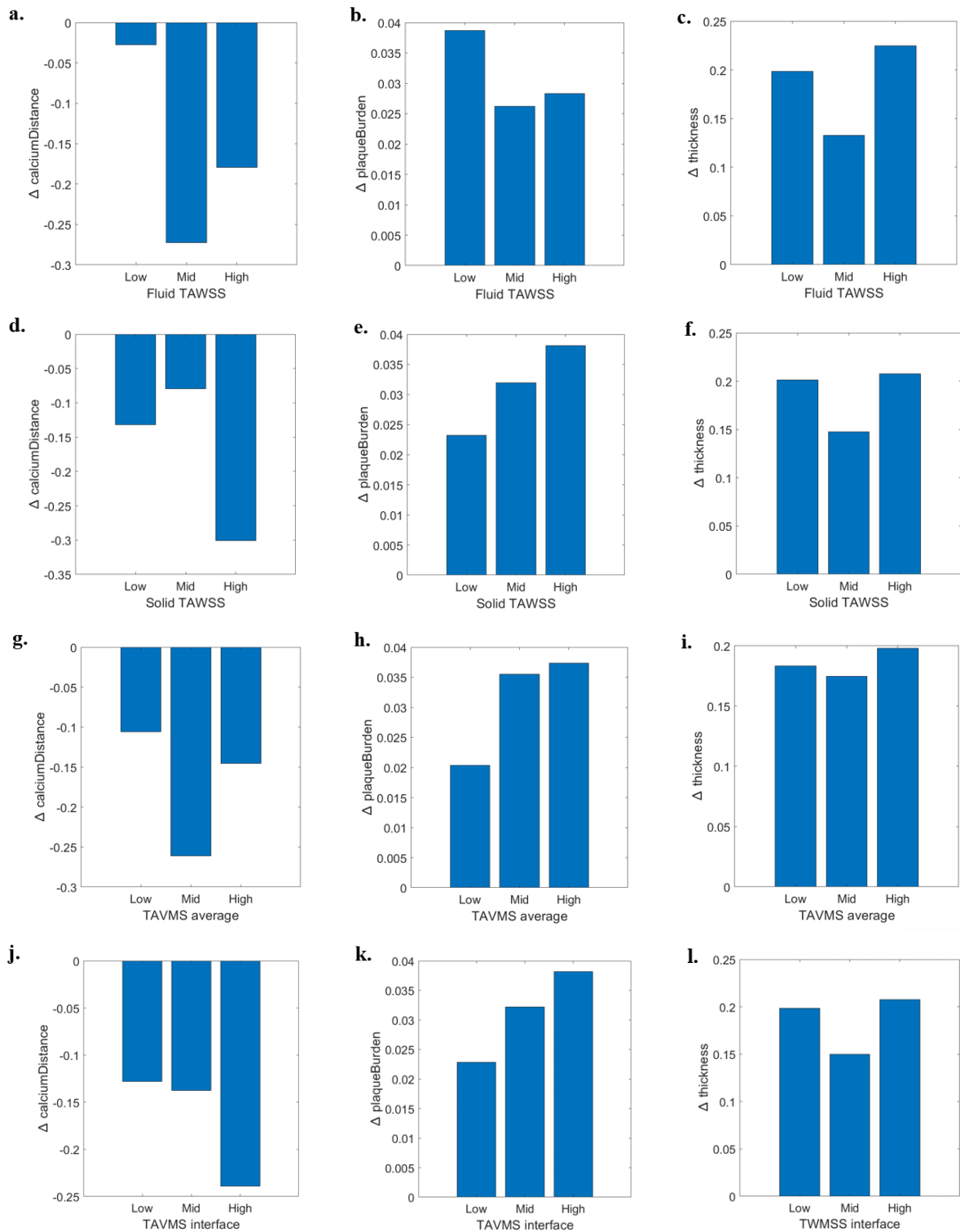


**Figure 3.15: Stress Distribution and morphological changes over time.** a-c. Fluid time-average wall shear stress (TAWSS) d-f. Solid time-average wall shear stress (TAWSS) g-i. Average time-average von Mises stress (TAVMS) j-l. Time-average von Mises stress (TAVMS) at interface

# 4

## Discussion

### 4.1. Framework

This thesis introduced a new methodology that enabled the computational FSI analysis of atherosclerotic carotid walls from CTA images. The advantage brought by this method was that the generated models closely resembled realistic and patient-specific representations of atherosclerotic carotid arteries, including vessel and plaque geometries, initial stress, and boundary conditions. The entire process can be automatically executed using Matlab, making it particularly useful for large database analysis.

Geometric reconstructions of the carotid bifurcation primarily influenced the numerical simulation result [35][70][71]. The vessel wall geometry and two plaque components utilized in this study were obtained through CTA image segmentation. The reconstruction of 3D vessel geometry from 2D images involved two widely used methods: the iso-surface method and the loft method [72][73][74]. The iso-surface reconstruction employed a series of parallel contours generated using the Marching Cubes algorithm [75]. Nevertheless, the selection of the threshold grey scale level posed challenges due to image inhomogeneities and other artifacts [76]. Moreover, since the contour coordinates derived from CTA image segmentation were originally aligned along the centerline, the conversion of these contours into parallel sets required by the iso-surface method could introduce errors, depending on the chosen projection level density. An alternative approach involved lofting multiple 2D slices to create 3D geometry, a technique applied in other pipelines for vessel geometry reconstruction [72]. However, this method encountered difficulties in cases where side branches or multiple sets of contours were present. In this study, a novel reconstruction method was introduced, using the alpha-shape algorithm [45]. The contour coordinate sets were treated as a 3D point cloud, and the vessel structure was defined as the resulting bounding surface of this point cloud. This approach showed its strength in accurately identifying concave structures, including side branches and vessels with bends.

In this project, the consideration of initial stress was a crucial aspect, addressed through the backward incremental method. Due to the limitations of medical imaging methods, obtaining the unloaded vessel geometry in a living subject was impractical. The deformed geometry brought errors in the computational accuracy of stress analysis. Tang et al. [73] employed

axial and circumferential shrinkage of the carotid artery to approximate the unloaded geometry before FSI. The shrinkage rate was determined by aligning the loaded plaque geometry, achieved after a 10% axial stretch and pressurization, with the *in vivo* geometry. While the Backward Incremental method had been employed previously to address initial stress effects on stress distribution in arterial walls in both 2D [77][49] and 3D models [78], its implementation in FSI and FEBio was lacking. This project proposed an approach that introduced the use of the backward incremental method in FEBio through a prestrain method [50]. This advancement not only enhanced the accuracy of stress distribution results in FSI in this project but also contributed to more realistic stress results for future computational analyses of vessels within the FEBio framework.

Measured patient-specific flow profiles were not used in this project, however, a parabolic profile, inlet extension, and a time-varying velocity waveform estimated by the vessel diameter were employed as the inlet boundary condition. The assumption of a relatively consistent flow waveform shape across normal subjects was adopted [30][79]. In the context of carotid bifurcation studies, four common inlet velocity profile assumptions—flat, parabolic, blunt, and Womersley—have been widely employed [71]. Campbell et al.'s [71] evaluation of these assumptions in a human carotid bifurcation model found that the parabolic profile yielded the lowest error in wall shear stress when compared to the real flow profile. Additionally, although physiologically relevant parameters, including WSS, were sensitivity to inlet velocity profiles [30], it was found to be affected mostly by the patient-specific geometry rather than the flow in numerical simulations of blood flow [61][70][71]. Moyle et al. [70] conducted a study investigating the effects of secondary velocities in the inlet profile on WSS in the carotid bifurcation. Their findings suggested that, given a sufficient entrance length of realistic geometry, simplifying the inlet flow to a fully developed axial profile may be done without penalty. Therefore, this selection of inlet velocity profiles enhanced the reliability of the FSI analysis conducted in this study.

## 4.2. Result

FSI simulation was performed on six vessel cases using the proposed pipeline. Four biomechanical metrics were computed to examine hemodynamic forces on the carotid artery. The range and pattern of these stresses obtained from the FSI results aligned with those from previous studies, indicating the robustness of the pipeline.

In this study, peak values of TAWSS were found on the inner walls of the ICA near the bifurcation points, with moderately elevated values along the ICA in the superior direction. Lower TAWSS values were primarily observed along the outer walls of the sinus bulbs or the plaque region (Figure 3.6). The distribution was in line with findings previously described in the literature [26][80][81][82]. The TAWSS range in this study, spanning from 0.14 Pa to 14.92 Pa (Table 3.5), aligned with findings reported by Dilba et al. [83], who also utilized the PARISK database and conducted CFD simulations. However, large variations in WSS values were encountered between patients, due to the large influence of geometrical factors on WSS patterns [70][84].

Regarding von Mises stress, despite variations in stress magnitudes over time, consistent spatial distributions of stress patterns were identified throughout the cardiac cycle. The structural

stress within the vessel wall exhibited a complex pattern due to the irregular 3D geometry and variable wall thickness at the bifurcation [81]. The overall time-averaged von Mises stress ranged from 4.36 kPa to 161.00 kPa at the lumen surface, with an average value ranging between 6.87 kPa and 133.45 kPa (Table 3.5). These stress measures were similar to the range reported by Gao et al. [85], who observed a maximum wall stress of 140.3-198.5 kPa. Notably, stress concentration was identified at the bifurcation point and areas with sharp edges of calcium deposits. Other studies [86][87] also observed this phenomenon. This concentration phenomenon implied potential artery injury and made the branch region susceptible to atherosclerosis.

Morphological changes, including wall thickness, plaque burden, and calcium distance, were used to evaluate the atherosclerotic carotid geometry over time. Following this, the stress distribution and morphological changes were discussed.

Wall thickness exhibited a general increase across all patients, with heightened values observed in sectors identified as diseased WT areas, signifying the progressive nature of atherosclerosis. Instances of increased diseased WT often coincided with lower stress levels, echoing findings from previous studies that have explored the negative association between WSS and wall thickening [88][89].

Plaque burden served as an additional metric to illustrate disease development in this study. In the context of fluid TAWSS, sectors with low-stress levels exhibited the highest increase in plaque burden, while for solid stresses, regions subjected to high stress displayed a significant rise in plaque burden. These observations align with findings in previous studies that investigated the impact of plaque structural stress and wall shear stress on coronary plaque burden, highlighting the relevance of stresses with plaque progression [90][91].

The third morphological metric explored in this study was the distance between calcium deposits and the lumen. The positioning of these deposits emerged as a crucial influencing factor [87][92][93]. Notably, calcium located near the surface impacted plaque stability by elevating shoulder stress and inducing stress concentrations in the cap [87]. Consequently, the investigation in this project focused on assessing the distance between calcium deposits and the lumen across six vessels. A large decrease in calcium distance was observed in high-stress sectors of solid TAWSS and TAVMS on the lumen surface. However, for fluid TAWSS and average TAVMS, the most significant decrease occurred in mid-stress sectors.

### 4.3. Limitations

This study had several limitations, including constraints related to sample size, choice of material model, and validation of simulation results. Firstly, the sample size was restricted to six vessels from three patients, which may affect the generalizability of the findings. Future investigations with larger sample sizes made it possible to conduct statistical analysis and thus lead to more robust and reliable conclusions.

In this project, both the vessel and plaque components were modeled as homogeneous using isotropic material models. However, considering the anisotropic and non-homogeneous nature of the vessel due to the fiber orientation, modeling each layer differently could yield distinct results. This aspect, if addressed, may contribute to a more accurate representation of the

complex arterial structure.

Moreover, the study lacked a validation process with a comparison between numerical results and in vivo measurements, such as four-dimensional cardiovascular magnetic resonance flow imaging (4D Flow CMR). The numerical simulation process involved a set of simplifications and assumptions, thereby, uncertainty and errors were inherent to the results. Incorporating such validation measures would provide an evaluation of the model's accuracy and predictive capabilities.

# 5

## Conclusion

This project aimed to establish a comprehensive pipeline for investigating plaque progression in carotid arteries, with a focus on biomechanical parameters utilizing patient-specific FSI models. The 3D vessel geometry and two plaque components were derived from CTA image data using the Alphashape method. To address the issue of initial stress, the backward incremental method was implemented. Subsequently, FSI simulations were performed on six vessels from the PARISK dataset using FEBio. The patient-specific inlet and outlet boundary conditions were obtained based on the vessel geometry and blood pressure. Morphological changes, including plaque burden, wall thickness, and calcium distance, were quantified to study plaque progression over time. The numerical simulation results provided insights into biomechanical stresses, including fluid and solid wall shear stress and von Mises stress. The stress distribution, morphological changes, and flow patterns were studied. The findings not only showed the robustness of this framework but also provided valuable insights into the relationship between biomechanics and plaque progression in carotid arteries.

# 6

## References

- [1] E. Britannica. “Britannica, t. editors of encyclopaedia.” (2023), [Online]. Available: <https://www.britannica.com/science/atherosclerosis> (visited on 08/24/2023).
- [2] H. Wang, M. Naghavi, C. Allen, *et al.*, “Global, regional, and national life expectancy, all-cause mortality, and cause-specific mortality for 249 causes of death, 1980–2015: A systematic analysis for the global burden of disease study 2015,” *The lancet*, vol. 388, no. 10053, pp. 1459–1544, 2016.
- [3] E. Falk, P. K. Shah, and V. Fuster, “Coronary plaque disruption,” *Circulation*, vol. 92, no. 3, pp. 657–671, 1995.
- [4] J. F. Bentzon, F. Otsuka, R. Virmani, and E. Falk, “Mechanisms of plaque formation and rupture,” *Circulation research*, vol. 114, no. 12, pp. 1852–1866, 2014.
- [5] “Endothelial primary cilia in areas of disturbed flow are at the base of atherosclerosis,” *Atherosclerosis*, vol. 196, no. 2, pp. 542–550, 2008, ISSN: 0021-9150. DOI: <https://doi.org/10.1016/j.atherosclerosis.2007.05.030>.
- [6] B. R. Kwak, M. Bäck, M.-L. Bochaton-Piallat, *et al.*, “Biomechanical factors in atherosclerosis: Mechanisms and clinical implications,” *European heart journal*, vol. 35, no. 43, pp. 3013–3020, 2014.
- [7] P. Libby, “Atherosclerosis: The new view,” *Scientific American*, vol. 286, no. 5, pp. 46–55, 2002, ISSN: 00368733, 19467087. [Online]. Available: <http://www.jstor.org/stable/26059682> (visited on 04/01/2023).
- [8] “Carotid artery stenting simulation: From patient-specific images to finite element analysis,” *Medical Engineering Physics*, vol. 33, no. 3, pp. 281–289, 2011, ISSN: 1350-4533. DOI: <https://doi.org/10.1016/j.medengphy.2010.10.011>. [Online]. Available: <https://www.sciencedirect.com/science/article/pii/S1350453310002420>.
- [9] J. M. Wardlaw, M. D. Stevenson, F. Chappell, *et al.*, “Carotid artery imaging for secondary stroke prevention,” *Stroke*, vol. 40, no. 11, pp. 3511–3517, 2009. DOI: 10.1161/STROKEAHA.109.557017. [Online]. Available: <https://www.ahajournals.org/doi/abs/10.1161/STROKEAHA.109.557017>.
- [10] T. T. de Weert, M. Ouhlous, E. Meijering, *et al.*, “In vivo characterization and quantification of atherosclerotic carotid plaque components with multidetector computed tomography and histopathological correlation,” *Arteriosclerosis, Thrombosis, and Vascular*

- Biology*, vol. 26, no. 10, pp. 2366–2372, 2006. DOI: 10.1161/01.ATV.0000240518.90124.57. [Online]. Available: <https://www.ahajournals.org/doi/abs/10.1161/01.ATV.0000240518.90124.57>.
- [11] H. Baradaran and A. Gupta, “Carotid vessel wall imaging on cta,” *AJNR. American journal of neuroradiology*, vol. 41, no. 3, pp. 380–386, Mar. 2020, Epub 2020 Feb 6. DOI: 10.3174/ajnr.A6403. [Online]. Available: <https://doi.org/10.3174/ajnr.A6403>.
- [12] M. Wintermark, S. S. Jawadi, J. H. Rapp, *et al.*, “High-resolution ct imaging of carotid artery atherosclerotic plaques,” *AJNR. American journal of neuroradiology*, vol. 29, no. 5, pp. 875–882, May 2008, Epub 2008 Feb 13. DOI: 10.3174/ajnr.A0950.
- [13] D. H. van Dam-Nolen, M. T. Truijman, A. G. van der Kolk, *et al.*, “Carotid plaque characteristics predict recurrent ischemic stroke and tia: The parisk (plaque at risk) study,” *JACC: Cardiovascular Imaging*, vol. 15, no. 10, pp. 1715–1726, 2022, ISSN: 1936-878X. DOI: <https://doi.org/10.1016/j.jcmg.2022.04.003>. [Online]. Available: <https://www.sciencedirect.com/science/article/pii/S1936878X22002352>.
- [14] P. A. VanderLaan, C. A. Reardon, and G. S. Getz, “Site specificity of atherosclerosis: Site-selective responses to atherosclerotic modulators,” *Arteriosclerosis, thrombosis, and vascular biology*, vol. 24, no. 1, pp. 12–22, 2004.
- [15] M. A. Anwar, J. Shalhoub, C. S. Lim, M. S. Gohel, and A. H. Davies, “The effect of pressure-induced mechanical stretch on vascular wall differential gene expression,” *Journal of Vascular Research*, vol. 49, no. 6, pp. 463–478, 2012, ISSN: 1018-1172. DOI: 10.1159/000339151.
- [16] E. Cecchi, C. Giglioli, S. Valente, *et al.*, “Role of hemodynamic shear stress in cardiovascular disease,” *Atherosclerosis*, vol. 214, no. 2, pp. 249–256, 2011, ISSN: 0021-9150. DOI: <https://doi.org/10.1016/j.atherosclerosis.2010.09.008>. [Online]. Available: <https://www.sciencedirect.com/science/article/pii/S0021915010007367>.
- [17] H. C. Groen, F. J. Gijsen, A. Van Der Lugt, *et al.*, “Plaque rupture in the carotid artery is localized at the high shear stress region: A case report,” *Stroke*, vol. 38, no. 8, pp. 2379–2381, 2007.
- [18] A. Bank, A. Versluis, S. Dodge, and W. Douglas, “Atherosclerotic plaque rupture: A fatigue process?” *Medical hypotheses*, vol. 55, no. 6, pp. 480–484, 2000.
- [19] D. Camasão and D. Mantovani, “The mechanical characterization of blood vessels and their substitutes in the continuous quest for physiological-relevant performances. a critical review,” *Materials Today Bio*, vol. 10, p. 100 106, 2021.
- [20] Y. S. Chatzizisis, A. U. Coskun, M. Jonas, E. R. Edelman, C. L. Feldman, and P. H. Stone, “Role of endothelial shear stress in the natural history of coronary atherosclerosis and vascular remodeling: Molecular, cellular, and vascular behavior,” *Journal of the American College of Cardiology*, vol. 49, no. 25, pp. 2379–2393, 2007.
- [21] K. S. Cunningham and A. I. Gotlieb, “The role of shear stress in the pathogenesis of atherosclerosis,” *Laboratory investigation*, vol. 85, no. 1, pp. 9–23, 2005.
- [22] J. J. Wentzel, Y. S. Chatzizisis, F. J. Gijsen, G. D. Giannoglou, C. L. Feldman, and P. H. Stone, “Endothelial shear stress in the evolution of coronary atherosclerotic plaque and vascular remodelling: Current understanding and remaining questions,” *Cardiovascular research*, vol. 96, no. 2, pp. 234–243, 2012.

- 
- [23] K. McGurk, B. Owen, W. Watson, *et al.*, “Heritability of haemodynamics in the ascending aorta,” *Scientific Reports*, vol. 2020, p. 14 356, Sep. 2020. DOI: 10.1038/s41598-020-71354-7.
- [24] Ö. Zümre, A. Salbacak, A. E. Çiçekcibaşı, I. Tuncer, and M. Seker, “Investigation of the bifurcation level of the common carotid artery and variations of the branches of the external carotid artery in human fetuses,” *Annals of Anatomy - Anatomischer Anzeiger*, vol. 187, no. 4, pp. 361–369, 2005, ISSN: 0940-9602. DOI: <https://doi.org/10.1016/j.aanat.2005.03.007>. [Online]. Available: <https://www.sciencedirect.com/science/article/pii/S0940960205000646>.
- [25] P. Jiang, Z. Chen, D. S. Hippe, *et al.*, “Association between carotid bifurcation geometry and atherosclerotic plaque vulnerability: A chinese atherosclerosis risk evaluation study,” *Arteriosclerosis, thrombosis, and vascular biology*, vol. 40, no. 5, pp. 1383–1391, 2020.
- [26] M. Markl, F. Wegent, T. Zech, *et al.*, “In vivo wall shear stress distribution in the carotid artery: Effect of bifurcation geometry, internal carotid artery stenosis, and recanalization therapy,” *Circulation: Cardiovascular Imaging*, vol. 3, no. 6, pp. 647–655, 2010.
- [27] C. K. Zarins, D. P. Giddens, B. Bharadvaj, V. S. Sottiurai, R. F. Mabon, and S. Glagov, “Carotid bifurcation atherosclerosis. quantitative correlation of plaque localization with flow velocity profiles and wall shear stress,” *Circulation research*, vol. 53, no. 4, pp. 502–514, 1983.
- [28] D. Lopes, H. Puga, J. C. Teixeira, and S. Teixeira, “Influence of arterial mechanical properties on carotid blood flow: Comparison of cfd and fsi studies,” *International Journal of Mechanical Sciences*, vol. 160, pp. 209–218, 2019.
- [29] M. Albadawi, Y. Abuouf, S. Elsagheer, H. Sekiguchi, S. Ookawara, and M. Ahmed, “Influence of rigid-elastic artery wall of carotid and coronary stenosis on hemodynamics,” *Bioengineering*, vol. 9, no. 11, p. 708, Nov. 2022. DOI: 10.3390/bioengineering9110708.
- [30] S. H. Lee, S. Kang, N. Hur, and S.-K. Jeong, “A fluid-structure interaction analysis on hemodynamics in carotid artery based on patient-specific clinical data,” *Journal of mechanical science and technology*, vol. 26, pp. 3821–3831, 2012.
- [31] G. Hou, J. Wang, and A. Layton, “Numerical methods for fluid-structure interaction—a review,” *Communications in Computational Physics*, vol. 12, no. 2, pp. 337–377, 2012.
- [32] D. Lopes, H. Puga, J. Teixeira, and R. Lima, “Blood flow simulations in patient-specific geometries of the carotid artery: A systematic review,” *Journal of Biomechanics*, vol. 111, p. 110 019, 2020, ISSN: 0021-9290. DOI: <https://doi.org/10.1016/j.jbiomech.2020.110019>. [Online]. Available: <https://www.sciencedirect.com/science/article/pii/S0021929020304425>.
- [33] L. C. Sousa, C. F. Castro, C. C. António, *et al.*, “Computational simulation of carotid stenosis and flow dynamics based on patient ultrasound data - a new tool for risk assessment and surgical planning,” *Advances in Medical Sciences*, vol. 61, no. 1, pp. 32–39, 2016. DOI: 10.1016/j.advms.2015.07.009.
- [34] M. Malvè, S. Chandra, A. García, *et al.*, “Impedance-based outflow boundary conditions for human carotid haemodynamics,” *Computer methods in biomechanics and biomedical engineering*, vol. 17, no. 11, pp. 1248–1260, 2014.

- 
- [35] S. Zhao, X. Xu, A. Hughes, *et al.*, “Blood flow and vessel mechanics in a physiologically realistic model of a human carotid arterial bifurcation,” *Journal of biomechanics*, vol. 33, no. 8, pp. 975–984, 2000.
- [36] D. Lopes, H. Puga, J. Teixeira, and S. Teixeira, “Influence of arterial mechanical properties on carotid blood flow: Comparison of cfd and fsi studies,” *International Journal of Mechanical Sciences*, vol. 160, pp. 209–218, 2019, ISSN: 0020-7403. DOI: <https://doi.org/10.1016/j.ijmecsci.2019.06.029>. [Online]. Available: <https://www.sciencedirect.com/science/article/pii/S0020740319302899>.
- [37] A. V. Kamenskiy, I. I. Pipinos, Y. A. Dzenis, P. K. Gupta, S. A. Jaffar Kazmi, and J. N. MacTaggart, “A mathematical evaluation of hemodynamic parameters after carotid eversion and conventional patch angioplasty,” *American Journal of Physiology-Heart and Circulatory Physiology*, vol. 305, no. 5, H716–H724, 2013, PMID: 23812386. DOI: 10.1152/ajpheart.00034.2013. eprint: <https://doi.org/10.1152/ajpheart.00034.2013>. [Online]. Available: <https://doi.org/10.1152/ajpheart.00034.2013>.
- [38] A. V. Kamenskiy, I. I. Pipinos, Y. A. Dzenis, *et al.*, “Effects of carotid artery stenting on arterial geometry,” *Journal of the American College of Surgeons*, vol. 217, no. 2, pp. 251–262, 2013, ISSN: 1072-7515. DOI: <https://doi.org/10.1016/j.jamcollsurg.2013.03.016>. [Online]. Available: <https://www.sciencedirect.com/science/article/pii/S1072751513002408>.
- [39] “The influence of constitutive law choice used to characterise atherosclerotic tissue material properties on computing stress values in human carotid plaques,” *Journal of Biomechanics*, vol. 48, no. 14, pp. 3912–3921, 2015, ISSN: 0021-9290. DOI: <https://doi.org/10.1016/j.jbiomech.2015.09.023>. [Online]. Available: <https://www.sciencedirect.com/science/article/pii/S0021929015005175>.
- [40] D. Tang, Z. Teng, G. Canton, *et al.*, “Sites of rupture in human atherosclerotic carotid plaques are associated with high structural stresses,” *Stroke*, vol. 40, no. 10, pp. 3258–3263, 2009. DOI: 10.1161/STROKEAHA.109.558676. eprint: <https://www.ahajournals.org/doi/pdf/10.1161/STROKEAHA.109.558676>. [Online]. Available: <https://www.ahajournals.org/doi/abs/10.1161/STROKEAHA.109.558676>.
- [41] M. T. Truijman, M. E. Kooi, A. C. van Dijk, and *et al.*, “Plaque at risk (parisk): Prospective multicenter study to improve diagnosis of high-risk carotid plaques,” *International Journal of Stroke*, vol. 9, no. 6, pp. 747–754, 2014. DOI: 10.1111/ijvs.12167.
- [42] D. H. van Dam-Nolen, A. C. van Dijk, G. A. Crombag, *et al.*, “Lipoprotein(a) levels and atherosclerotic plaque characteristics in the carotid artery: The plaque at risk (parisk) study,” *Atherosclerosis*, vol. 329, pp. 22–29, 2021, ISSN: 0021-9150. DOI: <https://doi.org/10.1016/j.atherosclerosis.2021.06.004>. [Online]. Available: <https://www.sciencedirect.com/science/article/pii/S0021915021002756>.
- [43] Y. A. Elnabawi, A. K. Dey, A. Goyal, *et al.*, “Coronary artery plaque characteristics and treatment with biologic therapy in severe psoriasis: Results from a prospective observational study,” *Cardiovascular research*, vol. 115, no. 4, pp. 721–728, 2019.
- [44] F. Bernardini and C. L. Bajaj, “Sampling and reconstructing manifolds using alpha-shapes,” 1997.
- [45] H. Edelsbrunner and E. P. Mücke, “Three-dimensional alpha shapes,” *ACM Transactions On Graphics (TOG)*, vol. 13, no. 1, pp. 43–72, 1994.

- 
- [46] K. Moerman, “Gibbon: The geometry and image-based bioengineering add-on,” *The Journal of Open Source Software*, vol. 3, p. 506, Feb. 2018. DOI: 10.21105/joss.00506.
- [47] M. Attene, “A lightweight approach to repairing digitized polygon meshes,” *The visual computer*, vol. 26, pp. 1393–1406, 2010.
- [48] E. Trudel. “Surface booleans.” (2023), [Online]. Available: <https://www.mathworks.com/matlabcentral/fileexchange/122502-surface-booleans> (visited on 08/24/2023).
- [49] L. Speelman, A. Akyildiz, B. Den Adel, *et al.*, “Initial stress in biomechanical models of atherosclerotic plaques,” *Journal of biomechanics*, vol. 44, no. 13, pp. 2376–2382, 2011.
- [50] S. A. Maas, A. Erdemir, J. P. Halloran, and J. A. Weiss, “A general framework for application of prestrain to computational models of biological materials,” *Journal of the Mechanical Behavior of Biomedical Materials*, vol. 61, pp. 499–510, 2016, ISSN: 1751-6161. DOI: <https://doi.org/10.1016/j.jmbbm.2016.04.012>. [Online]. Available: <https://www.sciencedirect.com/science/article/pii/S1751616116300765>.
- [51] J. Wang, P. K. Paritala, J. B. Mendieta, *et al.*, “Optical coherence tomography-based patient-specific coronary artery reconstruction and fluid–structure interaction simulation,” *Biomechanics and modeling in mechanobiology*, vol. 19, no. 1, pp. 7–20, 2020.
- [52] P. K. Paritala, P. K. Yarlagadda, J. Wang, Y. Gu, and Z. Li, “Numerical investigation of atherosclerotic plaque rupture using optical coherence tomography imaging and xfem,” *Engineering Fracture Mechanics*, vol. 204, pp. 531–541, 2018.
- [53] S. G. Torun, H. M. Torun, H. H. Hansen, *et al.*, “Multicomponent material property characterization of atherosclerotic human carotid arteries through a bayesian optimization based inverse finite element approach,” *journal of the mechanical behavior of biomedical materials*, vol. 126, p. 104996, 2022.
- [54] F. M. White, *Fluid mechanics*. New York, 1990.
- [55] C. W. Kerber and C. B. Heilman, “Flow dynamics in the human carotid artery: I. preliminary observations using a transparent elastic model.,” *American journal of neuro-radiology*, vol. 13, no. 1, pp. 173–180, 1992.
- [56] G.-T. Liu, X.-J. Wang, B.-Q. Ai, and L.-G. Liu, “Numerical study of pulsating flow through a tapered artery with stenosis,” *Chinese Journal of Physics*, vol. 42, no. 4, pp. 401–409, 2004.
- [57] M. Y. Abdollahzadeh Jamalabadi, M. Daqiqshirazi, H. Nasiri, M. R. Safaei, and T. K. Nguyen, “Modeling and analysis of biomagnetic blood carreau fluid flow through a stenosis artery with magnetic heat transfer: A transient study,” *PLoS One*, vol. 13, no. 2, e0192138, 2018.
- [58] R. Ellahi, S. Rahman, M. M. Gulzar, S. Nadeem, and K. Vafai, “A mathematical study of non-newtonian micropolar fluid in arterial blood flow through composite stenosis,” *Applied Mathematics & Information Sciences*, vol. 8, no. 4, p. 1567, 2014.
- [59] Y. Cho and K. Kensey, “Effects of the non-newtonian viscosity of blood on flows in a diseased arterial vessel. part 1: Steady flows,” *Biorheology*, vol. 28, pp. 241–62, Feb. 1991. DOI: 10.3233/BIR-1991-283-415.

- 
- [60] S.-W. Lee, L. Antiga, J. D. Spence, and D. A. Steinman, "Geometry of the carotid bifurcation predicts its exposure to disturbed flow," *Stroke*, vol. 39, no. 8, pp. 2341–2347, 2008.
- [61] H. C. Groen, L. Simons, Q. J. van den Bouwhuisen, *et al.*, "Mri-based quantification of outflow boundary conditions for computational fluid dynamics of stenosed human carotid arteries," *Journal of biomechanics*, vol. 43, no. 12, pp. 2332–2338, 2010.
- [62] S. H. Lee, S. Kang, and N. Hur, "An approach on fluid-structure interaction for hemodynamics of carotid arteries," in *Fluids Engineering Division Summer Meeting*, American Society of Mechanical Engineers, vol. 44762, 2012, pp. 253–257.
- [63] I. E. Vignon-Clementel, C. A. Figueroa, K. E. Jansen, and C. A. Taylor, "Outflow boundary conditions for three-dimensional finite element modeling of blood flow and pressure in arteries," *Computer methods in applied mechanics and engineering*, vol. 195, no. 29–32, pp. 3776–3796, 2006.
- [64] J. J. Shim, S. A. Maas, J. A. Weiss, and G. A. Ateshian, "A formulation for fluid-structure interactions in febio using mixture theory," *Journal of Biomechanical Engineering*, vol. 141, no. 5, p. 051 010, 2019.
- [65] E. M. J. Hartman, G. De Nisco, A. M. Kok, *et al.*, "Lipid-rich plaques detected by near-infrared spectroscopy are more frequently exposed to high shear stress," *J Cardiovasc Transl Res*, vol. 14, no. 3, pp. 416–425, Jun. 2021, Epub 2020 Oct 9. DOI: 10.1007/s12265-020-10072-x.
- [66] MathWorks. "Matlab pchip function documentation." (Year of access), [Online]. Available: <https://nl.mathworks.com/help/matlab/ref/pchip.html>.
- [67] P.-J. Touboul, M. Hennerici, S. Meairs, *et al.*, "Mannheim Intima-Media Thickness Consensus: on Behalf of the Advisory Board of the 3rd Watching the Risk Symposium 2004, 13th European Stroke Conference, Mannheim, Germany, May 14, 2004," *Cerebrovascular Diseases*, vol. 18, no. 4, pp. 346–349, Dec. 2004, ISSN: 1015-9770. DOI: 10.1159/000081812. eprint: <https://karger.com/ced/article-pdf/18/4/346/2339250/000081812.pdf>. [Online]. Available: <https://doi.org/10.1159/000081812>.
- [68] M. J. Thubrikar and F. Robicsek, "Pressure-induced arterial wall stress and atherosclerosis," *The Annals of Thoracic Surgery*, vol. 59, no. 6, pp. 1594–1603, 1995, ISSN: 0003-4975. DOI: [https://doi.org/10.1016/0003-4975\(94\)01037-D](https://doi.org/10.1016/0003-4975(94)01037-D). [Online]. Available: <https://www.sciencedirect.com/science/article/pii/S000349759401037D>.
- [69] M. D. Ford, Y. J. Xie, B. A. Wasserman, and D. A. Steinman, "Is flow in the common carotid artery fully developed?" *Physiological Measurement*, vol. 29, no. 11, pp. 1335–1349, 2008. DOI: 10.1088/0967-3334/29/11/008.
- [70] K. R. Moyle, L. Antiga, and D. A. Steinman, "Inlet conditions for image-based cfd models of the carotid bifurcation: Is it reasonable to assume fully developed flow?," 2006.
- [71] I. C. Campbell, J. Ries, S. S. Dhawan, A. A. Quyyumi, W. R. Taylor, and J. N. Oshinski, "Effect of inlet velocity profiles on patient-specific computational fluid dynamics simulations of the carotid bifurcation," 2012.
- [72] D. Tang, C. Yang, S. Mondal, *et al.*, "A negative correlation between human carotid atherosclerotic plaque progression and plaque wall stress: In vivo mri-based 2d/3d fsi models," *Journal of biomechanics*, vol. 41, no. 4, pp. 727–736, 2008.

- 
- [73] D. Tang, C. Yang, G. Canton, Z. Wu, T. Hatsukami, and C. Yuan, “Correlations between carotid plaque progression and mechanical stresses change sign over time: A patient follow up study using mri and 3d fsi models,” *BioMedical Engineering OnLine*, vol. 12, pp. 1–12, 2013.
- [74] J. R. Cebral, P. J. Yim, R. Löhner, O. Soto, and P. L. Choyke, “Blood flow modeling in carotid arteries with computational fluid dynamics and mr imaging,” *Academic radiology*, vol. 9, no. 11, pp. 1286–1299, 2002.
- [75] W. E. Lorensen and H. E. Cline, “Marching cubes: A high resolution 3d surface construction algorithm,” in *Seminal graphics: pioneering efforts that shaped the field*, 1998, pp. 347–353.
- [76] P. J. Yim, J. J. Cebral, R. Mullick, H. B. Marcos, and P. L. Choyke, “Vessel surface reconstruction with a tubular deformable model,” *IEEE transactions on medical imaging*, vol. 20, no. 12, pp. 1411–1421, 2001.
- [77] L. Speelman, E. M. H. Bosboom, G. W. H. Schurink, *et al.*, “Initial stress and nonlinear material behavior in patient-specific aaa wall stress analysis,” *Journal of biomechanics*, vol. 42, no. 11, pp. 1713–1719, 2009.
- [78] S. De Putter, B. Wolters, M. Rutten, M. Breeuwer, F. Gerritsen, and F. Van de Vosse, “Patient-specific initial wall stress in abdominal aortic aneurysms with a backward incremental method,” *Journal of biomechanics*, vol. 40, no. 5, pp. 1081–1090, 2007.
- [79] M. D. Ford, N. Alperin, S. H. Lee, D. W. Holdsworth, and D. A. Steinman, “Characterization of volumetric flow rate waveforms in the normal internal carotid and vertebral arteries,” *Physiological measurement*, vol. 26, no. 4, p. 477, 2005.
- [80] K. Perktold, M. Resch, and R. O. Peter, “Three-dimensional numerical analysis of pulsatile flow and wall shear stress in the carotid artery bifurcation,” *Journal of Biomechanics*, vol. 24, no. 6, pp. 409–420, 1991.
- [81] S. Zhao, B. Ariff, Q. Long, *et al.*, “Inter-individual variations in wall shear stress and mechanical stress distributions at the carotid artery bifurcation of healthy humans,” *Journal of Biomechanics*, vol. 35, no. 10, pp. 1367–1377, 2002, ISSN: 0021-9290. DOI: [https://doi.org/10.1016/S0021-9290\(02\)00185-9](https://doi.org/10.1016/S0021-9290(02)00185-9). [Online]. Available: <https://www.sciencedirect.com/science/article/pii/S0021929002001859>.
- [82] B. Sui, P. Gao, Y. Lin, H. Qin, L. Liu, and G. Liu, “Noninvasive determination of spatial distribution and temporal gradient of wall shear stress at common carotid artery,” *Journal of Biomechanics*, vol. 41, no. 14, pp. 3024–3030, 2008, ISSN: 0021-9290. DOI: <https://doi.org/10.1016/j.jbiomech.2008.07.026>. [Online]. Available: <https://www.sciencedirect.com/science/article/pii/S0021929008003722>.
- [83] K. Dilba, D. H. van Dam-Nolen, S.-A. Korteland, *et al.*, “The association between time-varying wall shear stress and the development of plaque ulcerations in carotid arteries from the plaque at risk study,” *Frontiers in cardiovascular medicine*, vol. 8, p. 732 646, 2021.
- [84] A. Moerman, S. Korteland, K. Dilba, *et al.*, “The correlation between wall shear stress and plaque composition in advanced human carotid atherosclerosis,” *Frontiers in Bioengineering and Biotechnology*, vol. 9, p. 828 577, 2022.
- [85] H. Gao, Q. Long, M. Graves, J. H. Gillard, and Z.-Y. Li, “Carotid arterial plaque stress analysis using fluid–structure interactive simulation based on in-vivo magnetic resonance images of four patients,” *Journal of Biomechanics*, vol. 42, no. 10, pp. 1416–1423, 2009, ISSN: 0021-9290. DOI: <https://doi.org/10.1016/j.jbiomech>.

- 2009.04.010. [Online]. Available: <https://www.sciencedirect.com/science/article/pii/S0021929009002048>.
- [86] R. S. Salzar, M. J. Thubrikar, and R. T. Eppink, "Pressure-induced mechanical stress in the carotid artery bifurcation: A possible correlation to atherosclerosis," *Journal of biomechanics*, vol. 28, no. 11, pp. 1333–1340, 1995.
- [87] A. Veress, D. Vince, P. M. Anderson, *et al.*, "Vascular mechanics of the coronary artery," *Zeitschrift für Kardiologie*, vol. 89, S092–S100, 2000.
- [88] A. Augst, B. Ariff, S. McG. Thom, X. Xu, and A. D. Hughes, "Analysis of complex flow and the relationship between blood pressure, wall shear stress, and intima-media thickness in the human carotid artery," *American Journal of Physiology-heart and circulatory physiology*, vol. 293, no. 2, H1031–H1037, 2007.
- [89] M. Cibis, W. V. Potters, M. Selwaness, *et al.*, "Relation between wall shear stress and carotid artery wall thickening mri versus cfd," *Journal of Biomechanics*, vol. 49, no. 5, pp. 735–741, 2016, ISSN: 0021-9290. DOI: <https://doi.org/10.1016/j.jbiomech.2016.02.004>. [Online]. Available: <https://www.sciencedirect.com/science/article/pii/S0021929016300987>.
- [90] E. M. Hartman, G. De Nisco, F. J. Gijssen, *et al.*, "The definition of low wall shear stress and its effect on plaque progression estimation in human coronary arteries," *Scientific Reports*, vol. 11, no. 1, p. 22 086, 2021.
- [91] C. Costopoulos, L. H. Timmins, Y. Huang, *et al.*, "Impact of combined plaque structural stress and wall shear stress on coronary plaque progression, regression, and changes in composition," *European heart journal*, vol. 40, no. 18, pp. 1411–1422, 2019.
- [92] Z.-Y. Li, S. Howarth, T. Tang, M. Graves, J. U-King-Im, and J. H. Gillard, "Does calcium deposition play a role in the stability of atheroma? location may be the key," *Cerebrovascular diseases*, vol. 24, no. 5, pp. 452–459, 2007.
- [93] S. Yamada, M. Oshima, Y. Watanabe, H. Ogata, K. Hashimoto, and H. Miyake, "Intramural location and size of arterial calcification are associated with stenosis at carotid bifurcation," *European Journal of Radiology*, vol. 83, no. 6, pp. 957–963, 2014, ISSN: 0720-048X. DOI: <https://doi.org/10.1016/j.ejrad.2014.02.009>. [Online]. Available: <https://www.sciencedirect.com/science/article/pii/S0720048X1400076X>.
- [94] P. J. Roache, *Verification and validation in computational science and engineering*. Hermosa Albuquerque, NM, 1998, vol. 895.
- [95] S. Saitta, S. Pirola, F. Piatti, *et al.*, "Evaluation of 4d flow mri-based non-invasive pressure assessment in aortic coarctations," *Journal of biomechanics*, vol. 94, pp. 13–21, 2019.
- [96] S. A. Maas, G. A. Ateshian, and J. A. Weiss, "Febio: History and advances," *Annual review of biomedical engineering*, vol. 19, pp. 279–299, 2017.
- [97] Intel. "Direct sparse solver (dss) interface routines." (2023), [Online]. Available: <https://www.intel.com/content/www/us/en/docs/onemkl/developer-reference-c/2023-1/direct-sparse-solver-dss-interface-routines.html> (visited on 10/24/2023).
- [98] FEBio. "Febio user manual." (2023), [Online]. Available: <https://help.febio.org/docs/FEBioUser-4-0/UM40-Subsection-9.2.3.html> (visited on 10/24/2023).

# A

## Reconstruction

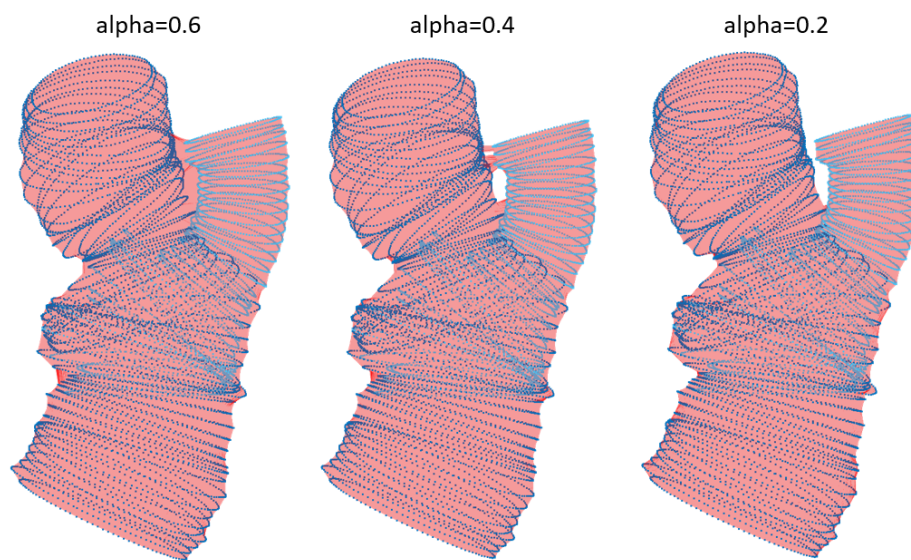


**Figure A.1: Contour and alpha shape result with different alpha values.** Light Blue: CCA-ECA Vessel; Dark Blue: CCA-ICA Vessel.

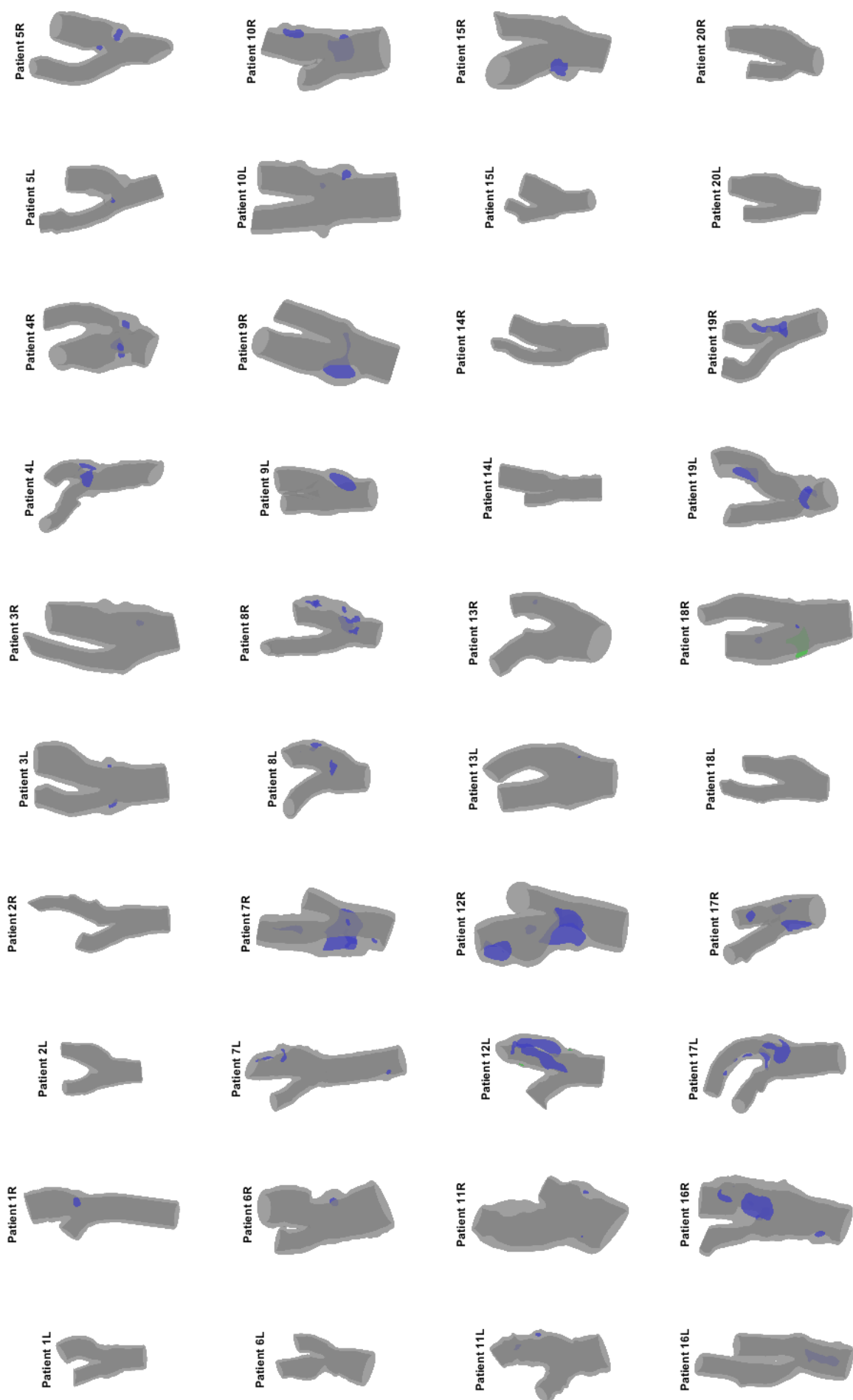


Figure A.2: Reconstruction result of patient 1-20 before adding the extension. Blue: calcium; green: lipid.

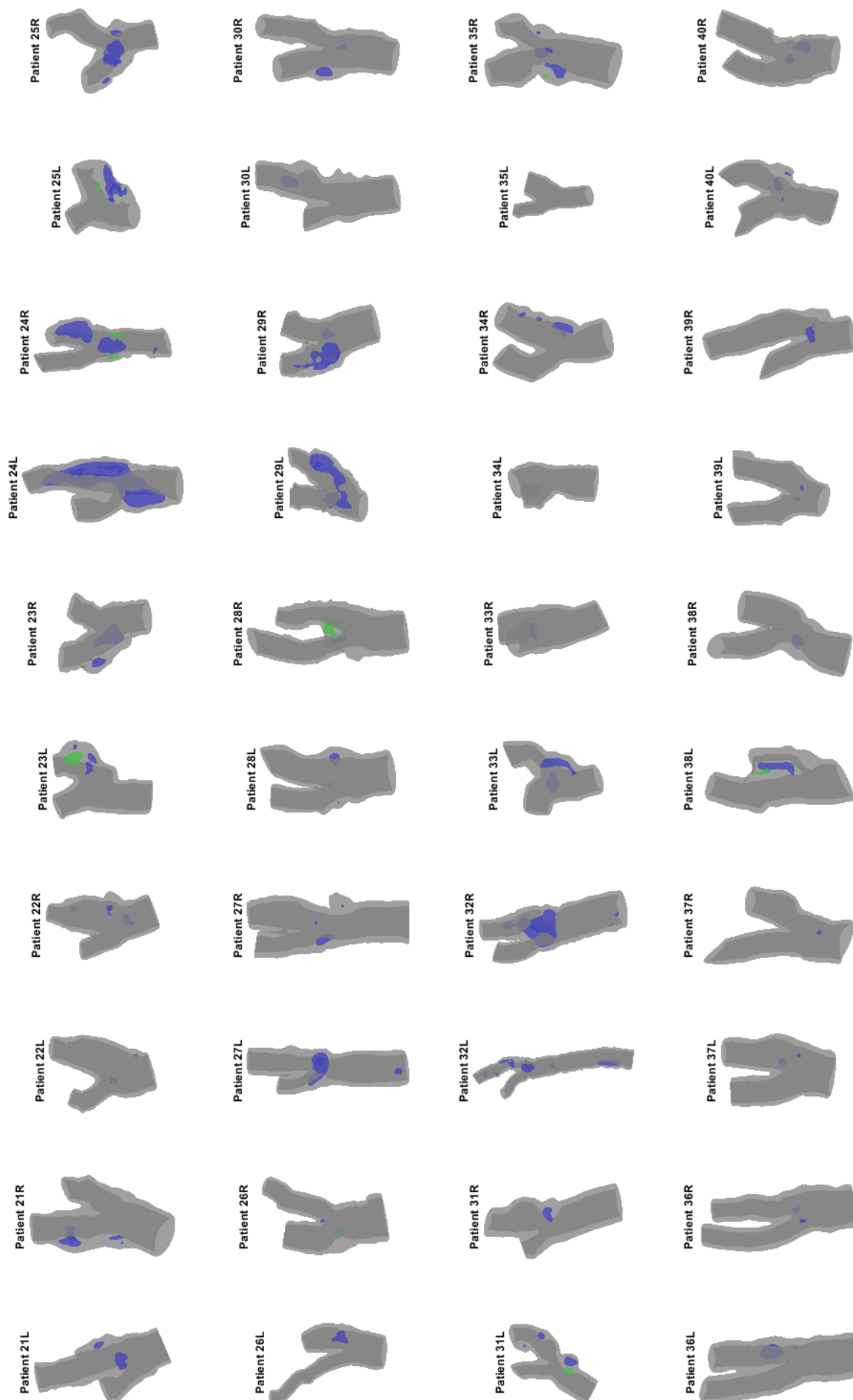


Figure A.3: Reconstruction result of patient 21-40 before adding the extension. Blue: calcium; green: lipid.

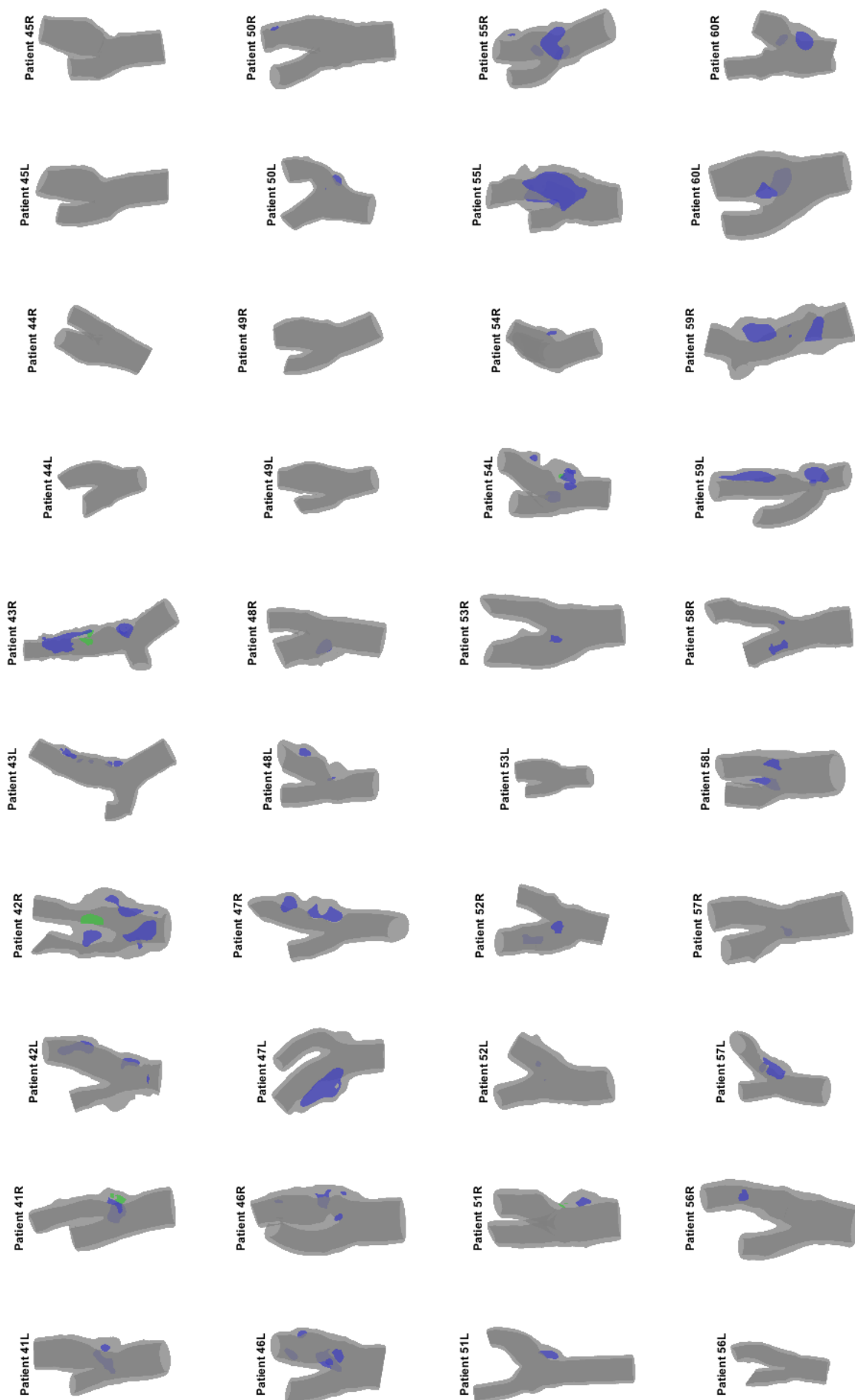


Figure A.4: Reconstruction result of patient 41-60 before adding the extension. Blue: calcium; green: lipid.

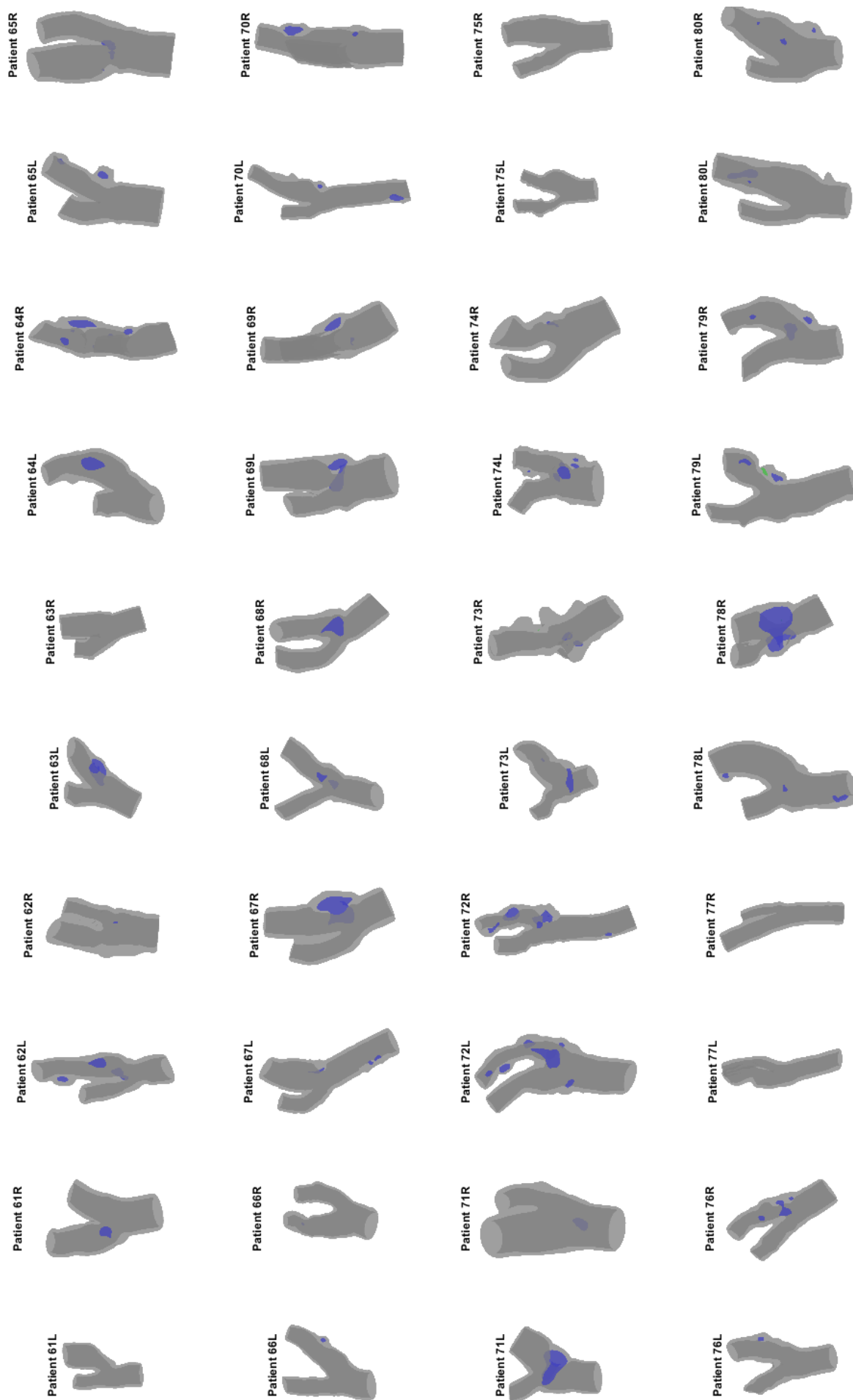


Figure A.5: Reconstruction result of patient 61-80 before adding the extension. Blue: calcium; green: lipid.

# B

## Validation of Backward Incremental Method

### B.1. Ring Model

Tetrahedral mesh was employed for modeling a ring structure, characterized by an inner radius of 1 mm, an outer radius of 2 mm, and a height of 0.5 mm. Deformation along the z-axis was constrained for both upper and lower surfaces. To avoid movement of the entire model, one node on the inner circle was fixed in three axes. For material properties, a nonlinear hyperelastic Neo-Hookean model was utilized, with detailed parameters outlined in 2.3.2. The specific values chosen were  $E = 0.6$  MPa for Young's modulus and  $\nu = 0.4$  for Poisson's ratio. Given the utilization of the FEBio Prestrain feature, the material was set as *Prestrain Elastic*, employing the *neo-Hookean* hyperelastic model [50].

The analysis began with a forward finite element simulation, involving the application of a 50 kPa pressure to the inner surface. This step aimed to replicate the deformed structure as it would appear in the captured image. Following this, nodal coordinates were extracted from the forward analysis and used as the initial geometry for the subsequent backward incremental analysis. In the backward incremental analysis, an initial pressure of  $p_i = 50$  kPa was set. Once the initial stress stage reached, a final pressure was applied. In order to obtain the actual stress distribution result, another simulation was conducted, starting from a zero-pressure state but with the final pressure applied. The resultant stress served as the reference for comparison. The simulations were performed using three different iterations (16, 24, and 32). The stress distribution at the initial stress stage (Stage 1) and after final pressure was applied (Stage 2) were extracted. All simulations were conducted employing the two methods. The process was visually demonstrated in Figure B.1.

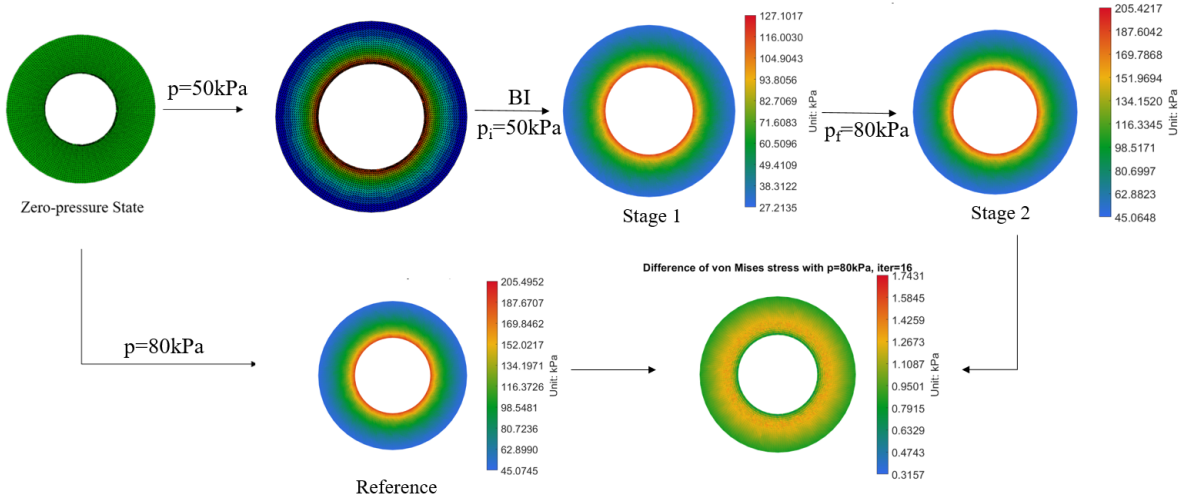


**Figure B.1: Verification using the ring model.** A pressure of 50 kPa was first applied on the inner surface at zero-pressure geometry. The deformed geometry was taken as the starting geometry for backward incremental analysis with  $p_i$  kPa. A final pressure was then applied using the input from backward incremental analysis. The reference stress distribution was calculated by applying the final pressure on undeformed geometry as the reference. The stresses from stage 2 were then compared with the reference.

Two different approaches for implementing the Backward Incremental method in FEBio were initially tested using a simplified ring model with varying optimal iteration numbers. The maximum von Mises stress results were presented in Table B.1. The element-wise differences were computed, and the maximum difference was shown in Figure B.2. The colormap plot of the stress distribution of each model was provided in Appendix B.1. With increasing iteration numbers, there were slight variations in the stress values for all methods and stages. Furthermore, Method 1 yielded a maximum von Mises stress value that closely matched the reference model. However, upon a detailed comparison of stress element-wise, Method 1 exhibited a higher difference than Method 2 across all iterations and stages. Therefore, using an iteration number of 16 showed promise.

**Table B.1:** Maximum Von Mises Stress Results of Ring Model for Different Methods and Iteration Numbers [kPa]

	Reference		Method 1		Method2	
	Stage 1	Stage 2	Stage 1	Stage 2	Stage 1	Stage 2
<b>i=16</b>	127.2	205.3	127.10	205.42	127.39	205.99
<b>i=24</b>	127.2	205.3	127.15	205.47	127.37	205.99
<b>i=32</b>	127.2	205.3	127.17	205.50	127.36	205.99

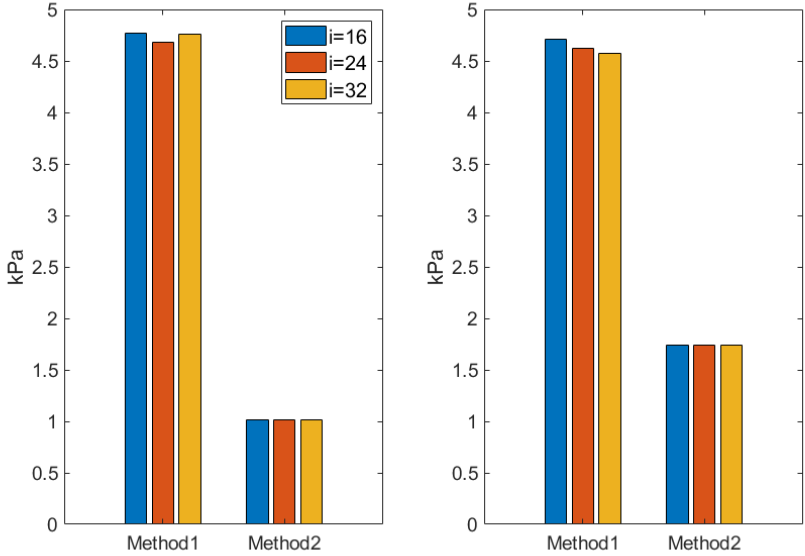


Figure B.2: Max difference of von Mises stress of different methods and iteration numbers. Stage 1: Left, Stage 2: Right.

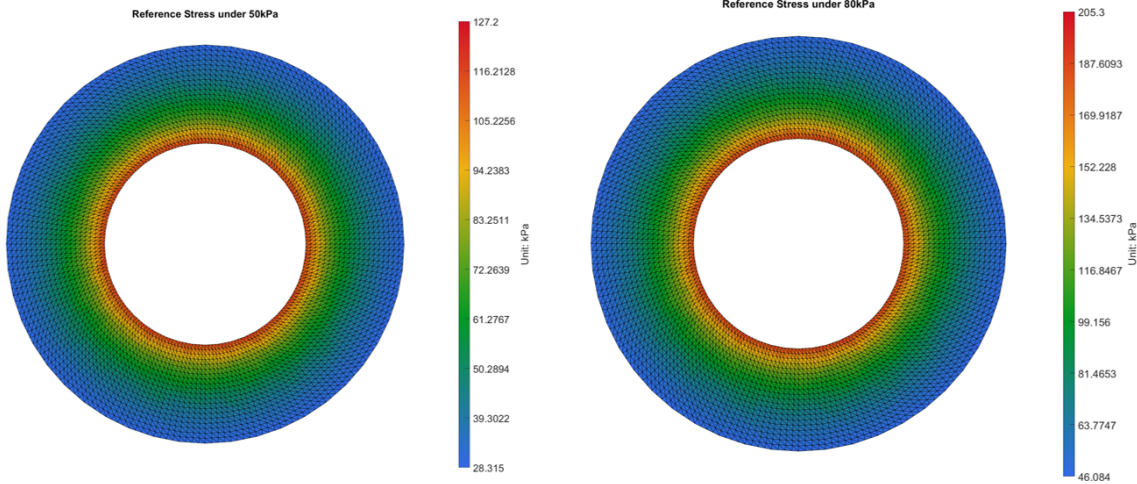
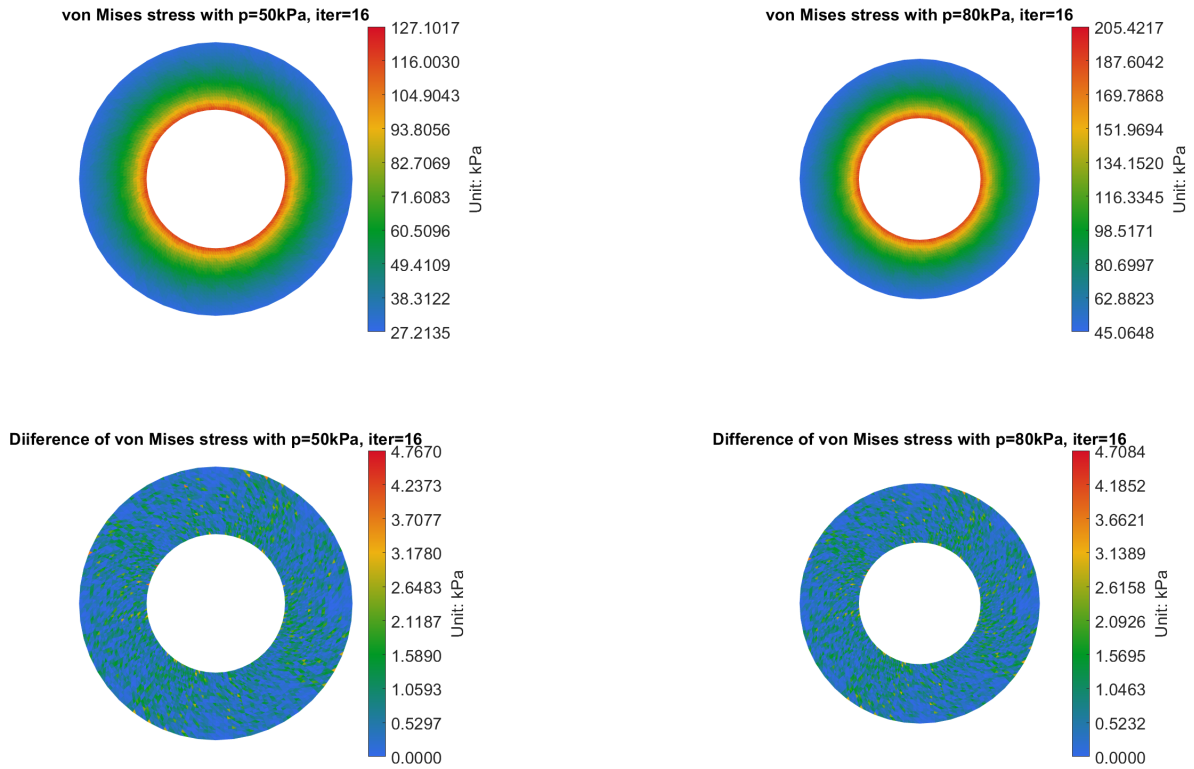
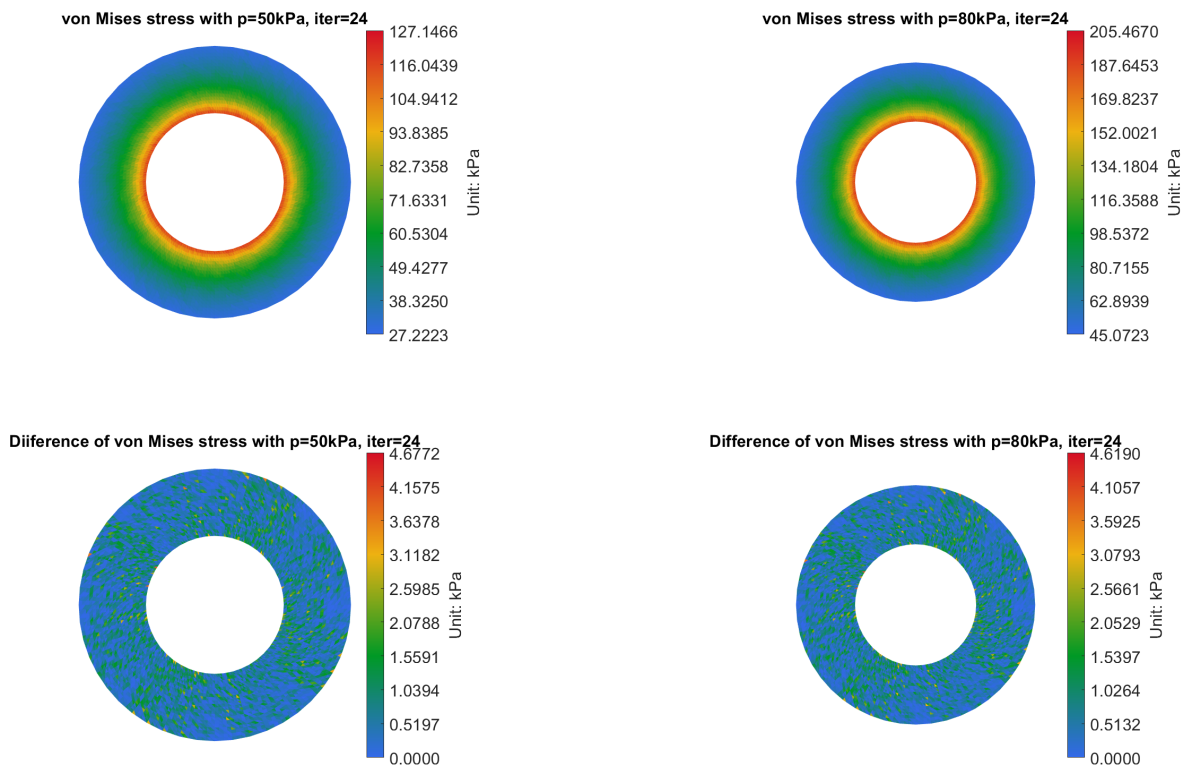


Figure B.3: The Von Mises stress result with Stage 1 (Left) and Stage 2 (Right) applying on undefromed geometry.



**Figure B.4:** The Von Mises stress result obtained using Method 1 with 16 iterations was compared to the reference result to calculate the difference. Stage 1: Left, Stage 2: Right.



**Figure B.5:** The Von Mises stress result obtained using Method 1 with 24 iterations was compared to the reference result to calculate the difference. Stage 1: Left, Stage 2: Right.

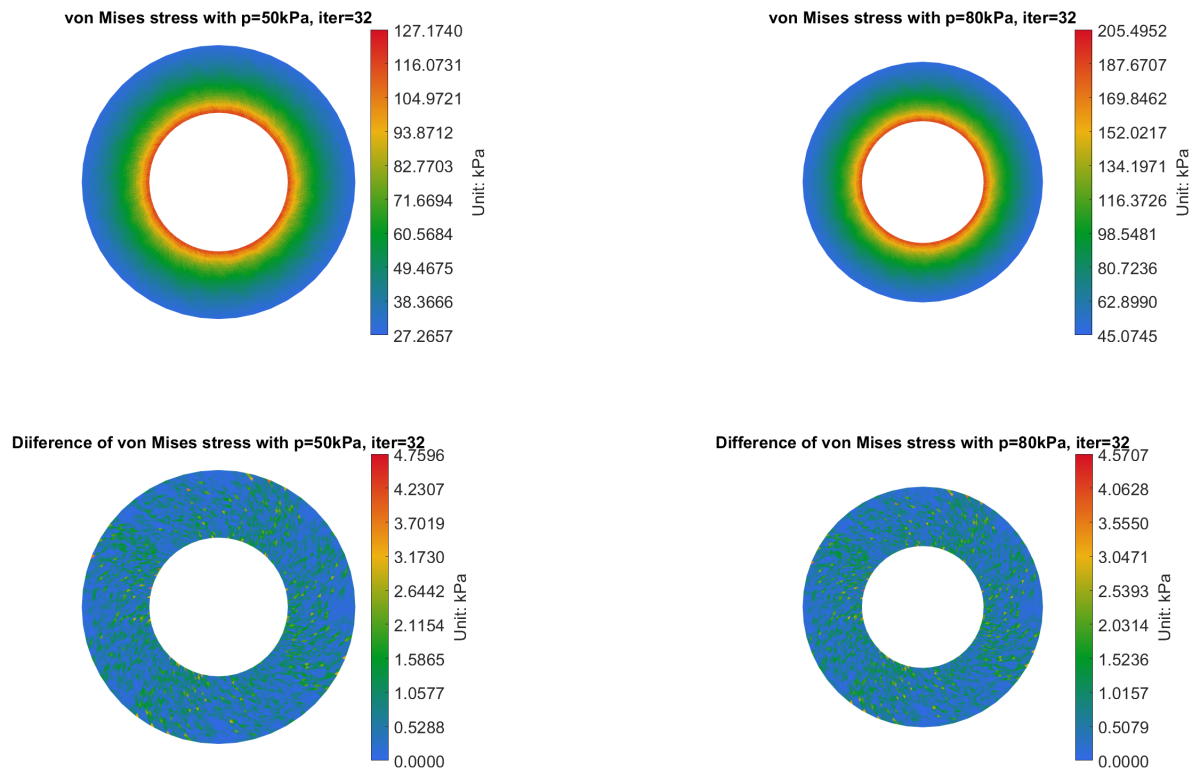


**Figure B.6:** The Von Mises stress result obtained using Method 1 with 32 iterations was compared to the reference result to calculate the difference. Stage 1: Left, Stage 2: Right.

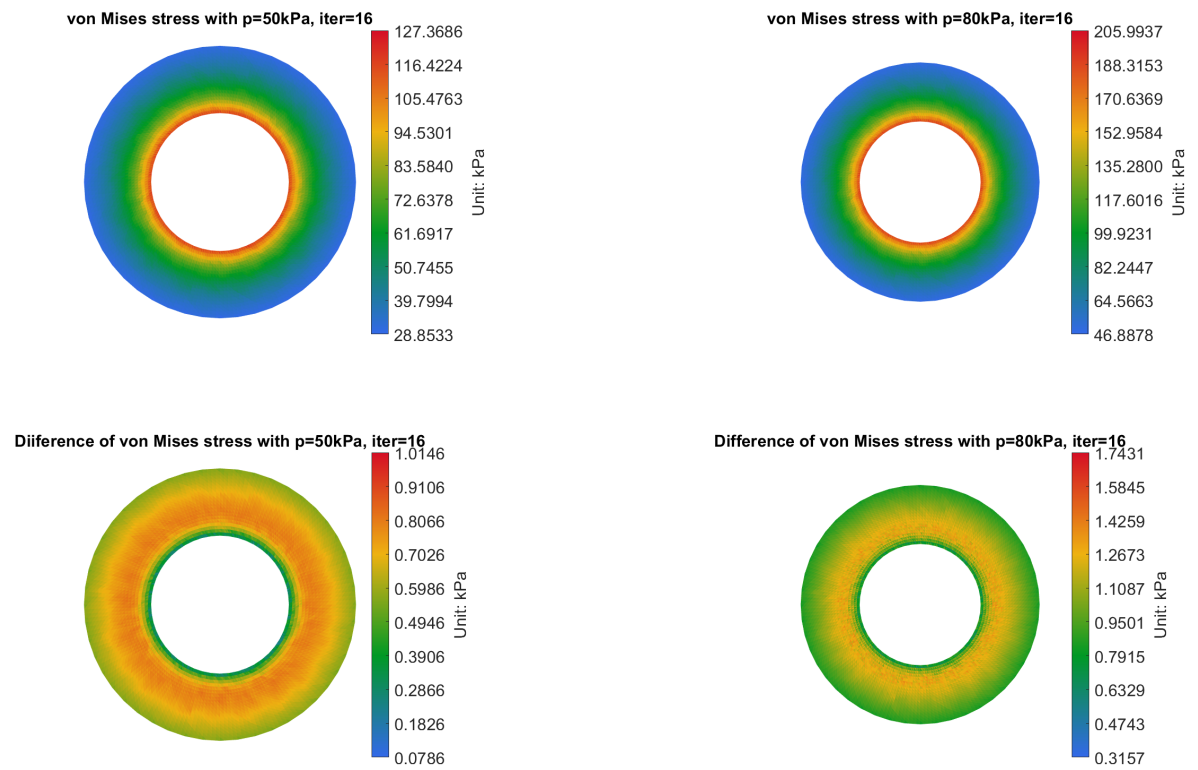


**Figure B.7:** The Von Mises stress result obtained using Method 2 with 16 iterations was compared to the reference result to calculate the difference. Stage 1: Left, Stage 2: Right.

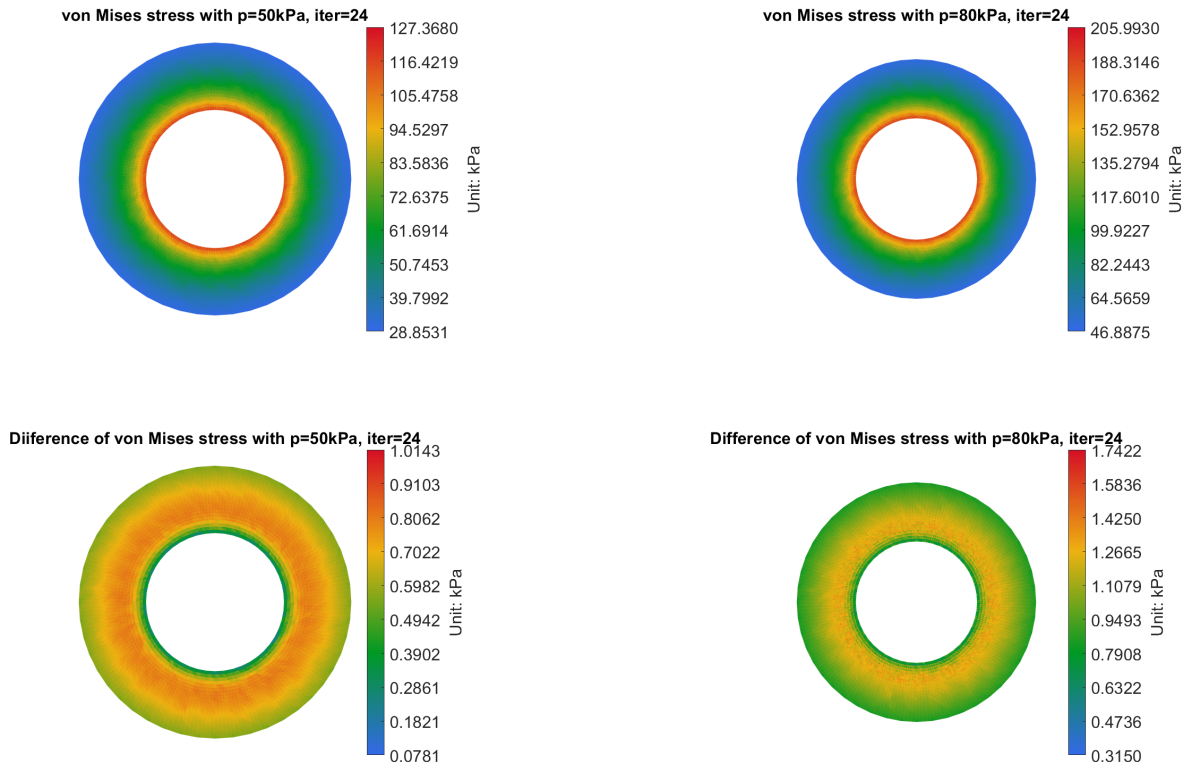


**Figure B.8:** The Von Mises stress result obtained using Method 2 with 24 iterations was compared to the reference result to calculate the difference. Stage 1: Left, Stage 2: Right.

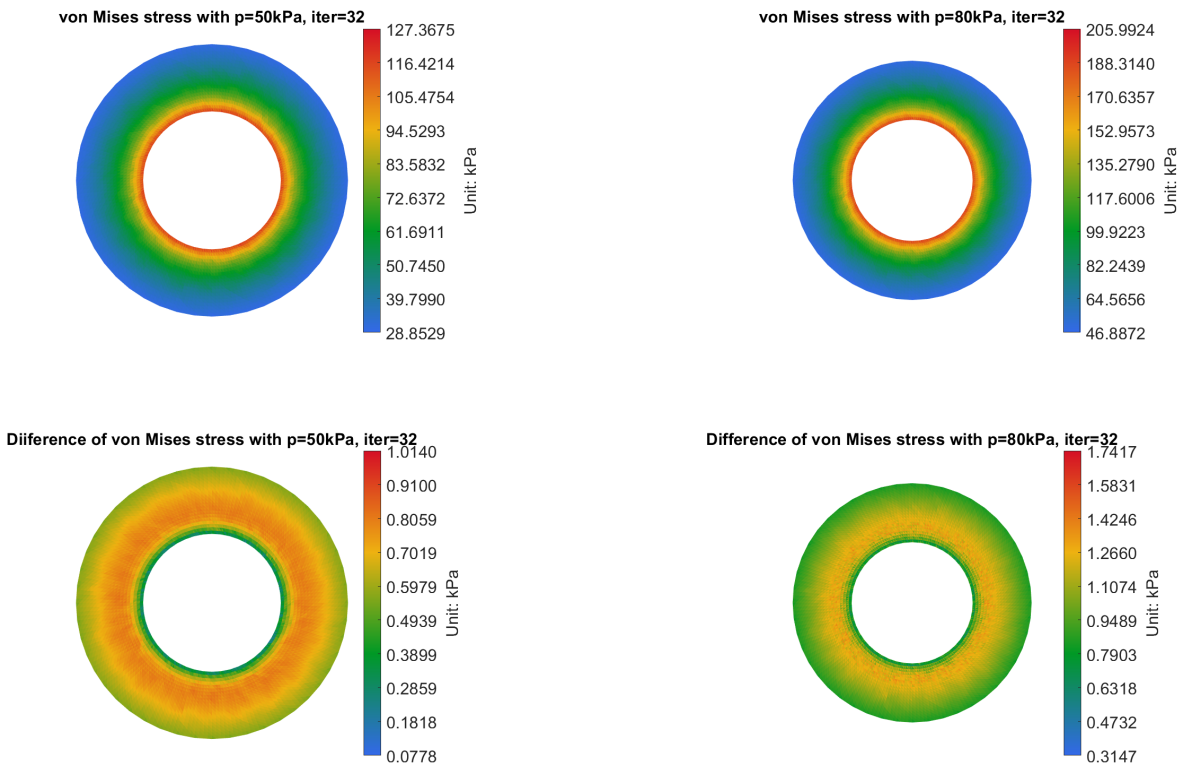


**Figure B.9:** The Von Mises stress result obtained using Method 2 with 32 iterations was compared to the reference result to calculate the difference. Stage 1: Left, Stage 2: Right.

# B.2. Artery Model

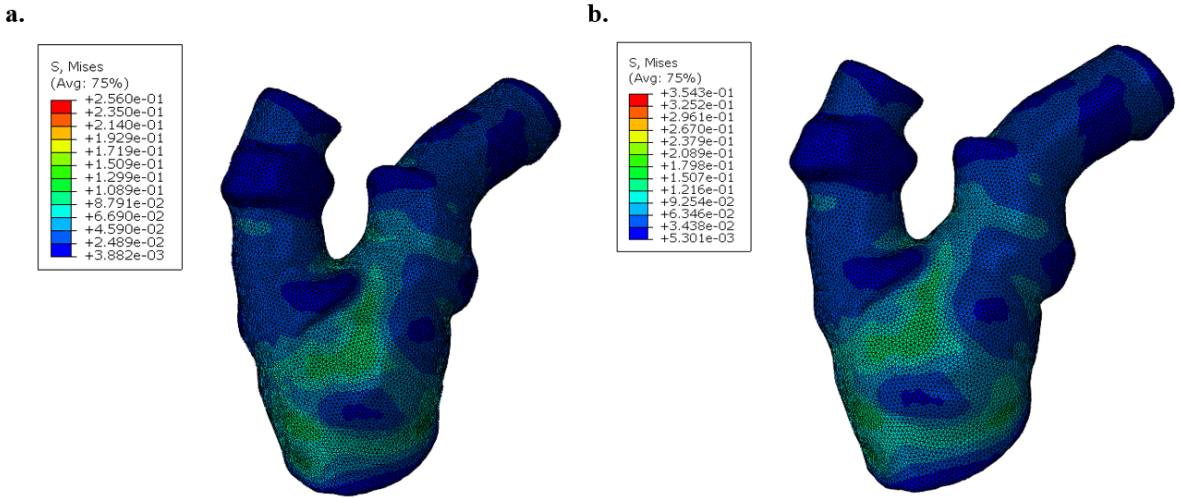


Figure B.10: The Von Mises stress result of Stage 1 (a) and Stage 2 (b) from abaqus.

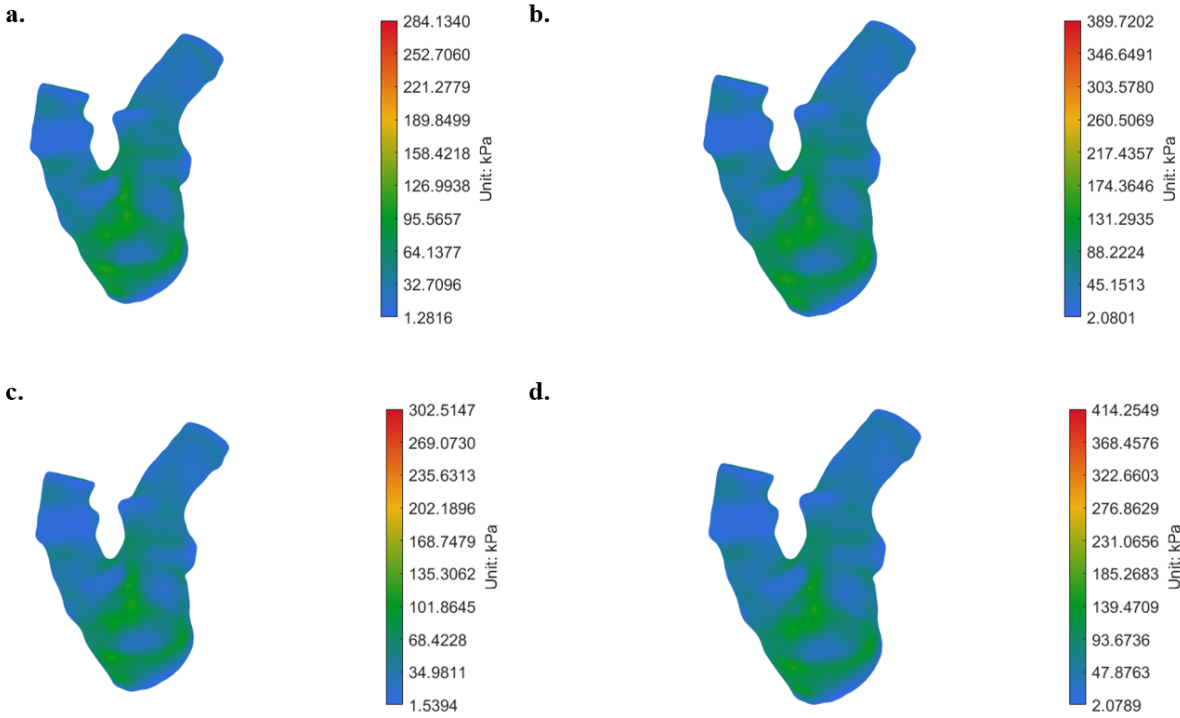


Figure B.11: The Von Mises stress result obtained using Method 1. a. iteration = 16, Stage 1. c. iteration = 16, Stage 2. b. iteration = 24, Stage 1. d. iteration = 24, Stage 2.

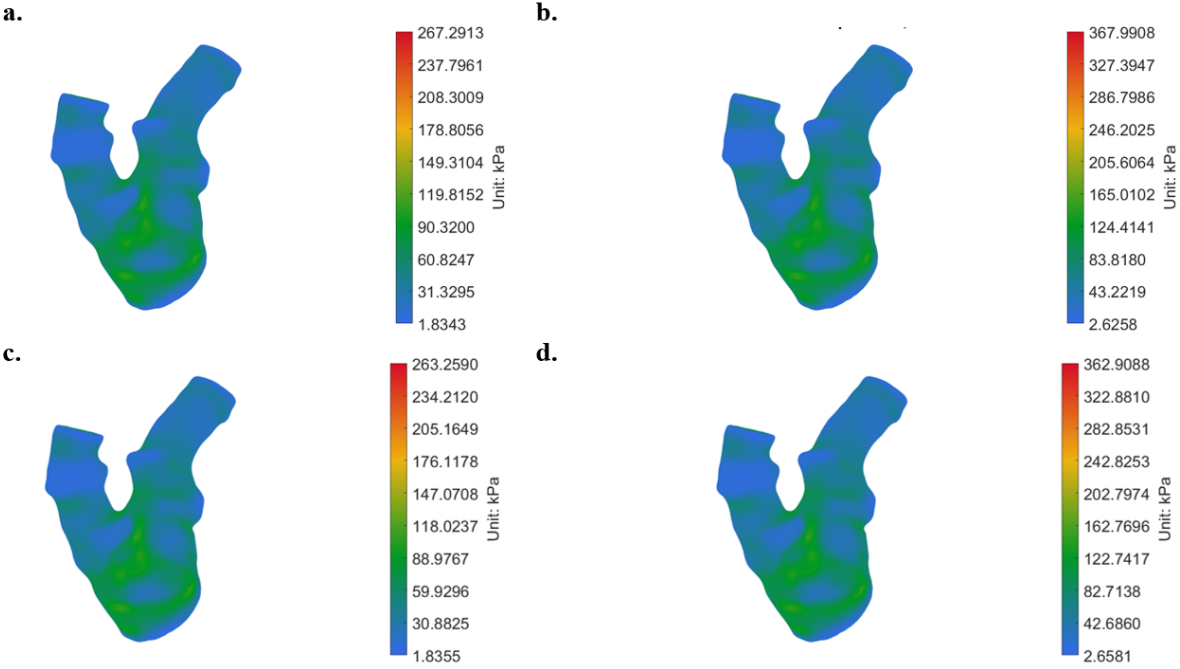


Figure B.12: The Von Mises stress result obtained using Method 2. a. iteration = 16, Stage 1. c. iteration = 16, Stage 2. a. iteration = 24, Stage 1. a. iteration = 24, Stage 2.

### B.3. Ogen Material Model

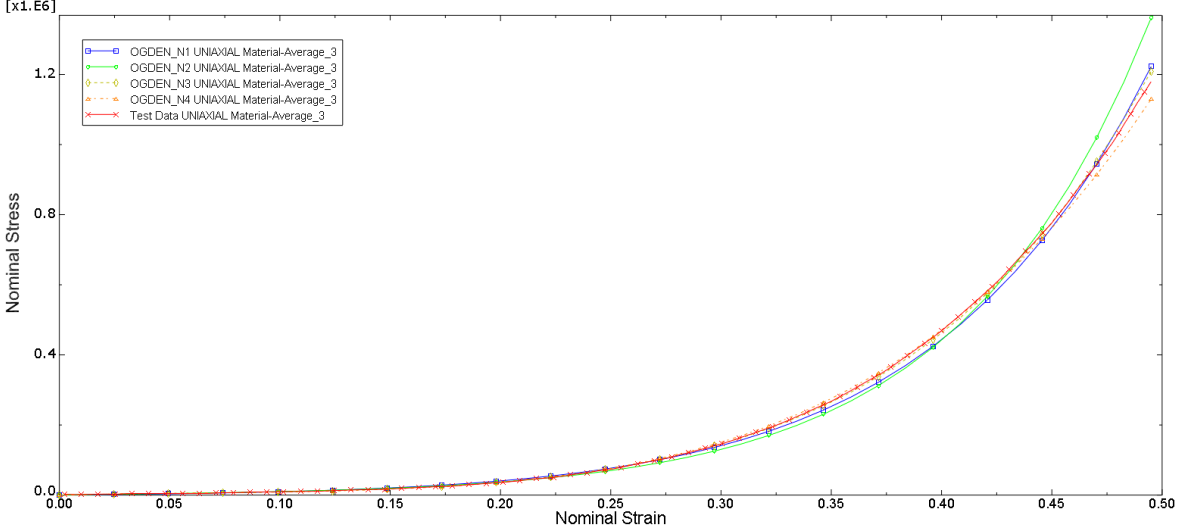


Figure B.13: Stress–stretch data points obtained from [53], with corresponding fitted curves using Ogden strain energy density functions (N=1,2,3,4).

# C

## Mesh Convergence Study

To ensure the reliability of results, mesh convergence study was performed for solid domain and fluid domain separately. Grid Convergence Index (GCI) was calculated to measure the difference between the computed value and the asymptotic numerical value [94], thus indicated how much the variable of interest would change with further refinement. Refine index  $r$  was first obtained from three different element number (fine: $N_1$ ; medium: $N_2$  and coarse: $N_3$ ):

$$r \approx \left(\frac{N_1}{N_2}\right)^{1/3} \approx \left(\frac{N_2}{N_3}\right)^{1/3} \quad (\text{C.1})$$

Using these three meshes, simulations were performed and the variable of interest was recorded as  $f_1, f_2, f_3$ , respectively. Thus the order of convergence was

$$p = \frac{\log\left(\frac{f_3 - f_2}{f_2 - f_1}\right)}{\log(r)} \quad (\text{C.2})$$

The GCI was calculated as

$$GCI_{1,2} = F_S |E_1| \quad (\text{C.3})$$

$$GCI_{2,3} = F_S |E_2| \quad (\text{C.4})$$

where  $E_1$  and  $E_2$  are estimated percent errors and

$$E_1 = \frac{f_2 - f_1}{f_1} \quad (\text{C.5})$$

$$E_2 = \frac{f_3 - f_2}{f_2} \quad (\text{C.6})$$

The safety factor  $F_S$  was set as 1.25 [95]. The ratio  $k \approx 1$  was then calculated to ensure that each grid level yield solution was in the asymptotic range of convergence for the computed solution.

$$k = \frac{GCI_{2,3}}{r^p GCI_{1,2}} \quad (\text{C.7})$$

## C.1. Solid Domain

In the solid domain, a pressure of 10 kPa was uniformly applied to the inner surface of the vessel wall in a single analysis step. Additionally, boundary conditions were enforced such that the displacement of the inlet and two outlet curves was restricted along all three axes. This comprehensive study encompassed six models derived from three distinct patients, each exhibiting varying node spacing ranging from 0.4 mm to 0.3 mm. The maximum von Mises stress was utilized as the variable of interest.

The results, presented in Table C.1, showcased minimal values for Grid Convergence Index (GCI) and estimated fractional error (E) across all six cases, affirming the convergence of the mesh. In light of these findings, the seed size was universally established at 0.3 mm for all cases, ensuring consistent and reliable results across the board.

**Table C.1:** Mesh Convergence Result of Solid Domain

	Patient 4		Patient 5		Patient 6	
	LEFT	RIGHT	LEFT	RIGHT	LEFT	RIGHT
<b>Grid1[MPa]</b>	0.2494	0.387	0.163	0.2491	0.213	0.3597
<b>Grid2[MPa]</b>	0.2447	0.3899	0.1529	0.2402	0.2034	0.3377
<b>Grid3[MPa]</b>	0.2367	0.3724	0.1496	0.1612	0.1825	0.2653
<i>GCI</i> <sub>1,2</sub> (%)	4.01	0.57	3.36	0.19	4.79	3.34
<i>E</i> <sub>1</sub> (%)	0.15	2.68	0.45	9.20	2.67	3.83
<b>k</b>	1.066	1.037	1.019	0.992	1.047	1.065

## C.2. Fluid Domain

**Table C.2:** Element Settings and Maximum Edge Sizes Analysis for Fluid Domain

Element Setting [mm]	Element Number	Maximum Edge Size [mm]	
		Average	Min
0.4	195,333	0.490	0.314
0.35	282,611	0.429	0.270
0.3	435,676	0.384	0.234

In the fluid domain, a steady flow simulation was conducted. The right carotid artery model from patient AMC005 was used. A steady flow rate corresponding to a systolic peak was imposed at the inlet with a parabolic profile. Within the timeframe of 0 to 1 second, the flow rate increased from zero to the systolic peak at the inlet, maintaining this peak velocity from 1 to 1.4 seconds. All other boundary conditions remained consistent with the FSI simulation. The results were extracted from the state at 1.4 seconds. Four variables were considered as variables of interest: maximum inlet velocity, maximum ICA outlet velocity, maximum ECA outlet velocity, maximum pressure, and maximum shear stress. Given the high sensitivity of

the maximum values to grid changes, the 99% maximum value was adopted as a more reliable indicator.

Three meshes were generated using TetGen, with element sizes set at 0.4 mm, 0.35 mm, and 0.3 mm. The resulting element numbers and maximum edge sizes are presented in Table C.2. Notably, as illustrated in Table C.3, the finest grid exhibited exceptional accuracy, yielding GCI values and  $E_1$  values of less than 2%. The proximity of the ratio  $k$  to 1 further confirmed that the finest grid fell within the range of convergence.

Furthermore, an investigation into the number of segments in the boundary layer was conducted. Segments of 6, 8, and 10 were employed while maintaining a consistent total thickness. The results were displayed in Table C.4. The GCIs of the 6-segment and 8-segment models were small. Therefore, in consideration of reducing simulation time, the 6-segment model was chosen for this project.

**Table C.3:** Mesh Convergence Result of the Fluid Domain with Different Element Numbers.

	<b>max velocity</b> CCA [m/s]	<b>max velocity</b> ICA [m/s]	<b>max velocity</b> ECA [m/s]	<b>max</b> Pressure[Pa]	<b>max</b> Shear Stress [Pa]
<b>Grid 1</b>	1.618	0.869	1.385	30376.66	34.505
<b>Grid 2</b>	1.618	0.862	1.392	30348.38	34.644
<b>Grid 3</b>	1.621	0.879	1.388	30364.71	34.190
$GCI_{1,2}[\%]$	-	0.713	1.196	0.275	0.222
$E_1[\%]$	-	0.745	1.457	0.300	1.596
<b>k</b>	-	0.995	1.001	0.996	1.008

**Table C.4:** Mesh Convergence Result of the Fluid Domain with Different Segment Numbers of the Boundary Layer.

	<b>Segments</b>	<b>max velocity</b> CCA [m/s]	<b>max velocity</b> ICA [m/s]	<b>max velocity</b> ECA [m/s]	<b>max</b> Pressure [Pa]	<b>max</b> Shear Stress [Pa]
<b>Grid 1</b>	6	1.618	0.862	1.392	30348.38	34.646
<b>Grid 2</b>	8	1.619	0.867	1.391	30353.51	36.319
<b>Grid 3</b>	10	1.616	0.868	1.390	30357.9	36.564
$GCI_{1,2} \%$		0.341	0.005	0.174	0.108	0.144
$E_1 \%$		-0.024	10.5775	0.0648	-0.115	-9.417
<b>k</b>		0.998	1.001	0.9995	1.0001	1.007

# D

## FSI

### D.1. Fluid-Structure Interaction Module in FEBio

FEBio is an open-source finite element software specifically developed for the biomechanics and biophysics communities [96]. The FSI implementation in FEBio defines the fluid domain as a mixture of solid and fluid materials. The solid material serves to regulate mesh motion and has zero density, resulting in zero momentum, and negligible elasticity, allowing the solid traction to be disregarded. Within this fluid domain, there is no frictional interaction between the fluid and solid materials. The nodal Degrees of Freedom (DOFs) in the fluid domain are defined as fluid velocity, fluid dilatation, and solid displacement. Therefore, the governing equations for the fluid domain are [64]

$$div\sigma^s = 0 \quad (D.1)$$

(Momentum of the solid material)

$$\rho^f \mathbf{a}^f = div\sigma^f + \rho^f \mathbf{b} \quad (D.2)$$

(Momentum balance of the fluid material)

$$\frac{1}{J^f}(\dot{J}^f + grad J^f \mathbf{w}) = div \mathbf{w} + \frac{\dot{J}^s}{J^s} \quad (D.3)$$

(Kinematic constraint)

where  $\sigma$  is the stress tensor,  $\rho$  is the material density,  $\mathbf{v}$  is the velocity vector,  $\mathbf{b}$  is the body force,  $J$  is the Jacobian of deformation, and  $\mathbf{w}$  is the fluid velocity.

The deformable interfaces between the solid and fluid domains share common nodes and displacements. The traction boundary condition is enforced on the interface, where the traction acting on the fluid domain  $\mathbf{t}^f$  is equal and opposite to the traction acting on the solid domain  $\mathbf{t}^s$ :

$$\mathbf{t}^s \times \mathbf{n} = -\mathbf{t}^f \times \mathbf{n}|_{interface} \quad (D.4)$$

$$\mathbf{u}^s = \mathbf{u}^f|_{interface} \quad (D.5)$$

where  $\mathbf{t}$  is the traction and  $\mathbf{u}$  is the displacement vector.

The numerical solution of the nonlinear system of equations is achieved through an initial iteration employing Newton's method, which is then followed by Broyden quasi-Newton updates [64]. Regarding Newton updates, FEBio provides a range of linear equation solvers. In this project, the DSS (Direct-Sparse-Solver) from the Intel oneAPI Math Kernel library [97] was selected for its promising performance, particularly in cases involving non-symmetric coefficient matrices, where it outperforms other solvers [98].

## D.2. Comparison of 2nd cycle and 4th cycle

The simulation was conducted over two cardiac cycles, with results obtained from the second cycle. To ensure result reliability, an initial simulation for four cycles was performed on the right carotid artery model. The inlet velocity profile settings were shown in Figure D.1a. All other loading conditions remained consistent with the explanations provided in Section 2.4.3. The corresponding flow results at the inlet and outlets were presented in Figure D.1b. The ratio of ICA to ECA flow aligned with the assumed ratio of 0.64:0.36. Subsequently, the flow data from the second and fourth cycles were compared, revealing a small difference of 2.5%. This observation indicates that the flow stabilized after the second cycle.

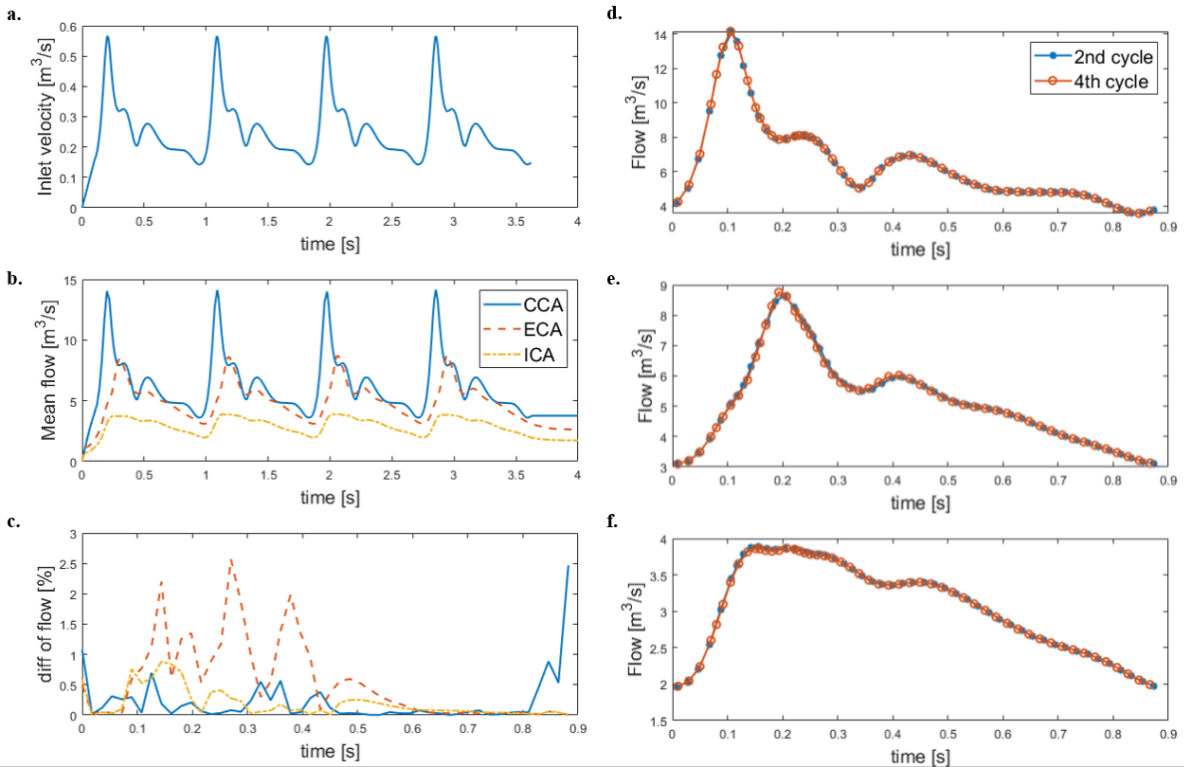


**Figure D.1: Comparison of flow between the 2nd and 4th cycles.** a. Inlet velocity profile settings. b. Inlet and outlet flow results. c. Percentage difference in inlet and outlet flow between the 2nd and 4th cycles. d. Comparison of CCA inlet flow between the 2nd and 4th cycles. e. Comparison of ECA outlet flow between the 2nd and 4th cycles. f. Comparison of ICA outlet flow between the 2nd and 4th cycles.

Moreover, biomechanical parameters such as fluid shear stress and von Mises stress were com-

pared. The fluid shear stress was extracted from the bifurcation point where the maximum shear stress was observed (Figure D.2a). Although a higher difference was noted between approximately 0.1s and 0.43s at the start of a cardiac cycle due to the rapid change in shear stress, the curves still aligned with each other (Figure D.2c and d). In order to mitigate this difference, the time step setting was adjusted to half of the original time step used in the simulation, resulting in a time step of 0.01s. Von Mises stress results were obtained from a point on the plaque cap (Figure D.2e). The maximum difference was found at 0.15s with a value of 1.4%. This result also indicates stabilization after the second cycle.

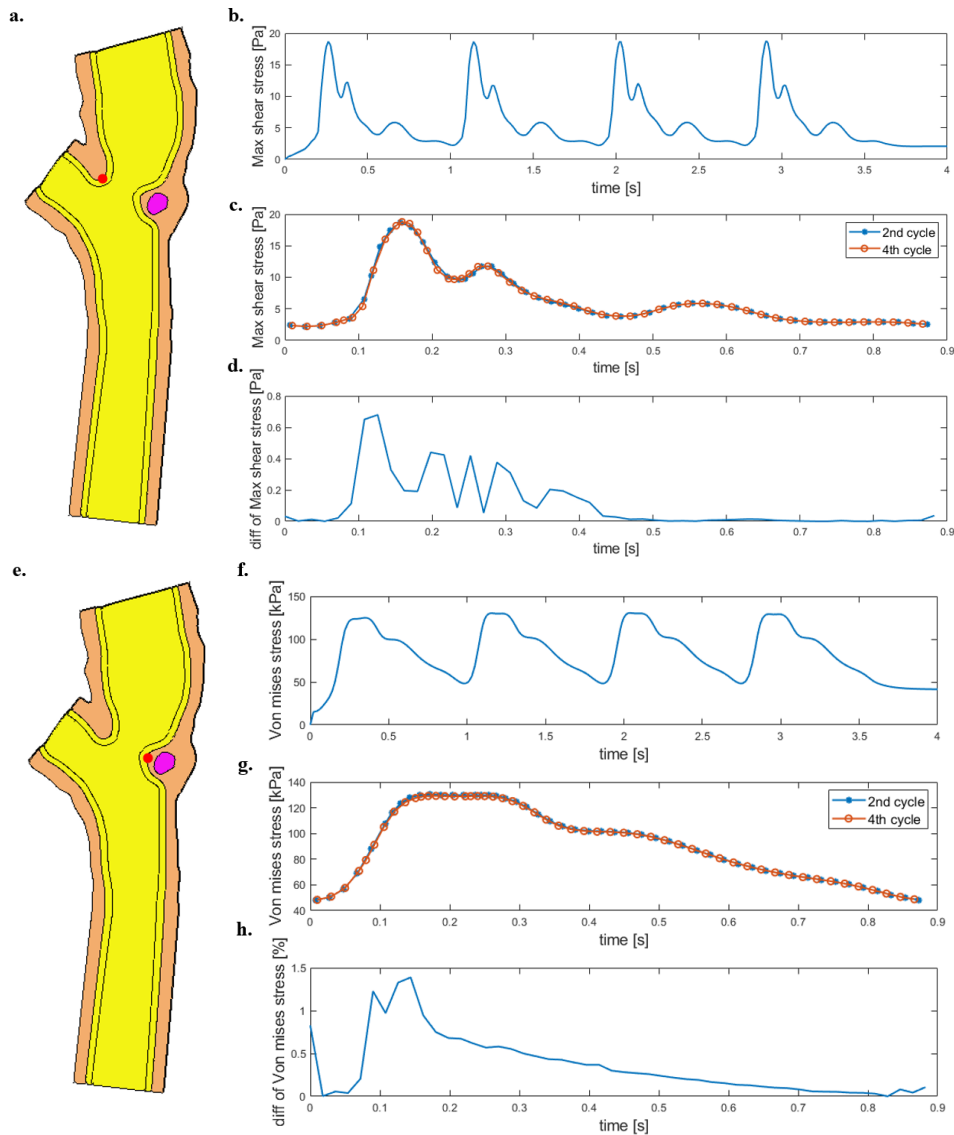


**Figure D.2: Comparison between the 2nd and 4th Cycles.** a. Selection of a bifurcation point marked in red to obtain shear stress results. b. Maximum fluid shear stress. c. Difference in shear stress between the 2nd and 4th cycles. e. Selection of a point on the plaque cap marked in red to obtain von Mises stress results. f. von Mises stress. g. Difference in von Mises stress between the 2nd and 4th cycles.

# E

## Results

### E.1. Case 1R

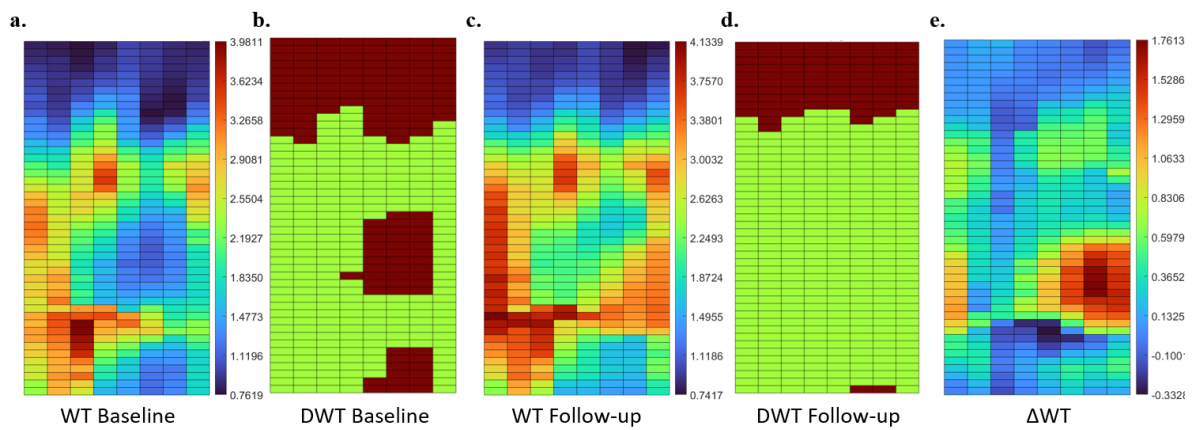


**Figure E.1: 2D map plot of WT for case 1R.** a. WT at baseline. b. DWT at baseline. c. WT at follow-up. d. DTW at follow-up. e. Difference of WT between baseline and follow-up. (WT: wall thickness; DWT: diseased wall thickness)

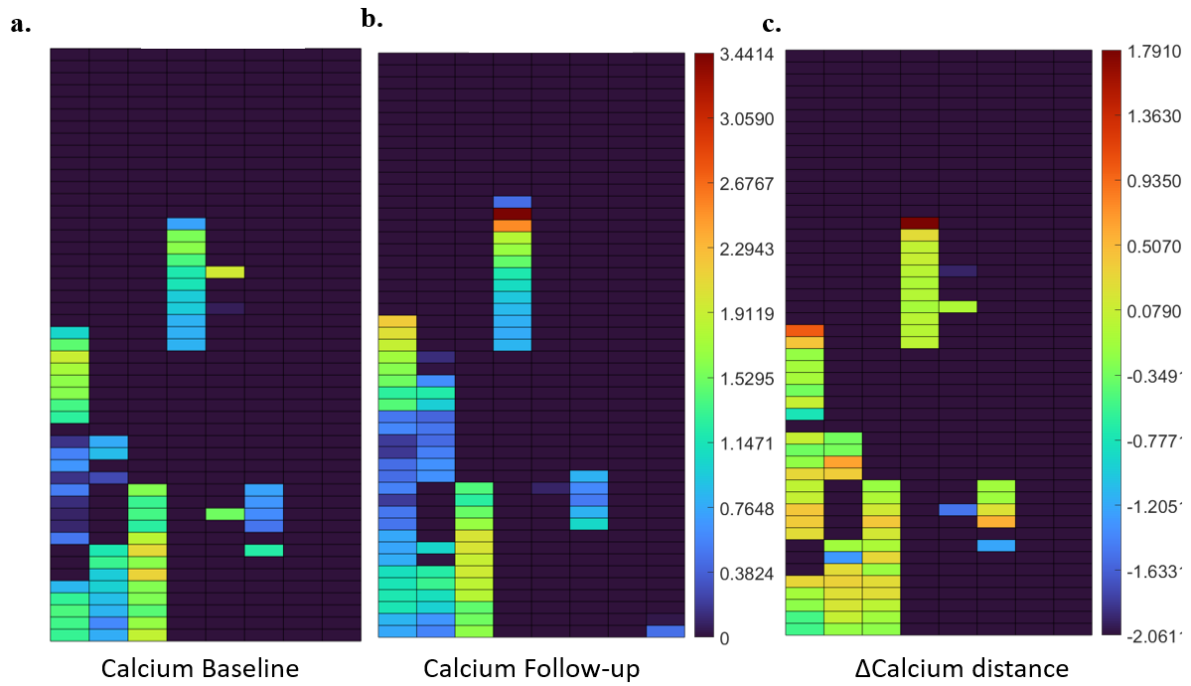


**Figure E.2: 2D map plot of calcium distance for case 1R.** a. Calcium distance at baseline. b. Calcium distance at follow-up. c. Difference of calcium distance between baseline and follow-up. Only the sectors with calcium detected were presented. a and b shared the same colormap.

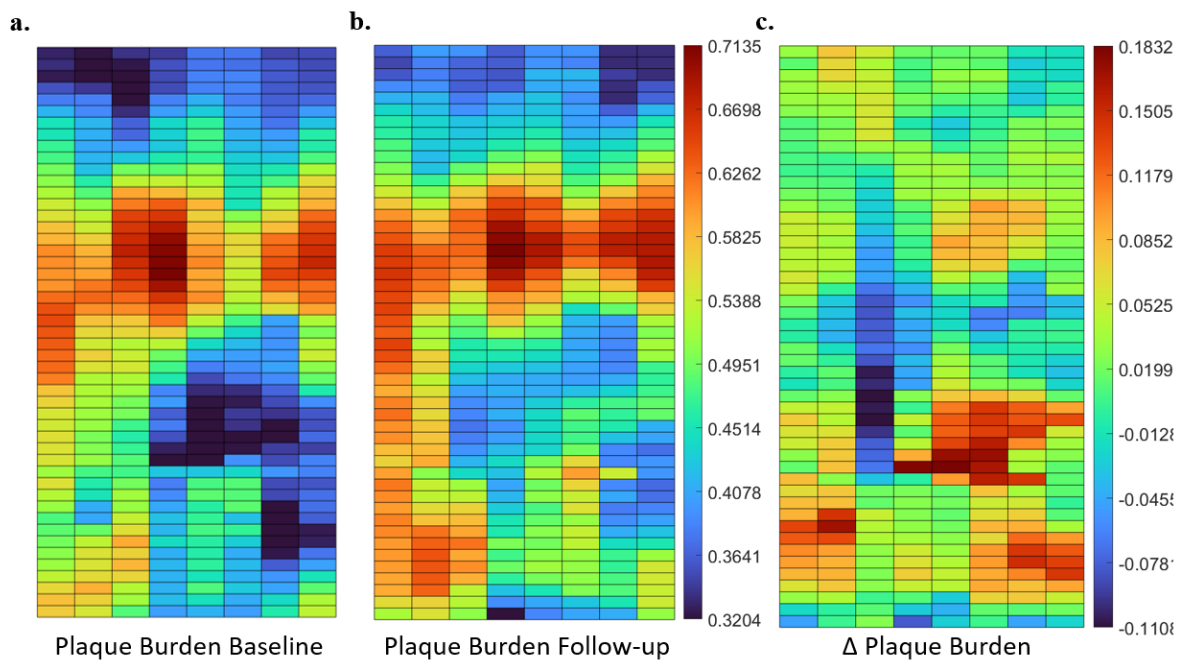


**Figure E.3: 2D map plot of plaque burden for case 1R.** a. Plaque burden at baseline. b. Plaque burden at follow-up. c. Difference of plaque burden between baseline and follow-up. a and b shared the same colormap.

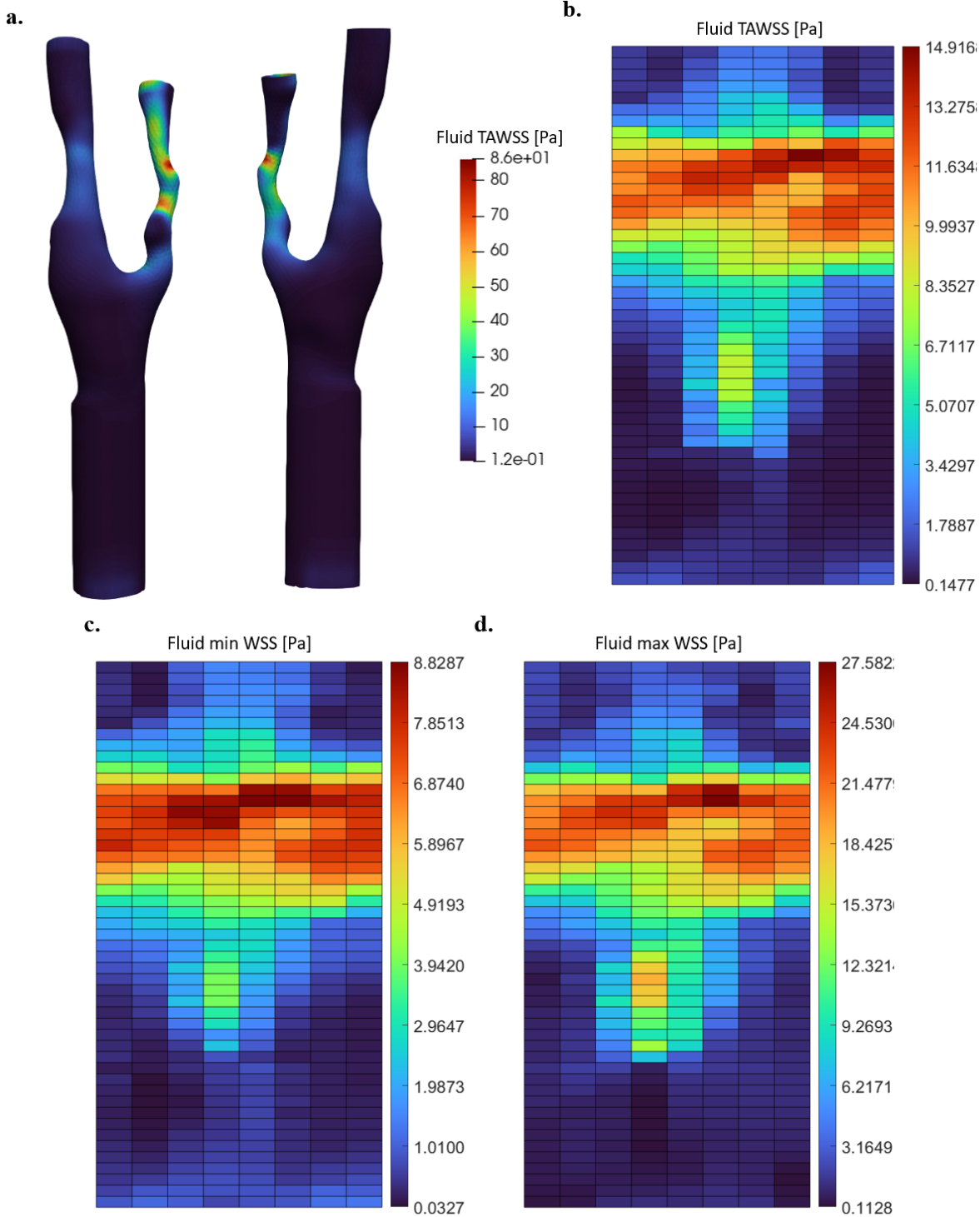


**Figure E.4: Fluid wall shear stress (WSS) for case 1R.** a. Front view and back view of the stress distribution. b. 2D map of fluid time-average WSS. c. 2D map of min fluid WSS over a cycle. d. 2D map of max fluid WSS over a cycle.

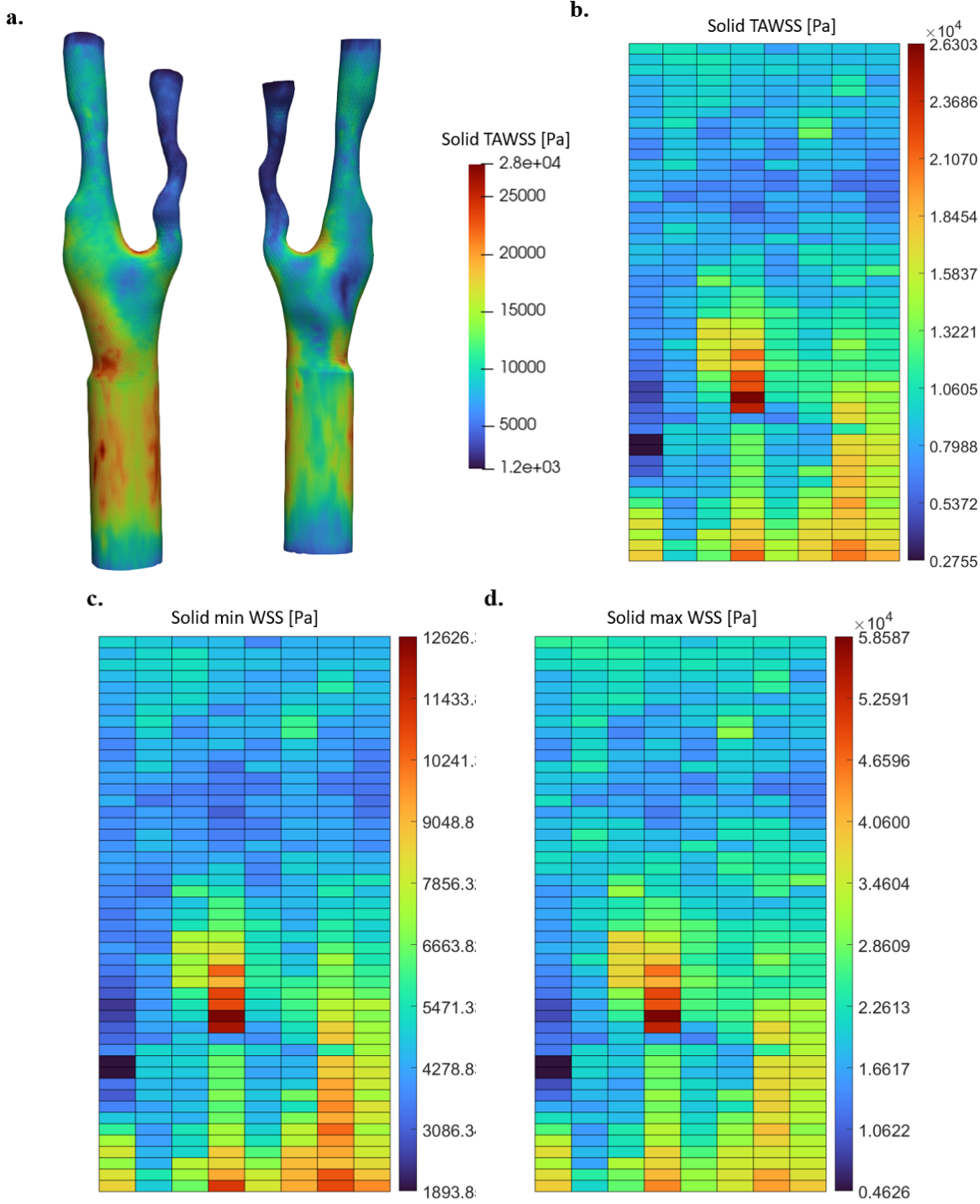


**Figure E.5: Solid wall shear stress (WSS) for case 1R.** a. Front view and back view of the stress distribution. b. 2D map of solid time-average WSS. c. 2D map of min solid WSS over a cycle. d. 2D map of max solid WSS over a cycle.

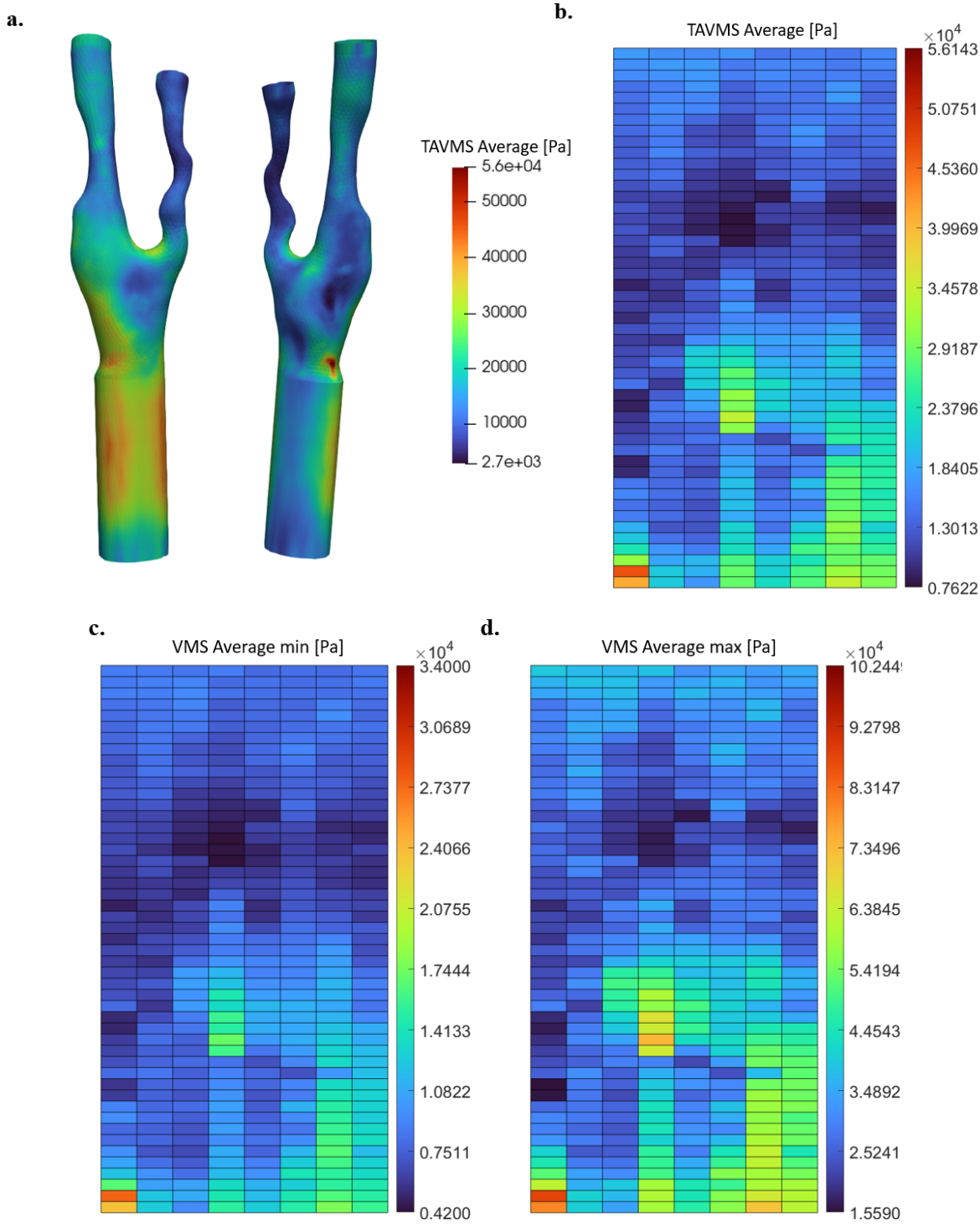


**Figure E.6: Average von Mises stress (VMS) for case 1R.** a. Front view and back view of the stress distribution. b. 2D map of average VMS. c. 2D map of min average VMS over a cycle. d. 2D map of max average VMS over a cycle.

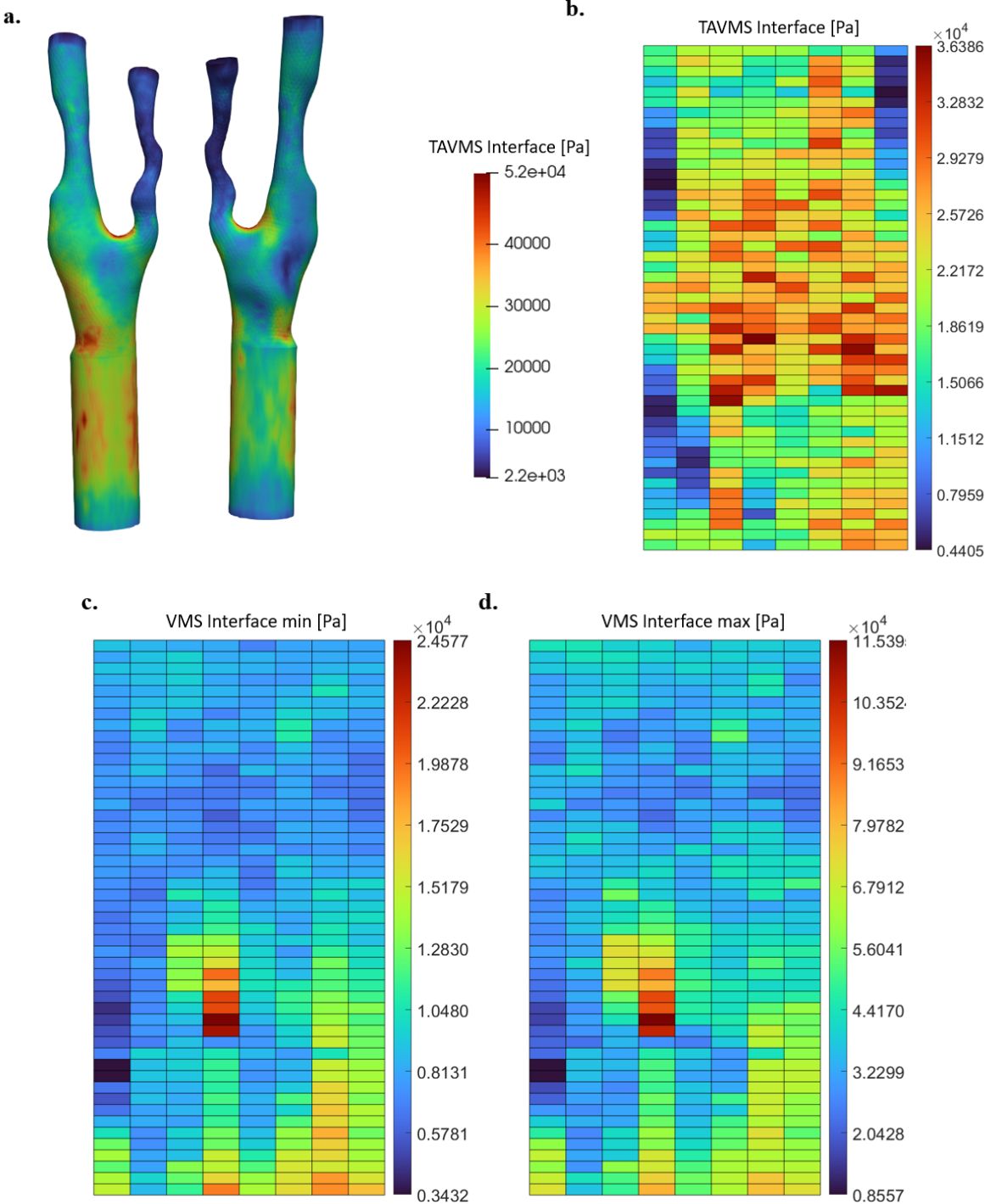


**Figure E.7: Interface von Mises stress (VMS) for case 1R.** a. Front view and back view of the stress distribution. b. 2D map of interface VMS. c. 2D map of min interface VMS over a cycle. d. 2D map of max interface VMS over a cycle.

## E.2. Case 2L

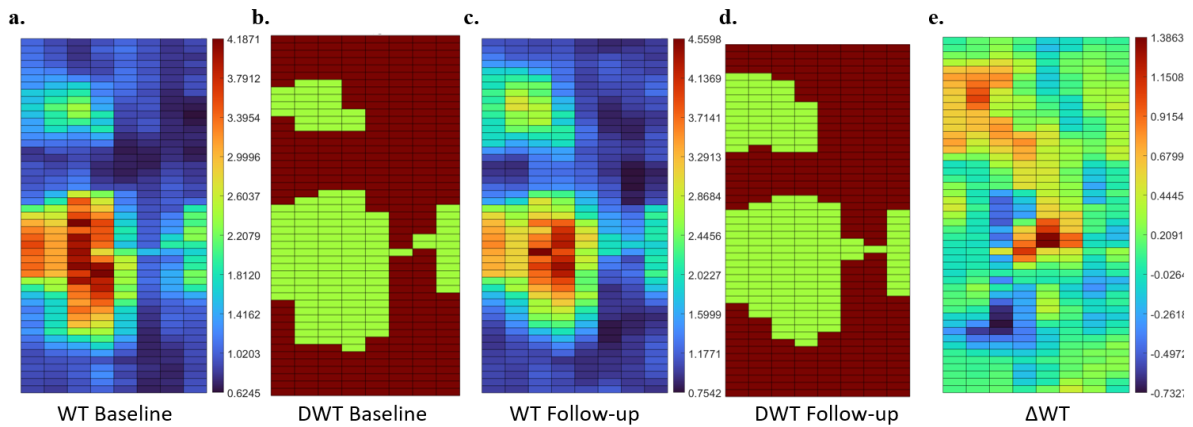


**Figure E.8: 2D map plot of WT for case 2L.** a. WT at baseline. b. DWT at baseline. c. WT at follow-up. d. DWT at follow-up. e. Difference of WT between baseline and follow-up. (WT: wall thickness; DWT: diseased wall thickness)

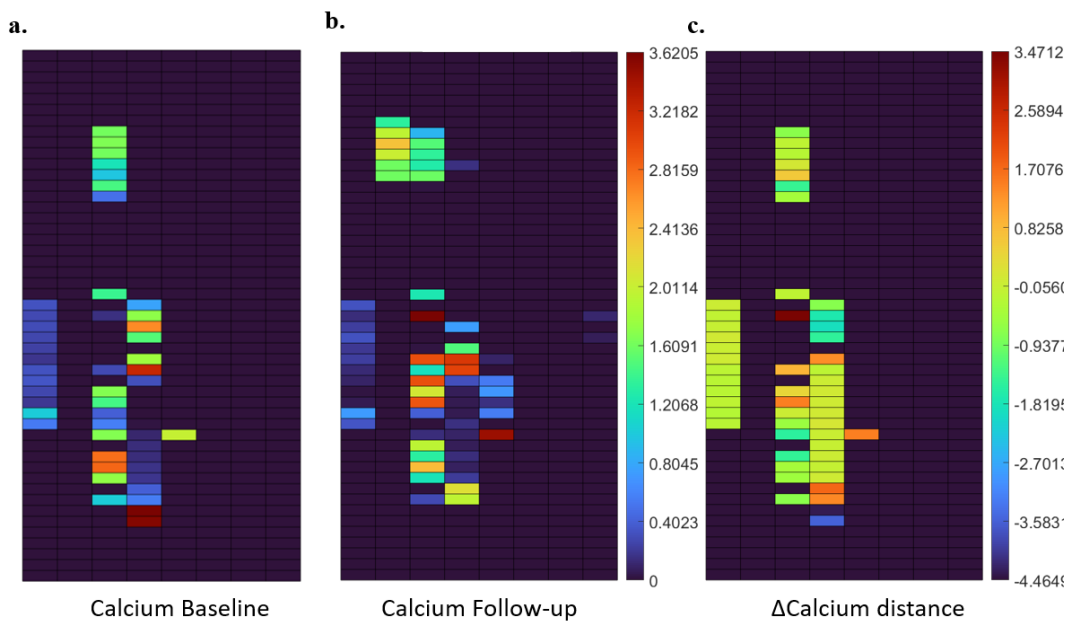


**Figure E.9: 2D map plot of calcium distance for case 2L.** a. Calcium distance at baseline. b. Calcium distance at follow-up. c. Difference of calcium distance between baseline and follow-up. Only the sectors with calcium detected were presented. a and b shared the same colormap.

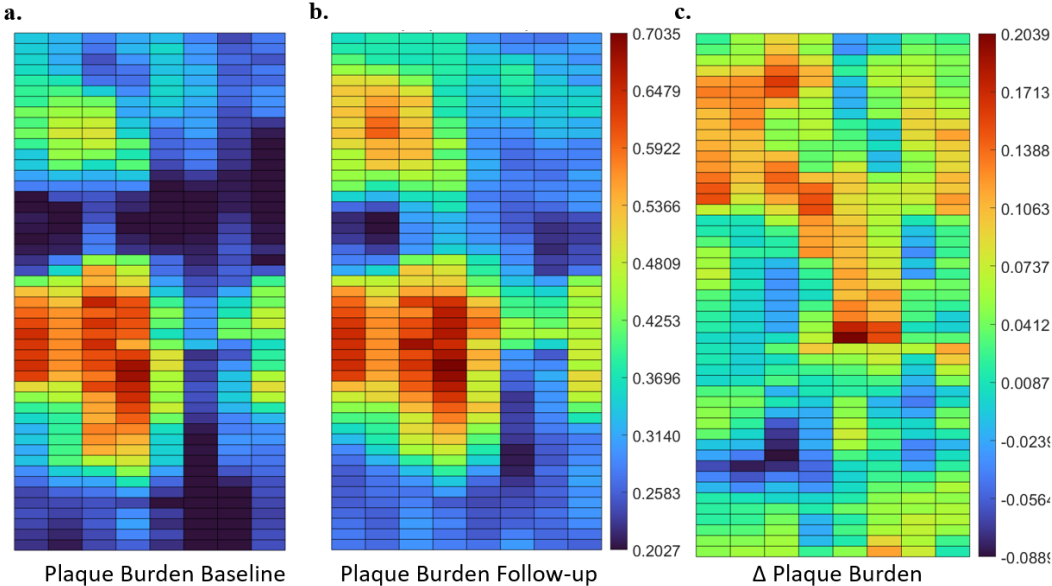


**Figure E.10: 2D map plot of plaque burden for case 2L.** a. Plaque burden at baseline. b. Plaque burden at follow-up. c. Difference of plaque burden between baseline and follow-up. a and b shared the same colormap.

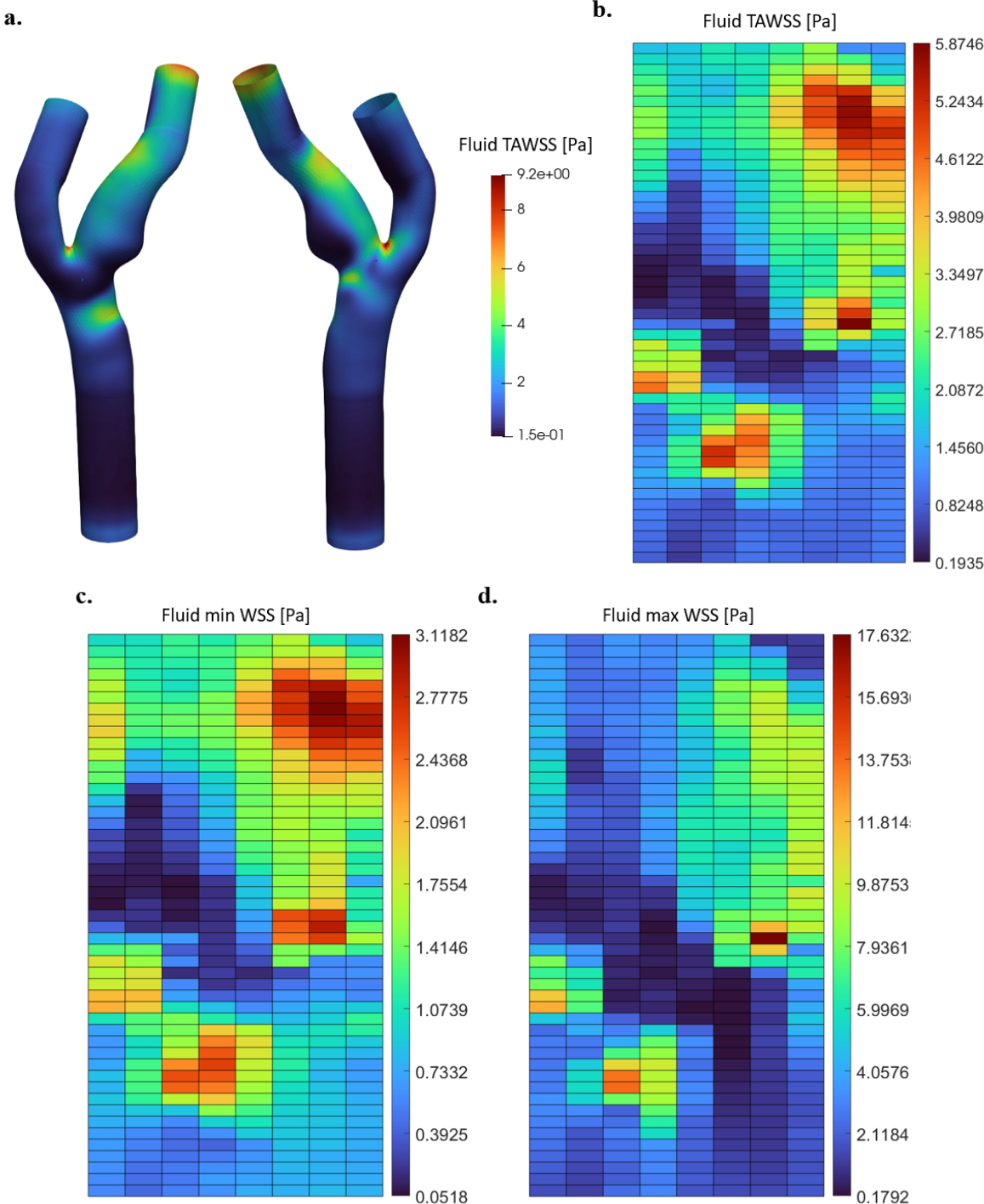


**Figure E.11: Fluid wall shear stress (WSS) for case 2L.** a. Front view and back view of the stress distribution. b. 2D map of fluid time-average WSS. c. 2D map of min fluid WSS over a cycle. d. 2D map of max fluid WSS over a cycle.

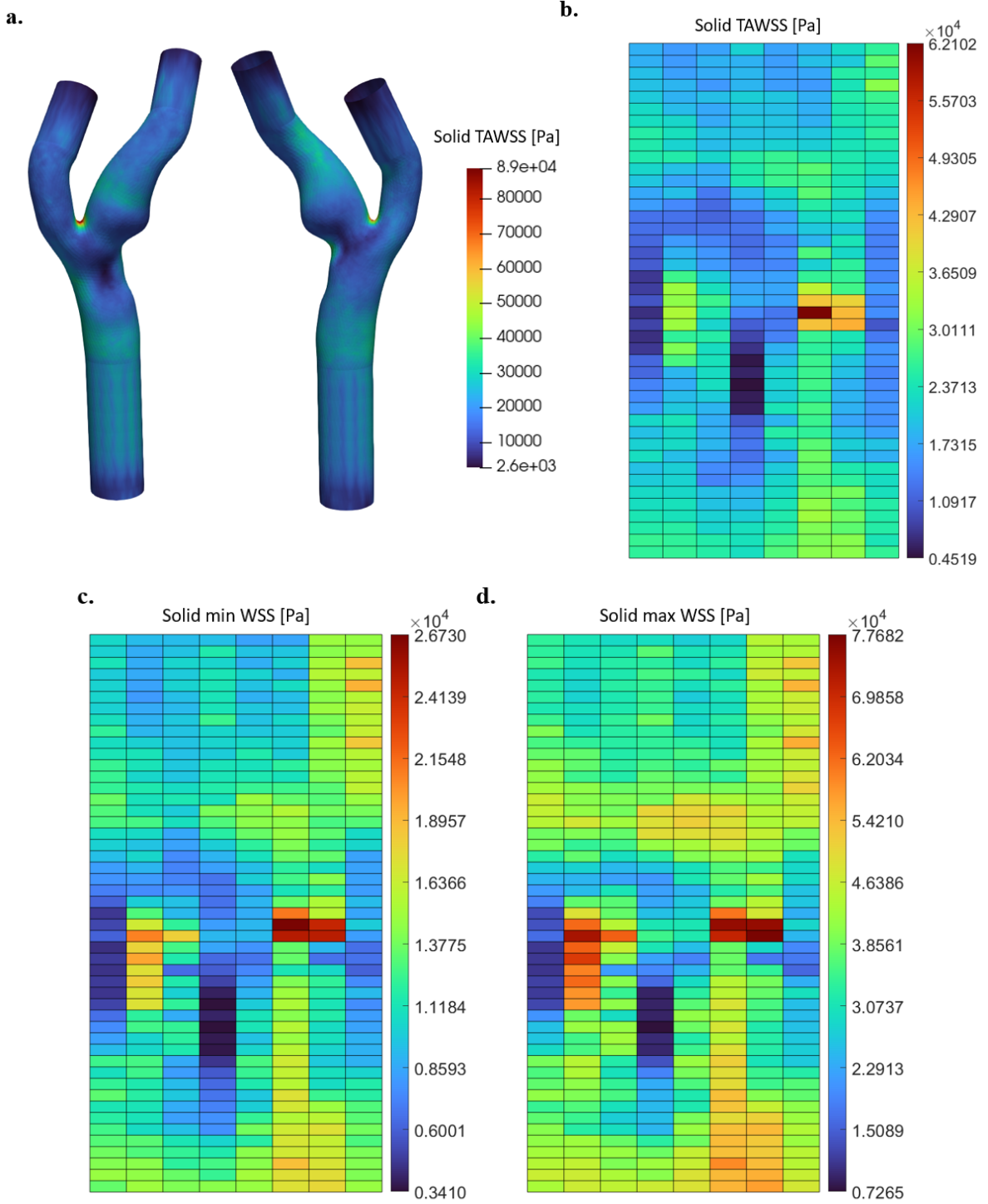


**Figure E.12: Solid wall shear stress (WSS) for case 2L.** a. Front view and back view of the stress distribution. b. 2D map of solid time-average WSS. c. 2D map of min solid WSS over a cycle. d. 2D map of max solid WSS over a cycle.

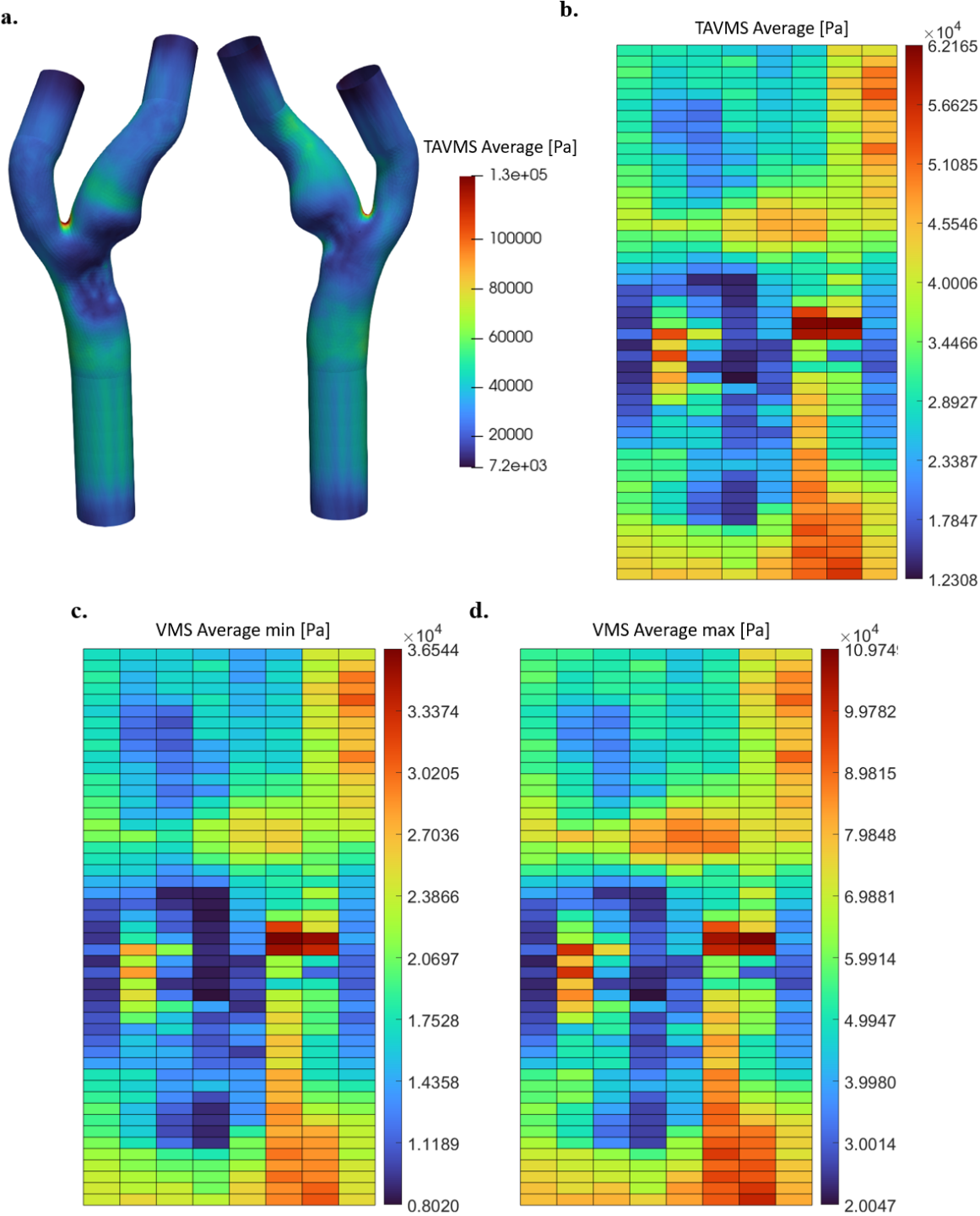


**Figure E.13: Average von Mises stress (VMS) for case 2L.** a. Front view and back view of the stress distribution. b. 2D map of average VMS. c. 2D map of min average VMS over a cycle. d. 2D map of max average VMS over a cycle.

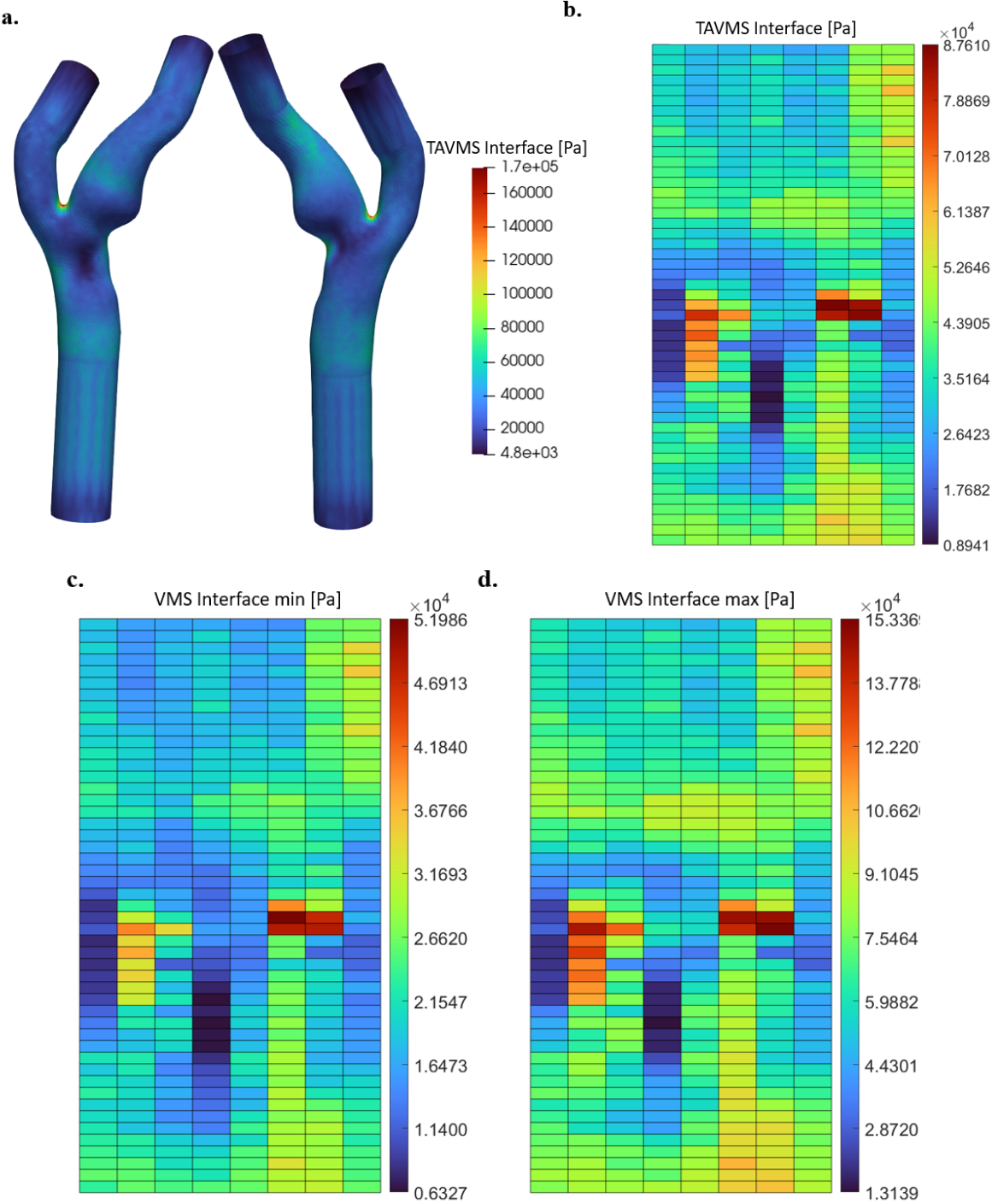


**Figure E.14: Interface von Mises stress (VMS) for case 2L.** a. Front view and back view of the stress distribution. b. 2D map of interface VMS. c. 2D map of min interface VMS over a cycle. d. 2D map of max interface VMS over a cycle.

## E.3. Case 2R

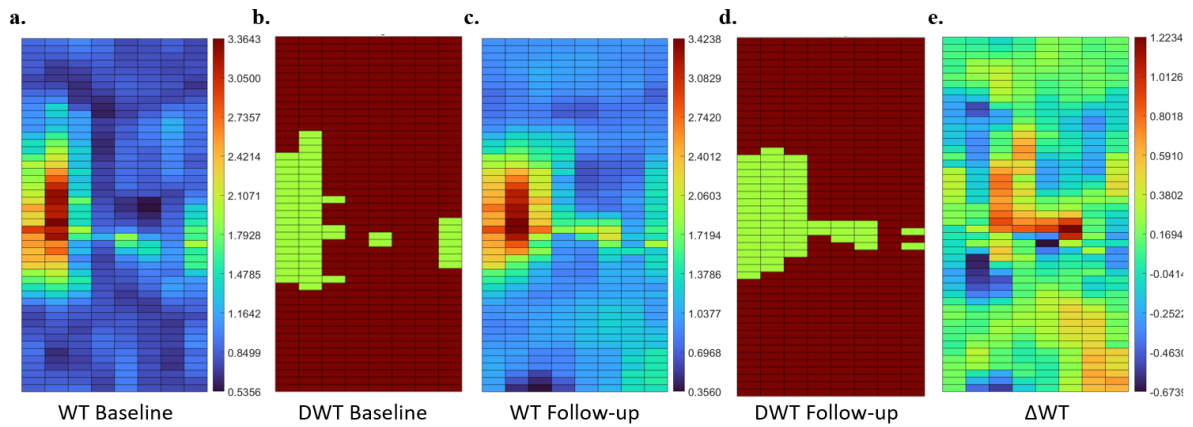


**Figure E.15: 2D map plot of WT for case 2R.** a. WT at baseline. b. DWT at baseline. c. WT at follow-up. d. DWT at follow-up. e. Difference of WT between baseline and follow-up. (WT: wall thickness; DWT: diseased wall thickness)

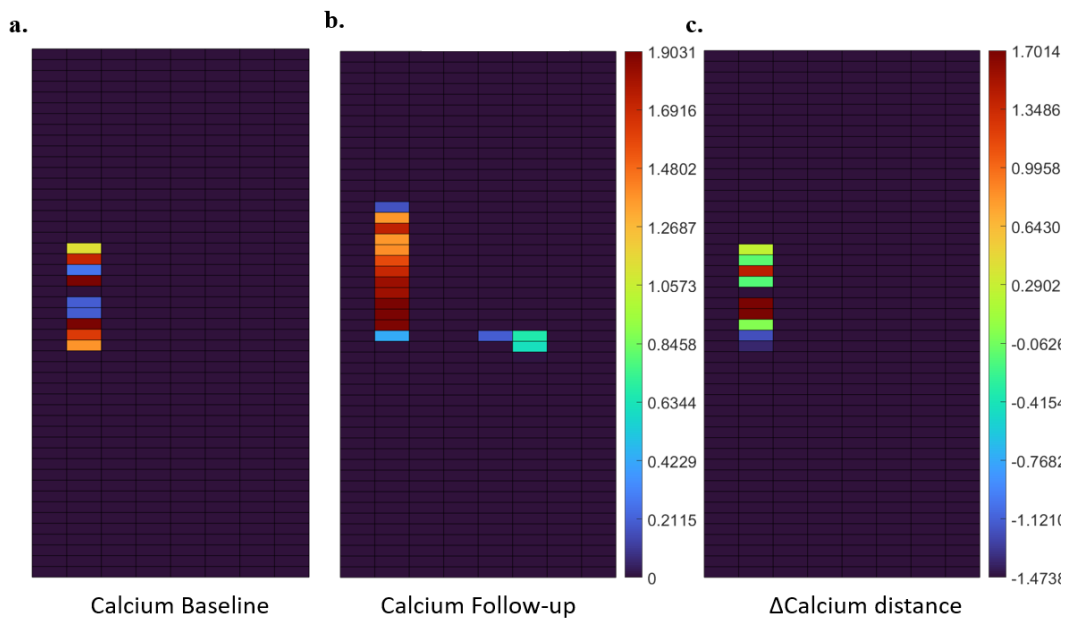


**Figure E.16: 2D map plot of calcium distance for case 2R.** a. Calcium distance at baseline. b. Calcium distance at follow-up. c. Difference of calcium distance between baseline and follow-up. Only the sectors with calcium detected were presented. a and b shared the same colormap.

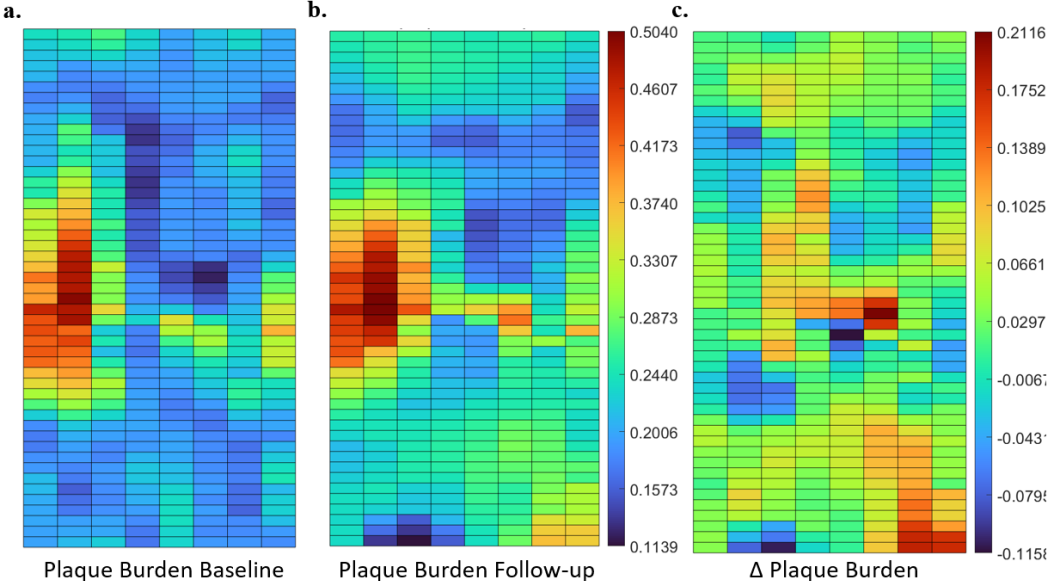


**Figure E.17: 2D map plot of plaque burden for case 2R.** a. Plaque burden at baseline. b. Plaque burden at follow-up. c. Difference of plaque burden between baseline and follow-up. a and b shared the same colormap.

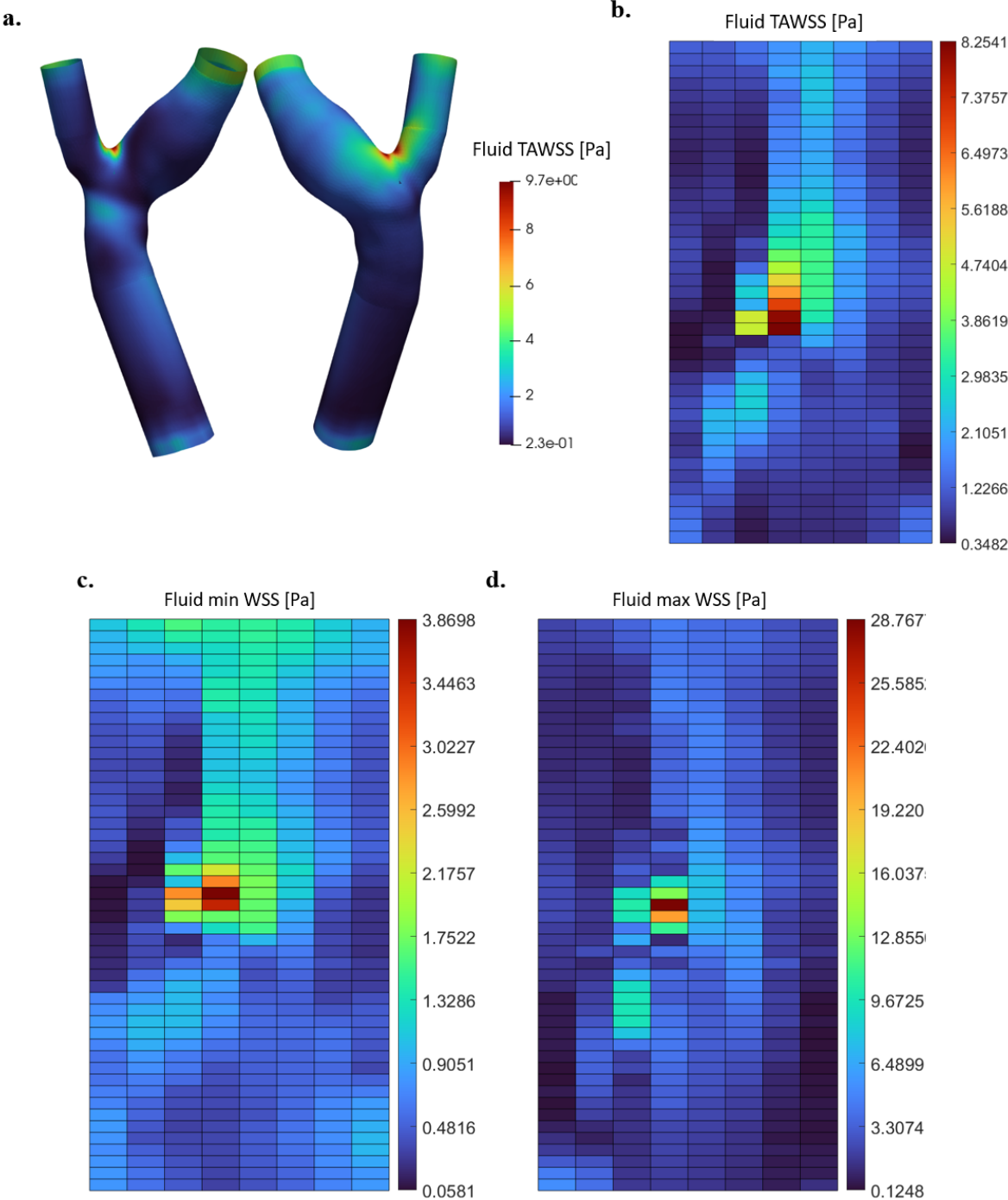


**Figure E.18: Fluid wall shear stress (WSS) for case 2R.** a. Front view and back view of the stress distribution. b. 2D map of fluid time-average WSS. c. 2D map of min fluid WSS over a cycle. d. 2D map of max fluid WSS over a cycle.

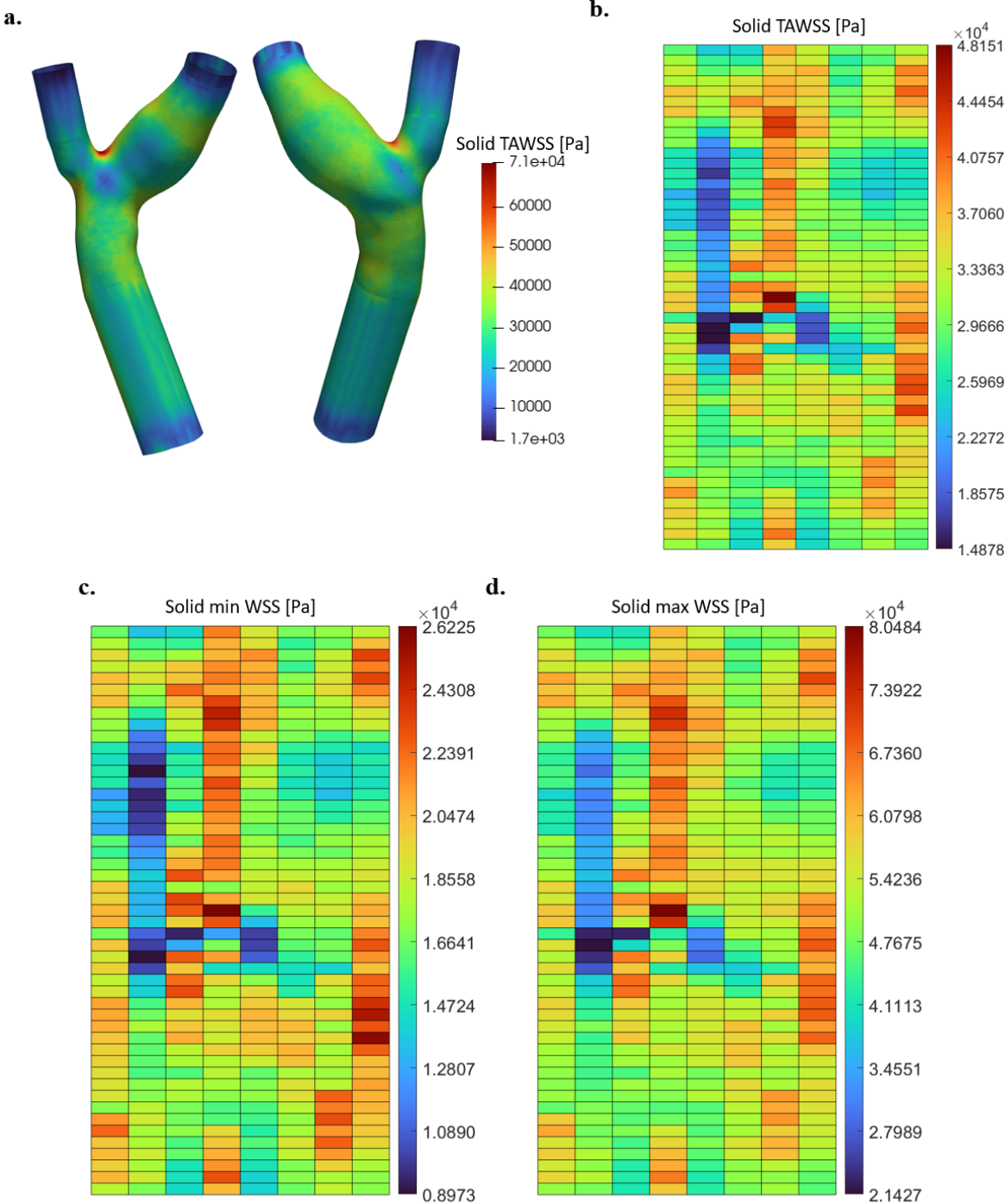


**Figure E.19: Solid wall shear stress (WSS) for case 2R.** a. Front view and back view of the stress distribution. b. 2D map of solid time-average WSS. c. 2D map of min solid WSS over a cycle. d. 2D map of max solid WSS over a cycle.

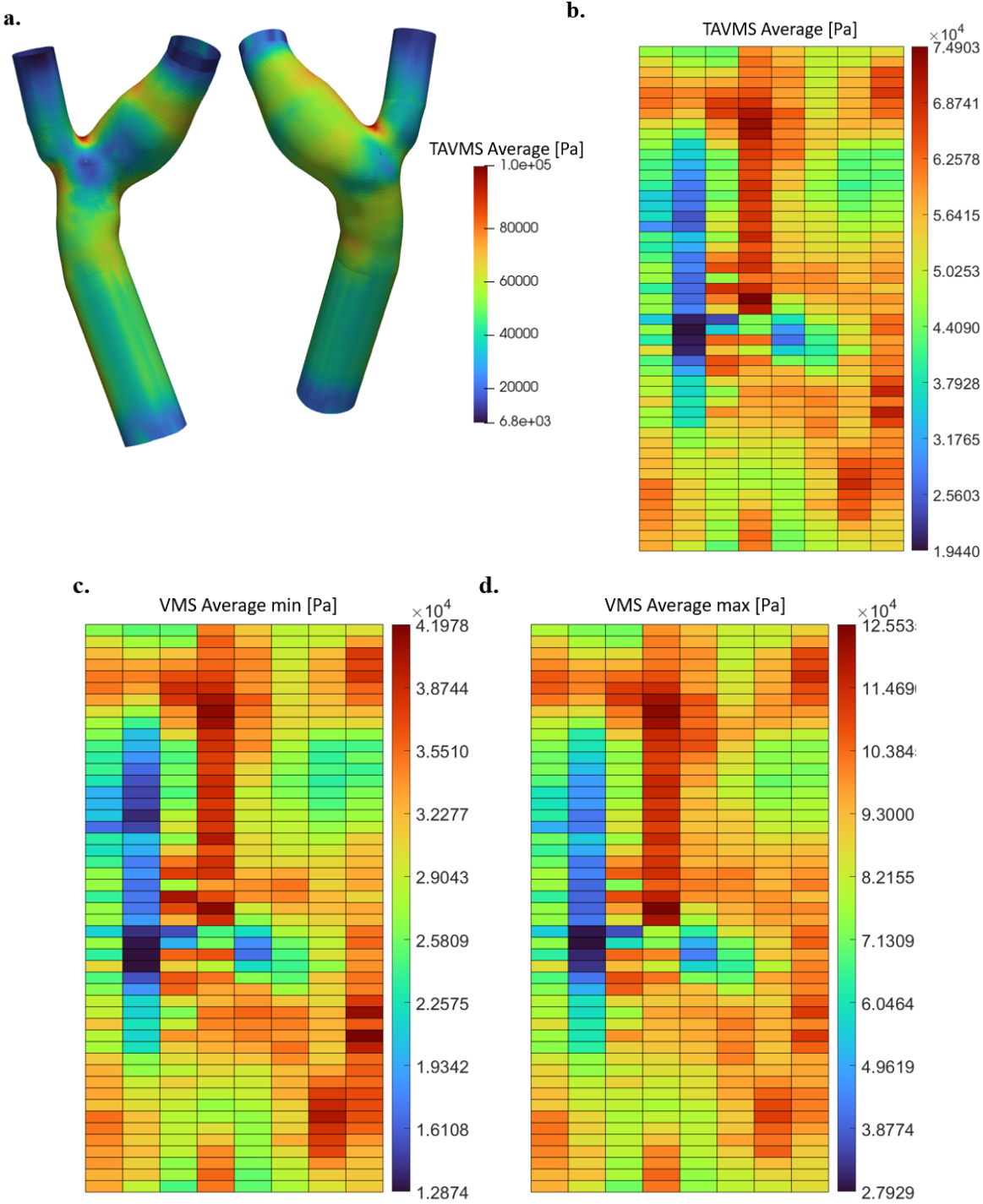


**Figure E.20: Average von Mises stress (VMS) for case 2R.** a. Front view and back view of the stress distribution. b. 2D map of average VMS. c. 2D map of min average VMS over a cycle. d. 2D map of max average VMS over a cycle.

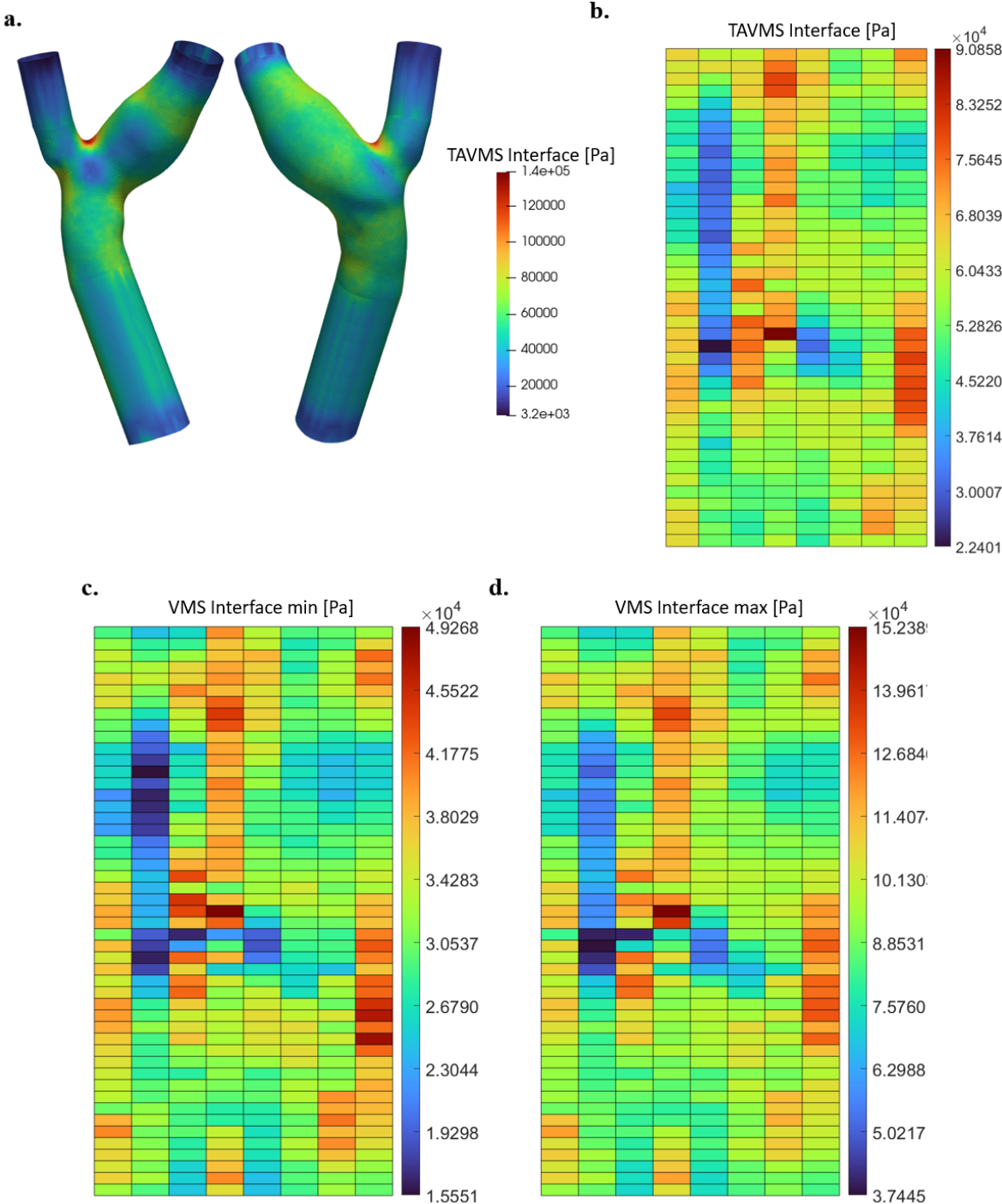


**Figure E.21: Interface von Mises stress (VMS) for case 2R.** a. Front view and back view of the stress distribution. b. 2D map of interface VMS. c. 2D map of min interface VMS over a cycle. d. 2D map of max interface VMS over a cycle.

## E.4. Case 3L

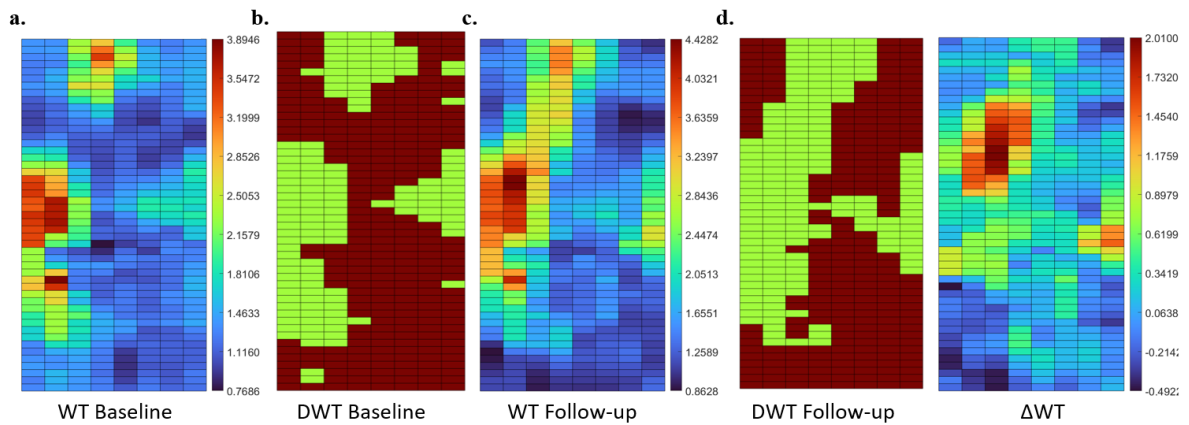


**Figure E.22: 2D map plot of WT for case 3L.** a. WT at baseline. b. DWT at baseline. c. WT at follow-up. d. DWT at follow-up. e. Difference of WT between baseline and follow-up. (WT: wall thickness; DWT: diseased wall thickness)

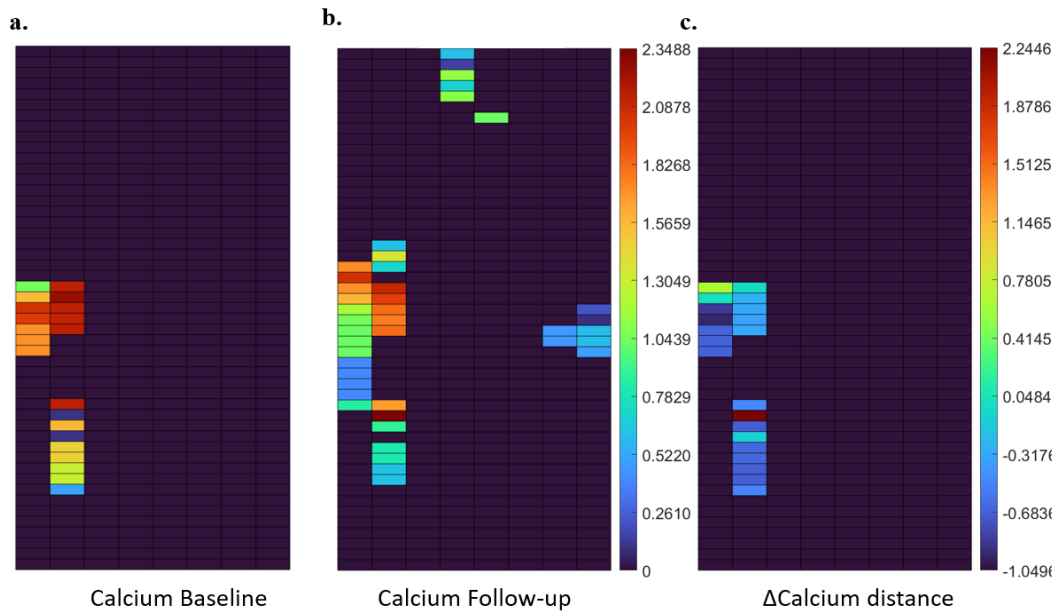


**Figure E.23: 2D map plot of calcium distance for case 3L.** a. Calcium distance at baseline. b. Calcium distance at follow-up. c. Difference of calcium distance between baseline and follow-up. Only the sectors with calcium detected were presented. a and b shared the same colormap.

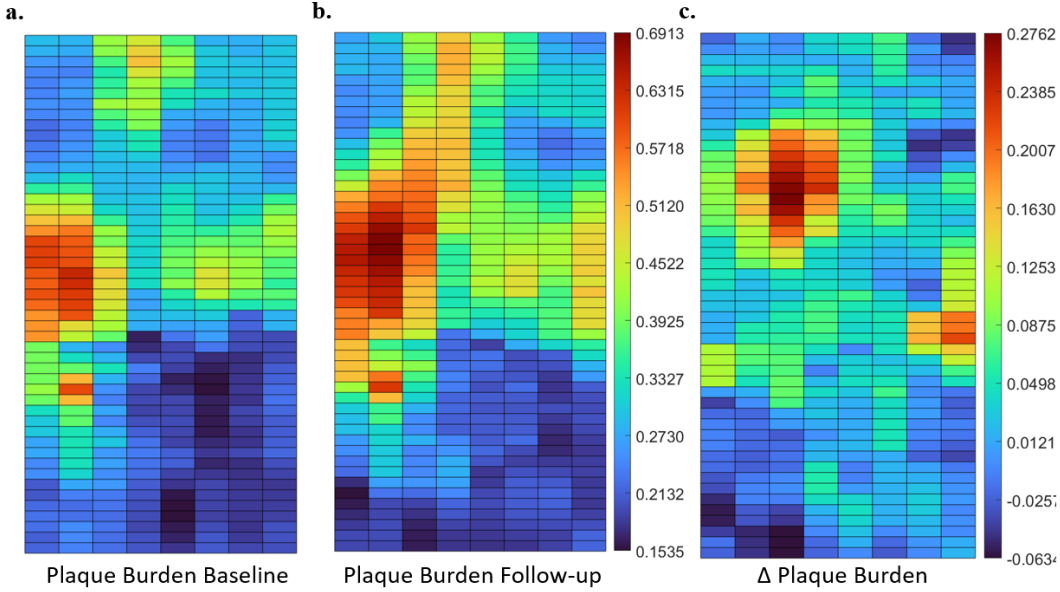


**Figure E.24: 2D map plot of plaque burden for case 3L.** a. Plaque burden at baseline. b. Plaque burden at follow-up. c. Difference of plaque burden between baseline and follow-up. a and b shared the same colormap.

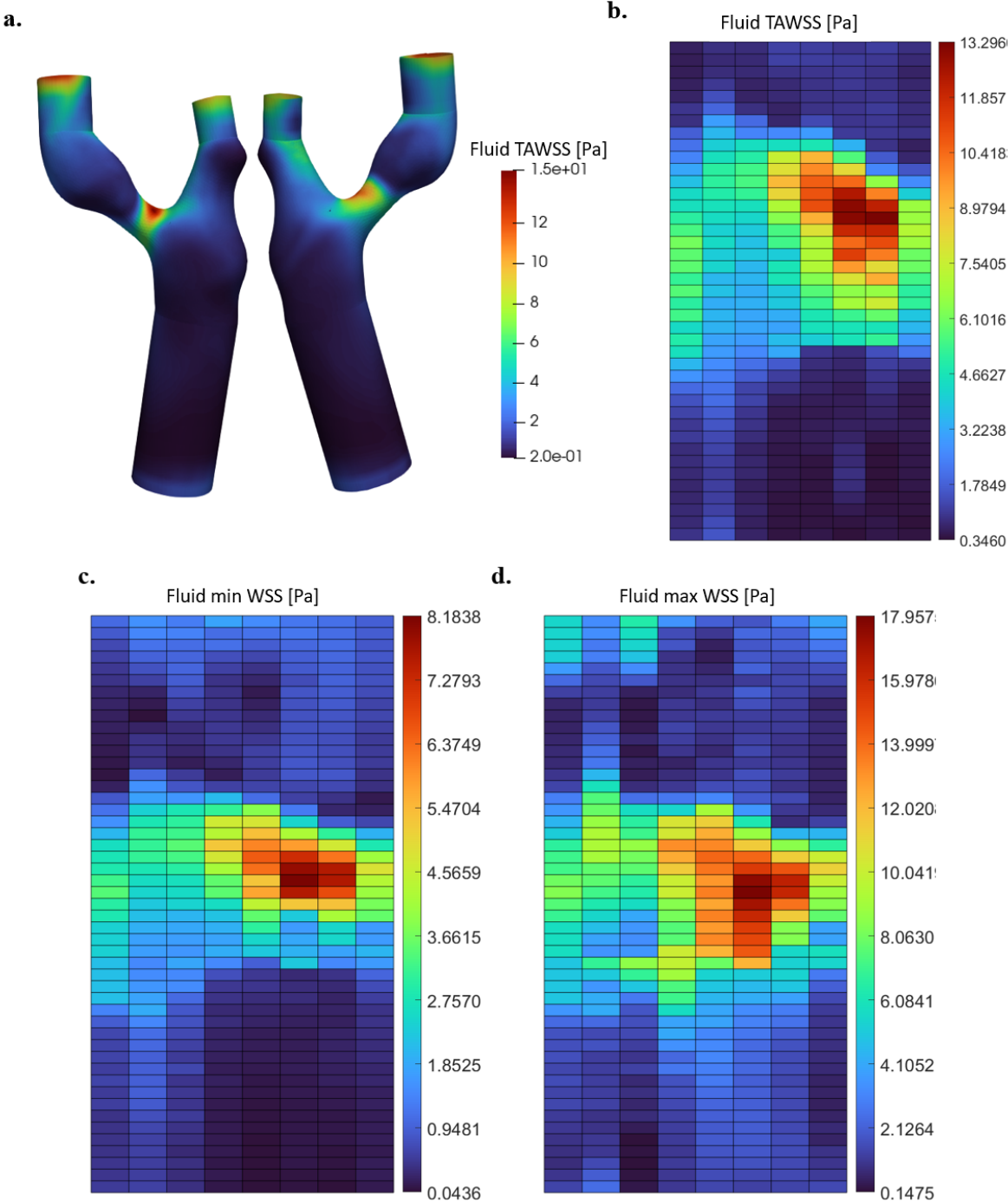


**Figure E.25: Fluid wall shear stress (WSS) for case 3L.** a. Front view and back view of the stress distribution. b. 2D map of fluid time-average WSS. c. 2D map of min fluid WSS over a cycle. d. 2D map of max fluid WSS over a cycle.

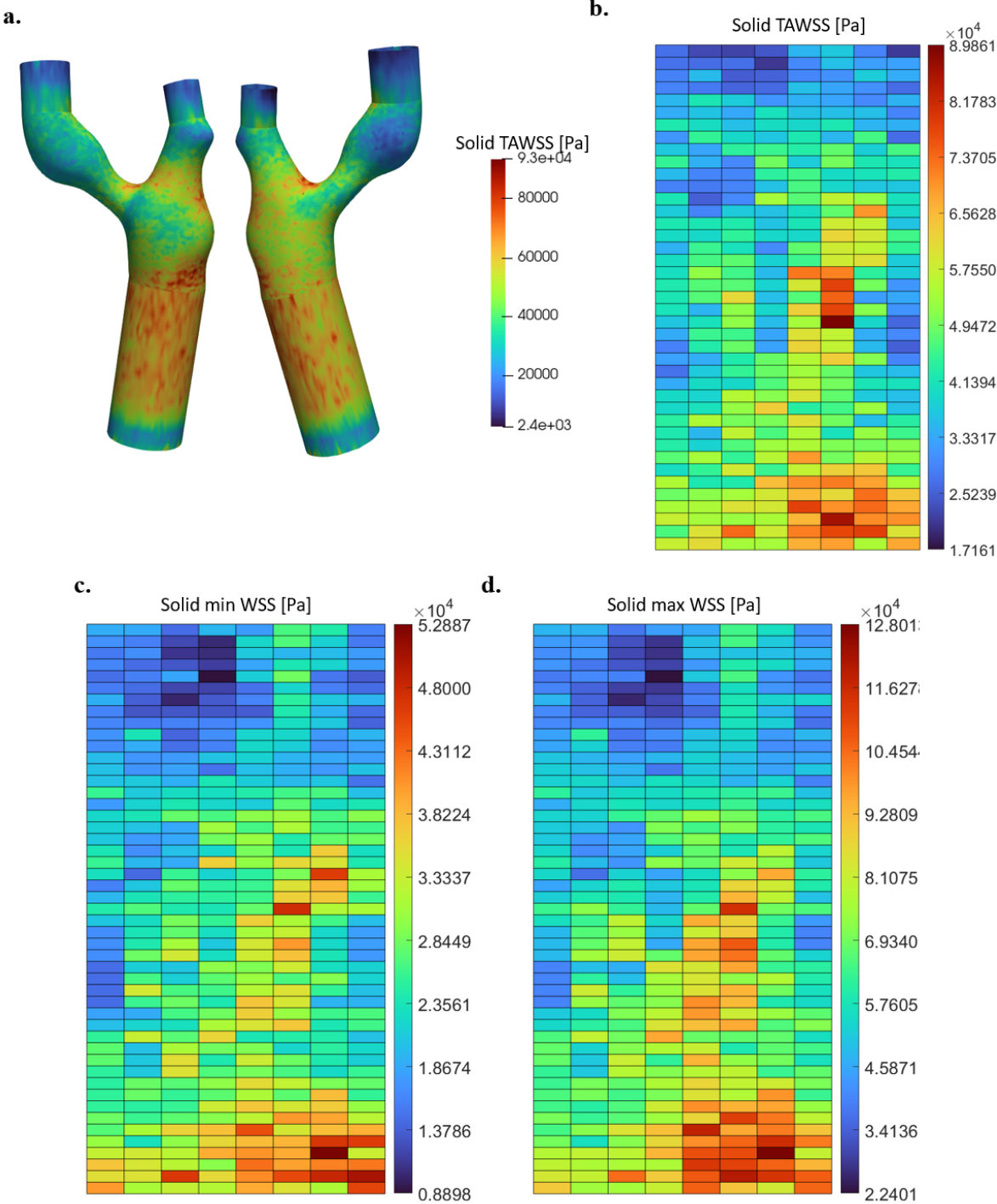


**Figure E.26: Solid wall shear stress (WSS) for case 3L.** a. Front view and back view of the stress distribution. b. 2D map of solid time-average WSS. c. 2D map of min solid WSS over a cycle. d. 2D map of max solid WSS over a cycle.

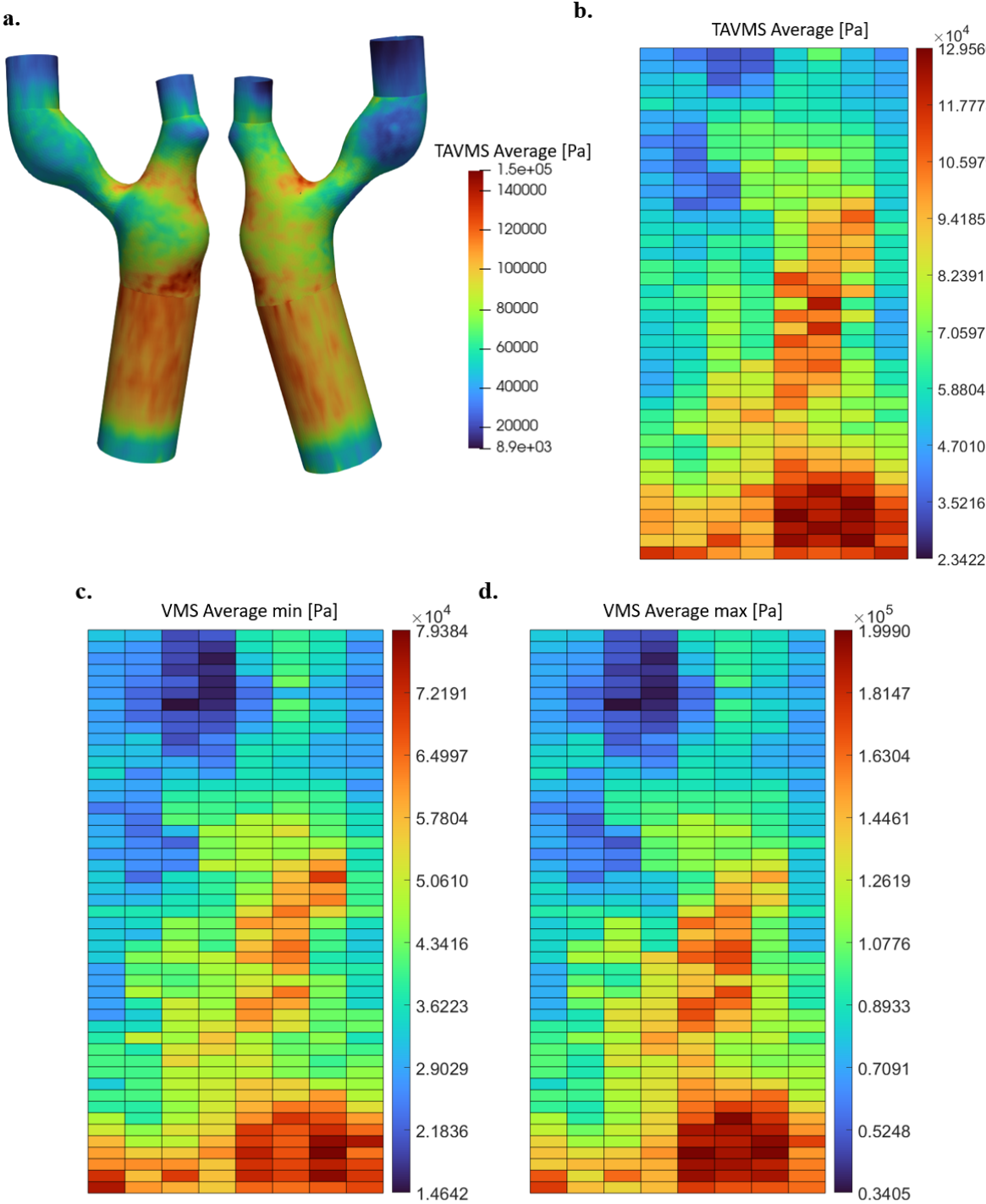


**Figure E.27: Average von Mises stress (VMS) for case 3L.** a. Front view and back view of the stress distribution. b. 2D map of average VMS. c. 2D map of min average VMS over a cycle. d. 2D map of max average VMS over a cycle.

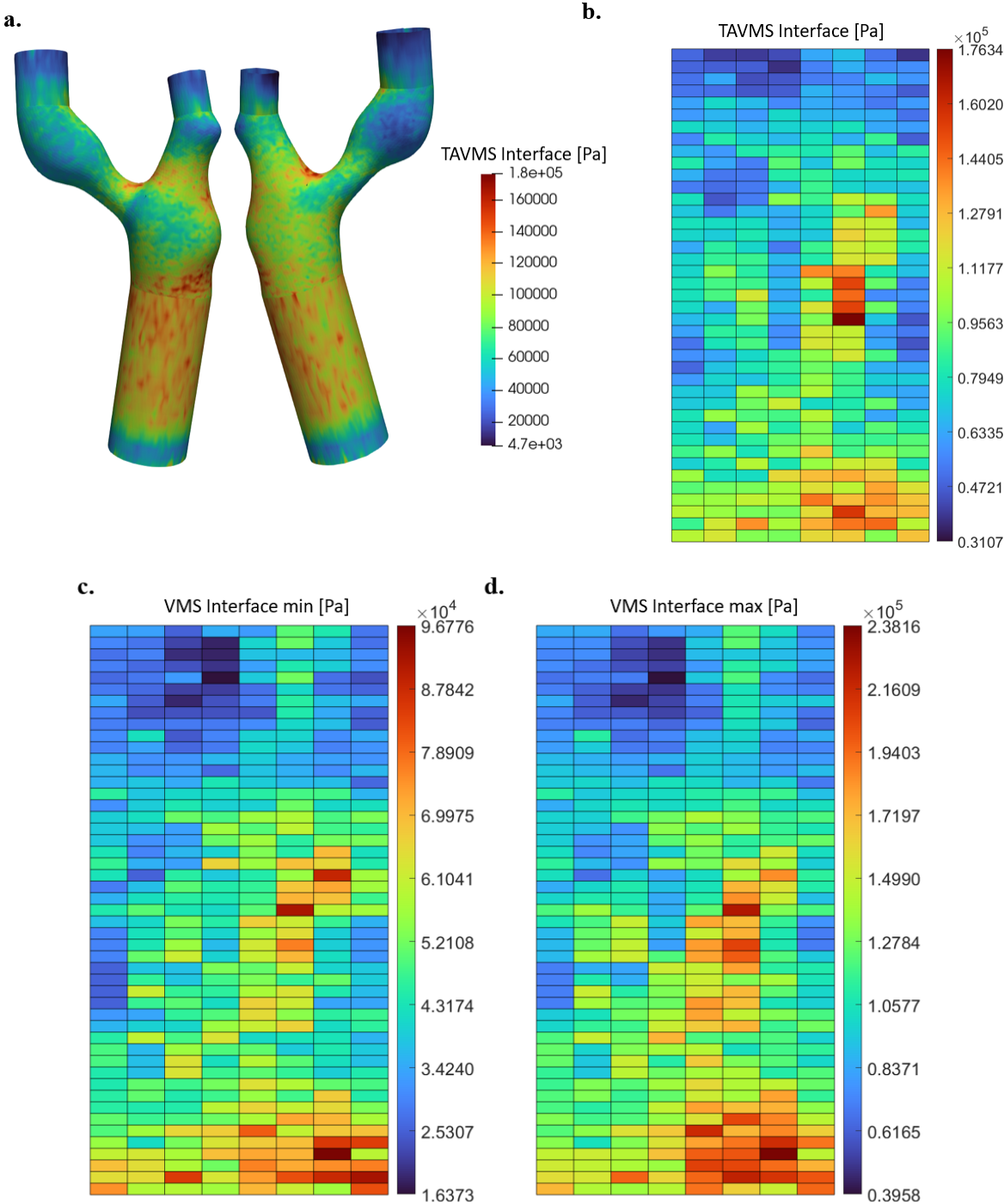


**Figure E.28: Interface von Mises stress (VMS) for case 3L.** a. Front view and back view of the stress distribution. b. 2D map of interface VMS. c. 2D map of min interface VMS over a cycle. d. 2D map of max interface VMS over a cycle.

## E.5. Case 3R

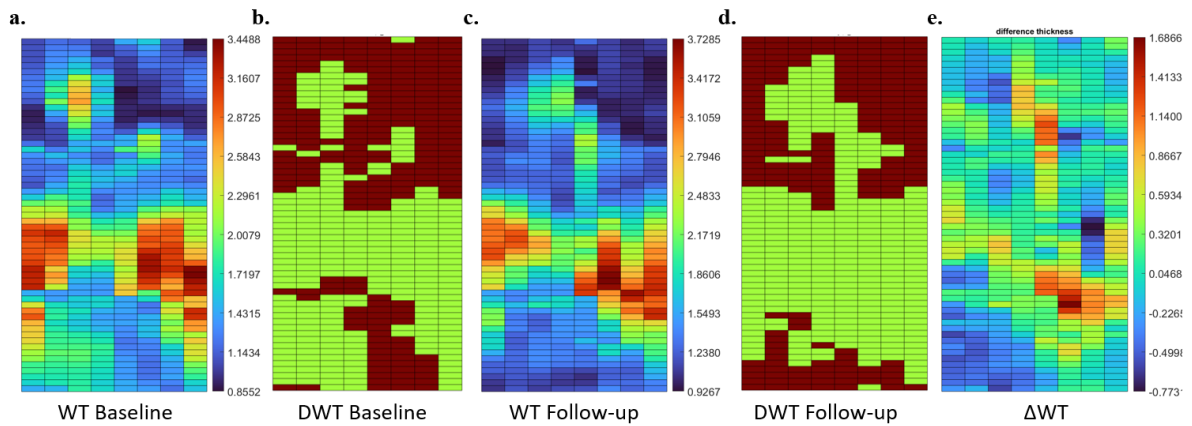


**Figure E.29: 2D map plot of WT for case 3R.** a. WT at baseline. b. DWT at baseline. c. WT at follow-up. d. DWT at follow-up. e. Difference of WT between baseline and follow-up. (WT: wall thickness; DWT: diseased wall thickness)

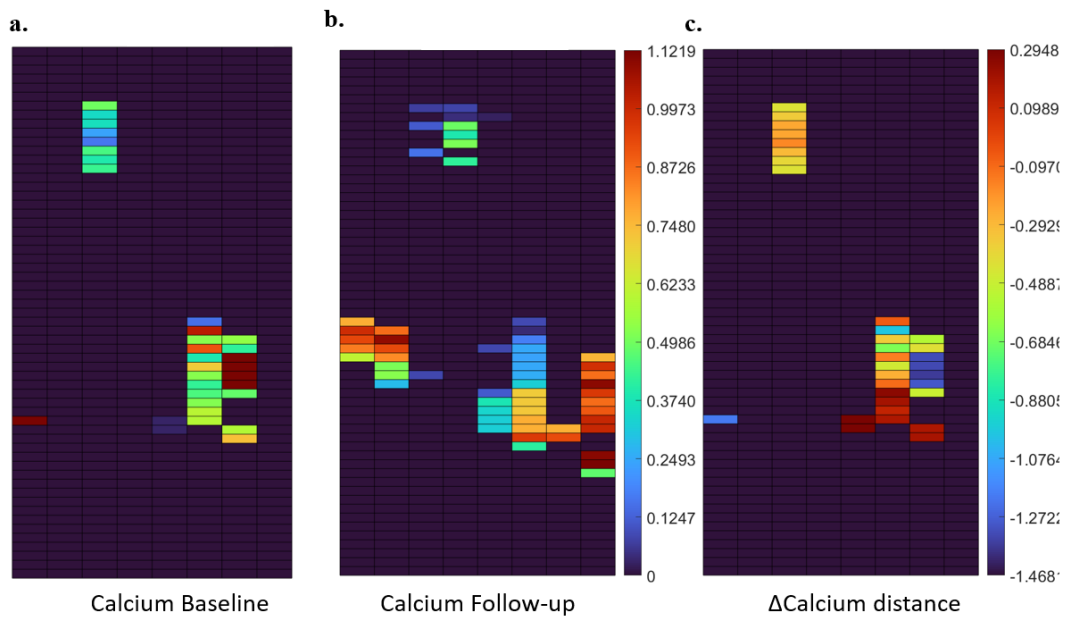


**Figure E.30: 2D map plot of calcium distance for case 3R.** a. Calcium distance at baseline. b. Calcium distance at follow-up. c. Difference of calcium distance between baseline and follow-up. Only the sectors with calcium detected were presented. a and b shared the same colormap.

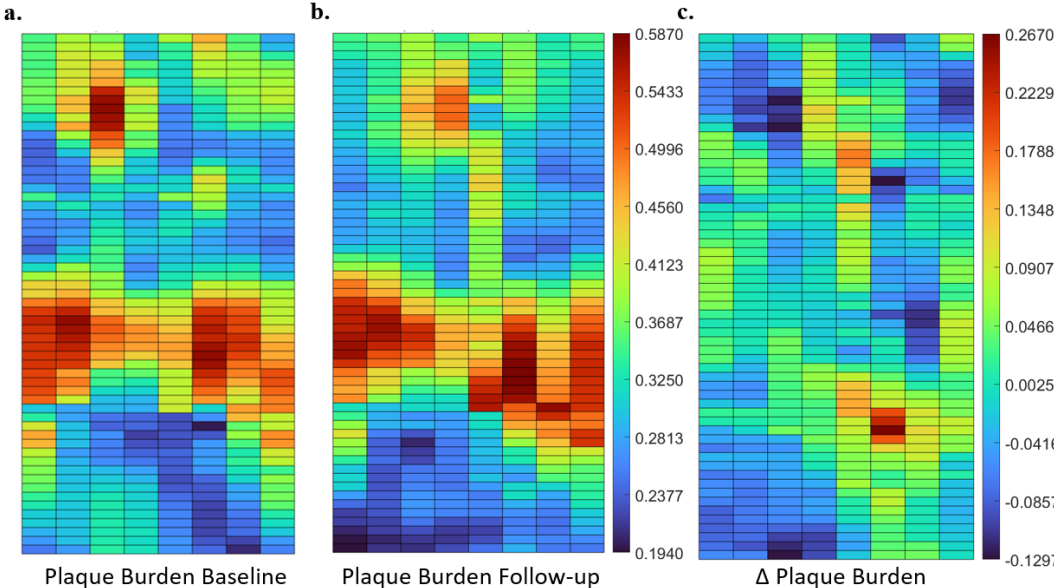


**Figure E.31: 2D map plot of plaque burden for case 3R.** a. Plaque burden at baseline. b. Plaque burden at follow-up. c. Difference of plaque burden between baseline and follow-up. a and b shared the same colormap.

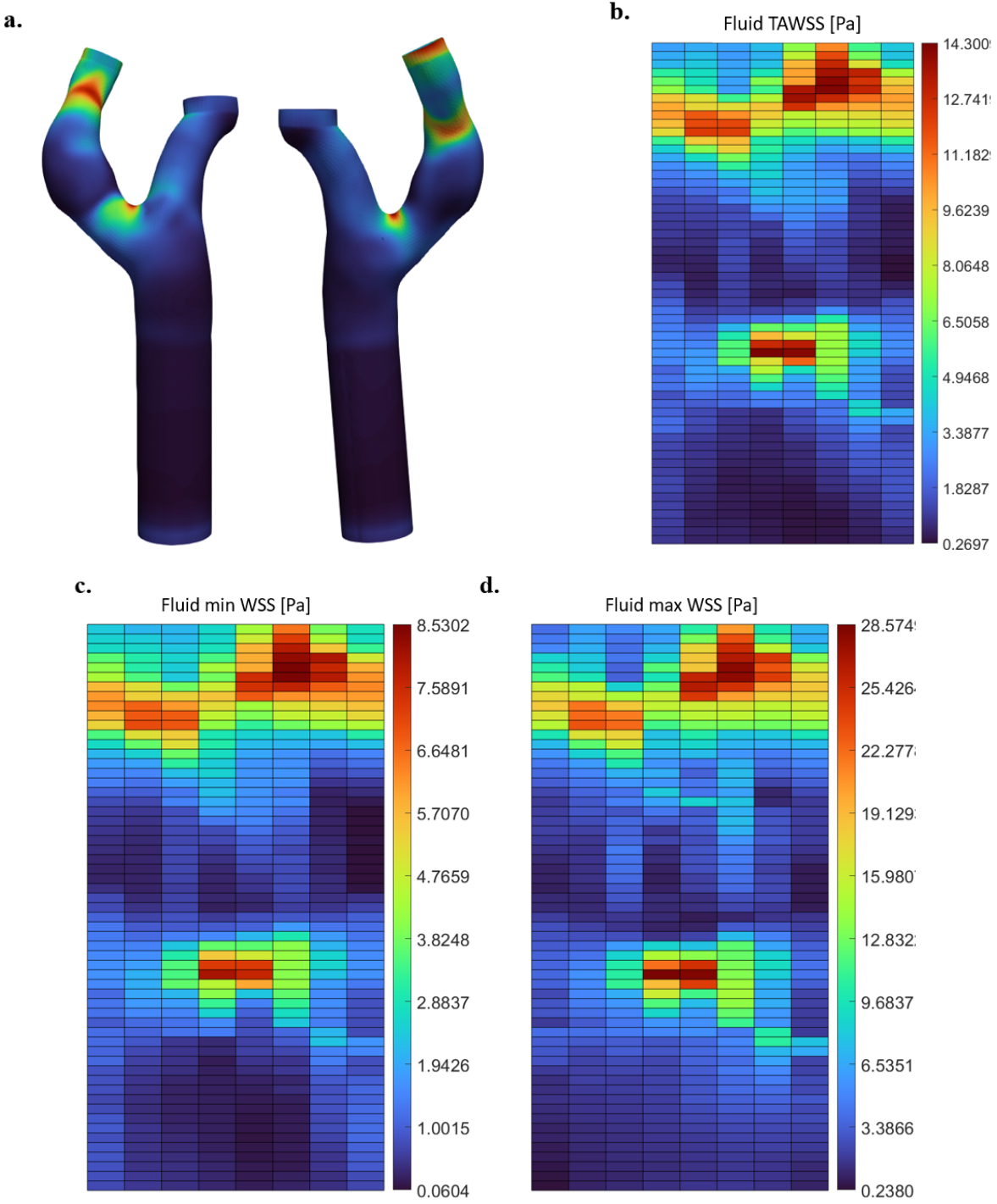


**Figure E.32: Fluid wall shear stress (WSS) for case 3R.** a. Front view and back view of the stress distribution. b. 2D map of fluid time-average WSS. c. 2D map of min fluid WSS over a cycle. d. 2D map of max fluid WSS over a cycle.

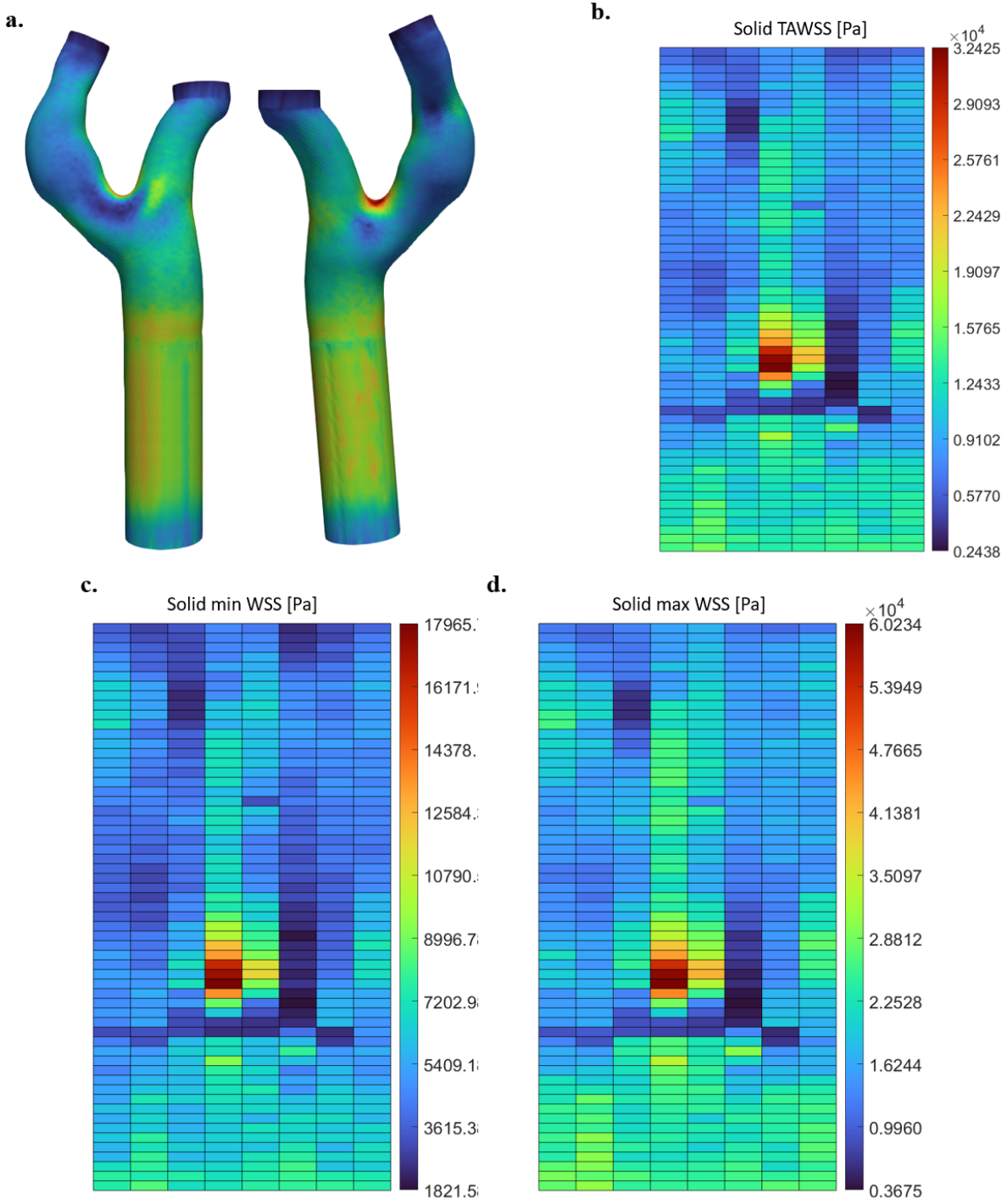


**Figure E.33: Solid wall shear stress (WSS) for case 3R.** a. Front view and back view of the stress distribution. b. 2D map of solid time-average WSS. c. 2D map of min solid WSS over a cycle. d. 2D map of max solid WSS over a cycle.

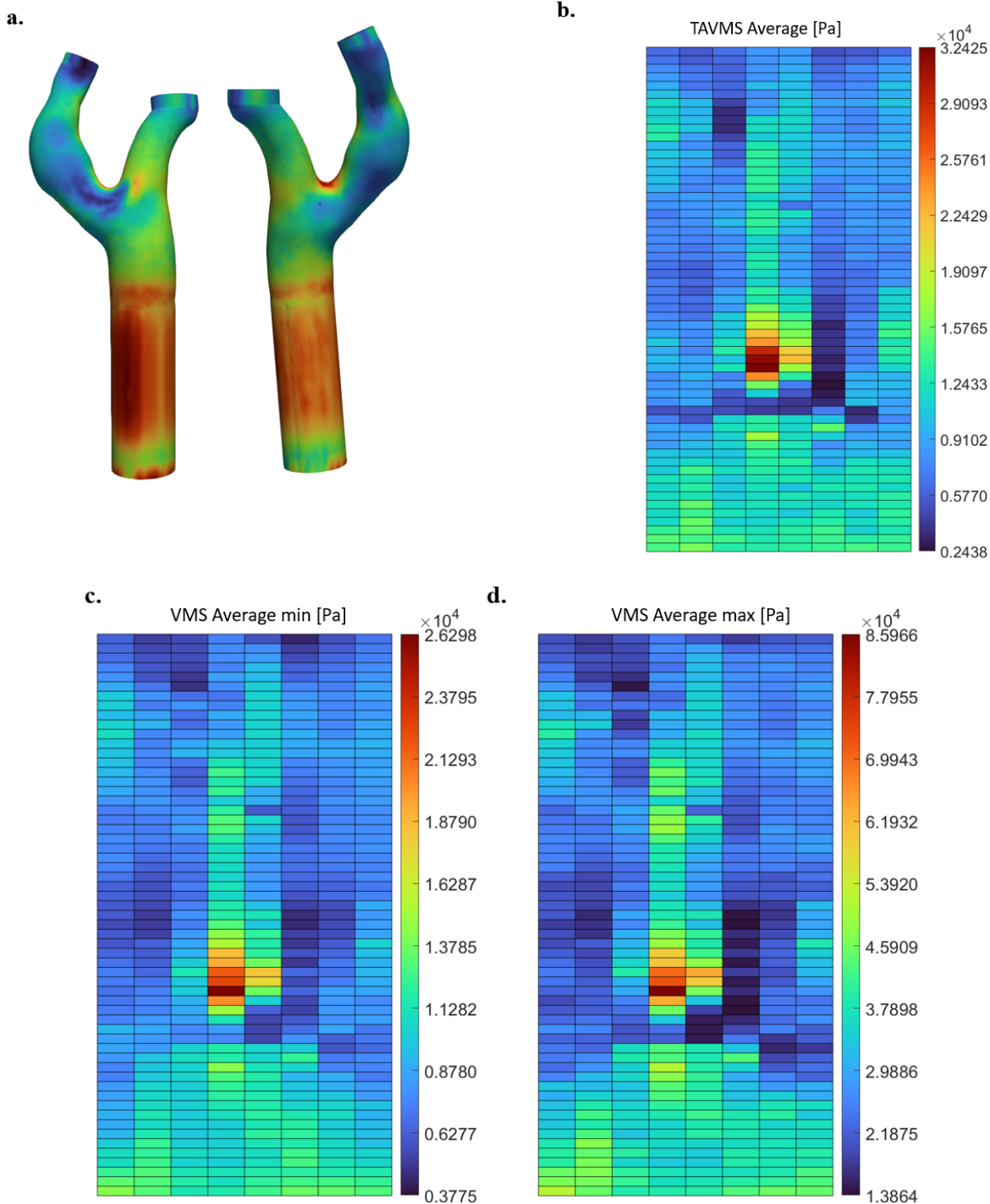


**Figure E.34: Average von Mises stress (VMS) for case 3R.** a. Front view and back view of the stress distribution. b. 2D map of average VMS. c. 2D map of min average VMS over a cycle. d. 2D map of max average VMS over a cycle.

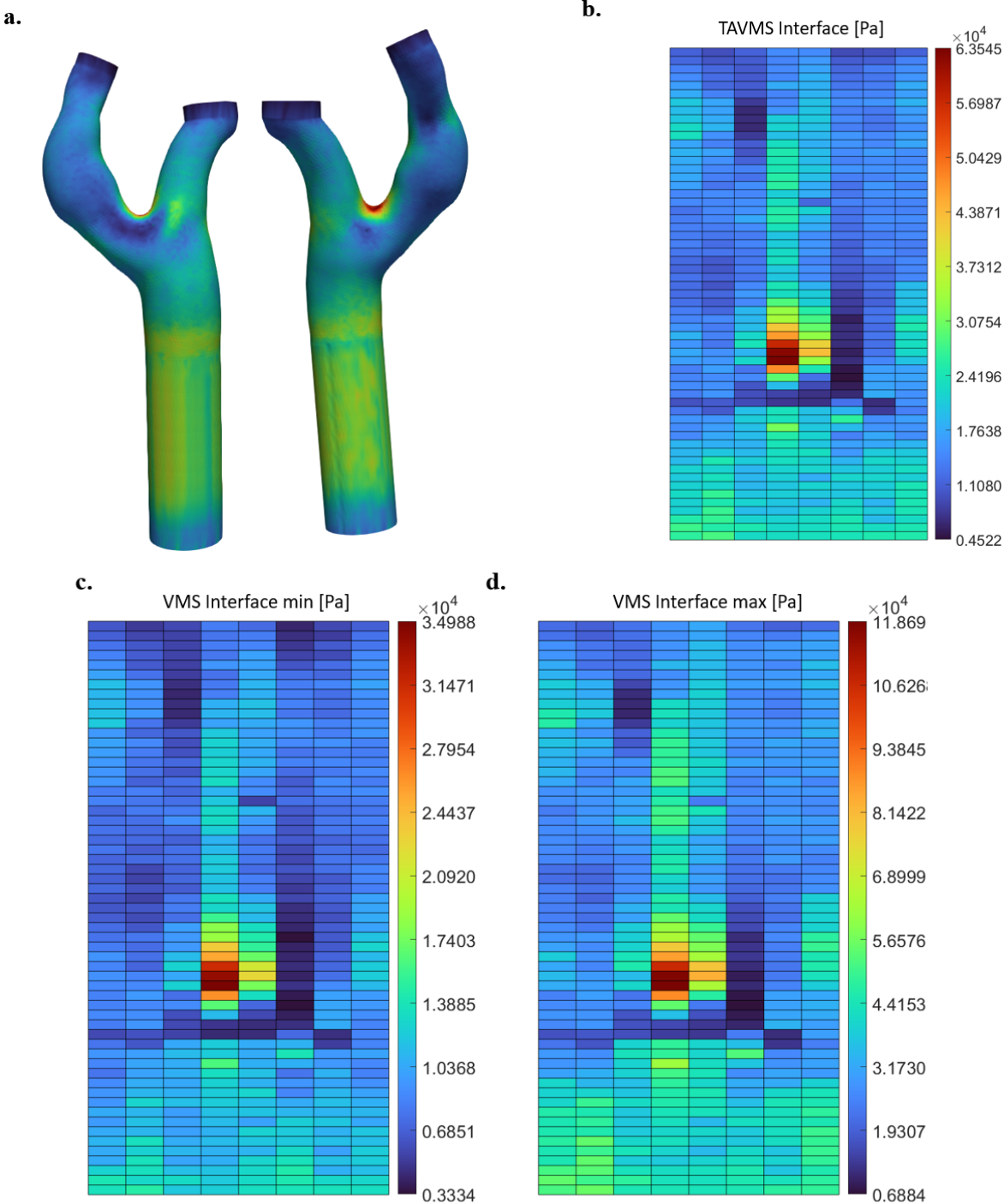


**Figure E.35: Interface von Mises stress (VMS) for case 3R.** a. Front view and back view of the stress distribution. b. 2D map of interface VMS. c. 2D map of min interface VMS over a cycle. d. 2D map of max interface VMS over a cycle.